

**DISPERSION AND ALIGNMENT OF CARBON NANOTUBES IN
POLYMER BASED COMPOSITES**

A Dissertation
Presented to
The Academic Faculty

by

Erin Lynn Camponeschi

In Partial Fulfillment
of the Requirements for the Degree
Doctor of Philosophy in the
School of Materials Science and Engineering

Georgia Institute of Technology
DECEMBER 2007

COPYRIGHT 2007 BY ERIN LYNN CAMPONESCHI

DISPERSION AND ALIGNMENT OF CARBON NANOTUBES IN POLYMER BASED COMPOSITES

Approved by:

Dr. Rina Tannenbaum, Advisor
School of Materials Science and
Engineering
Georgia Institute of Technology

Dr. Ken Gall
School of Materials Science and
Engineering
Georgia Institute of Technology

Dr. Thomas Sanders
School of Materials Science and
Engineering
Georgia Institute of Technology

Dr. Hamid Garmestani, Advisor
School of Materials Science and
Engineering
Georgia Institute of Technology

Dr. Meisha Shofner
School of Polymer, Textile, and Fiber
Engineering
Georgia Institute of Technology

Date Approved: July 23, 2007

For my family and friends

ACKNOWLEDGEMENTS

I would first like to thank my parents for supporting my decisions and supporting me while I attained by goals. My advisors, Dr. Rina Tannenbaum and Dr. Hamid Garmestani, have also guided me through my graduate work and helped mold me into the researcher I am today. My thesis committee, Dr. Meisha Shofner, Dr. Ken Gall, and Dr. Thomas Sanders, has also given me lots of support and assistance.

This work could not have been completed without the help of my research group members, past and present: Melissa Williams, Jeremy Walker, Kasi David, Dan Ciprari, Cantwell Carson, and Lex Nunnery. I would like to thank all of the friends who've come and gone throughout my years here at Georgia Tech: Beth, Anne, Ven, Morgan, Matt, Kip, Dan, Laura A., Laura C., Terra, Stef, Rob, Scott, Pete, Jelila, Liz, Laura D., Heather, Chris, and especially Brett. And last but not least, are the wonderful MSE office staff who've helped me navigate classes, registration, and finally graduation: Susan, Karen, Jyoti, Mechelle, Renita, Shirely, and Jasmin.

I would also like to acknowledge the funding that allowed my research to be continued these four years here at Georgia Tech. This work was supported by Institute of Paper Science and Technology at Georgia Tech through the Otto Kress Scholarship, without their generosity and support I would not be where I am today.

TABLE OF CONTENTS

	Page
ACKNOWLEDGEMENTS	iv
LIST OF TABLES	x
LIST OF FIGURES	xi
SUMMARY	xix
 <u>CHAPTER</u>	
1 Introduction	1
2 Background	4
2.1 Overview	4
2.2 Metal, Ceramic, and Carbon Composite Materials	5
2.3 Polymer Matrix Composites	6
2.3.1 Carbon Reinforcing Materials for Polymer Based Composites	8
2.4 Early Carbon Nanomaterials	9
2.4.1 Fullerenes and Carbon Nanotubes	10
2.5 Carbon Nanotube Properties	14
2.5.1 Mechanical Properties of Carbon Nanotubes	15
2.5.2 Carbon Nanotube Reactivity	16
2.6 Carbon Nanotube Polymer-Based Composite Properties	20
2.6.1 Carbon Nanotube Polymer-Based Composite Properties Mechanical Properties	20
2.6.2 Dispersion of Carbon Nanotubes	21
2.6.3 Alignment of Carbon Nanotubes	24
2.5.4 Novel Approach to Disperse and Align Carbon Nanotube Polymer-Based Composites In Situ	26

3	Materials and Materials Characterization	28
3.1	Overview	28
3.2	Materials	28
3.2.1	Carbon Nanotubes	28
3.2.2	Surfactant Sodium Dodecyl Benzene Sulfonate	29
3.2.3	Commerical Block Copolymer Dispersing Agent	29
3.2.4	Pluronic F108	29
3.2.5	Carboyslmethyl Cellulose	30
3.2.5	Sol Gel Precursor Materials	30
3.3	Transmission Electron Microscopy	30
3.4	Raman Spectroscopy	31
3.5	Mechanical Property Characterization	35
3.5.1	Dynamic Mechanical Analysis	35
3.5.2	Compression Testing	37
3.6	X-Ray Diffraction	40
3.6.1	Small Angle X-Ray Scattering	41
3.7	Differential Scanning Calorimetry	42
4	Effects of Different Dispersing Agents on Polymer Carbon Nanotube Composites	45
4.1	Overview	45
4.2	Introduction	45
4.3	Experimental Procedure	47
4.4	Results and Discussion	50
4.4.1	Dispersion Mechanisms	50
4.4.2	Effect of Glass Transition Temperature	56

4.4.3	Effect on Storage, Loss Modulus and Tan Delta	59
4.4.4	Small Angle X-Ray Scattering (SAXS) of SWNT-Epoxy Composites	66
4.5	Summary of Dispersing Agents Effects on Carbon Nanotube Polymer Composites	69
5	Alignment of Carbon Nanotubes Under Shear Viscous Flow for Polymer and Epoxy Composite Systems	70
5.1	Overview	70
5.2	Introduction	70
5.3	Experimental Procedure	72
5.3.1	Polymer Viscous Flow	72
5.3.2	Epoxy Composites	74
5.4	Viscous Polymer Flow Results and Discussion	75
5.4.1	Dispersion of SWNTs	75
5.4.2	Orientation of SWNT in Shear Flow	78
5.5	Epoxy Composite Results and Discussion	85
5.5.1	Dispersion of SWNTs in Shear Flow	85
5.5.2	Orientation of SWNTs in Epoxy Composites	86
5.5.3	Raman Spectroscopy of SWNT in Epoxy Composites	87
5.5.4	Dynamic Mechanical Analysis of SWNT in Epoxy Composites	91
5.5.4.1	Effect on Glass Transition Temperature	91
5.5.4.2	Effect on Storage and Loss Modulus and Tan Delta	93
5.6	Summary of Viscous Polymer and Epoxy Composite Systems	96
6	Properties of Carbon Nanotube-Polymer Composites Aligned in a Magnetic Field	97
6.1	Overview	97
6.2	Introduction	97

6.3	Experimental Procedure	98
6.4	Results and Discussion of Magnetic Field Aligned Carbon Nanotubes	101
6.4.1	Effect of Glass Transition Temperature	102
6.4.2	Effect of Storage, Loss Modulus and Tan Delta	105
6.4.3	Effect of Young's Modulus	111
6.4.4	Effect on Raman Scattering	112
6.5	Summary of Mechanical Properties of Magnetic Field Alignment of Carbon Nanotubes	115
7	Carbon Nanotubes Decorated with Iron (III) Oxide Particles from Sol Gel Processing for Magnetic Applications	117
7.1	Overview	117
7.2	Introduction	118
7.3	Experimental Procedure	120
7.4	Results and Discussion of Iron (III) Oxide Decorated Carbon Nanotubes	122
7.4.1	Modified Sol Gel Processing of Iron (III) Oxide Particles	122
7.4.2	Decoration of CNTs with Iron (III) Oxide Nanoparticles	131
7.5	Summary of Decorating Carbon Nanotubes with Iron (III) Oxide Nanoparticles	133
8	Magnetic Alignment of Iron (III) Oxide Decorated Carbon Nanotubes Polymer Composites	134
8.1	Overview	134
8.2	Introduction	134
8.3	Experimental Procedure	135
8.4	Results and Discussion of Iron(III) Oxide Decorated Aligned Carbon Nanotubes	138
8.4.1	Effect on Glass Transition Temperature	139
8.4.2	Compression Testing	141

8.4.3 Effect on Young's Modulus	145
8.4.4 Effect on Raman Scattering	150
8.5 Summary of Decorating Carbon Nanotubes with Iron (III) Oxide Nanoparticles for Magnetic Field Alignment	154
9 Conclusions	156
10 Recommendations	162
APPENDIX A	164
REFERENCES	178
VITA	201

LIST OF TABLES

	Page
Table 2.1: Young's Modulus Data for SWNT and MWNTs	16
Table 4.1: Summary of the measured and calculated mechanical properties, such as glass transition temperature, elastic modulus, storage modulus, and loss modulus for the various samples characterized in this work.	49
Table 5.1: Summary of the mechanical properties of the various SWNT-containing solutions.	79
Table 6.1: Summary of the measured and calculated mechanical properties, such as glass transition temperature, elastic modulus, storage modulus, and loss modulus for the various samples characterized in this work.	101
Table 7.1: Summary of the characteristics of the modified sol-gel process for the various reactions performed in this study. Specific molar quantities for each reactant are described in the Experimental section.	121
Table 7.2: Summary of the iron oxide product size and morphology resulting from the modified sol-gel process for the various reactions performed in this study.	125
Table 8.1: Summary of the sample parameters, such as carbon nanotube content, iron oxide batches, and magnetic field applied.	137
Table 8.2: Summary of the measured and determined sample properties, such as glass transition temperature, carbon nanotube content, iron oxide batches, applied magnetic field, and Raman analysis.	140
Table 8.3: Summary of the compression test values for the samples in alignment direction (#a) and perpendicular to alignment direction (#b) coupled with Raman analysis.	147
Table A.1: Nomenclature for distribution functions	167
Table A.2: Limiting conditions for the two-point probability function	172

LIST OF FIGURES

	Page
Figure 2.1 C60 Fullerene Molecules	12
Figure 2.2: Illustrates the three different types of carbon nanotubes a) single walled b) double walled c) multiwalled	13
Figure 2.3: Graphene sheet illustrating Chirality	14
Figure 2.4: Mismatch Between π Bonding Orbitals in a Nanotube	16
Figure 2.5: Potential of interaction between two parallel SWNTs as function of the distance between them, as calculated by Grifalco, <i>et Al.</i> Note the very deep attractive well when the SWNTs are in contact.	19
Figure 3.1: The difference between normal and resonance Raman	33
Figure 3.2: The ideal Raman spectrum for carbon nanotubes	34
Figure 3.3: Viscoelastic Stress-Strain Relation	36
Figure 3.4: Typical DMA Data Plot	37
Figure 3.5: Stress-Strain relation for various types of materials	38
Figure 3.6: Illustration of DSC Setup	42
Figure 3.7: Sample DSC Scan	43
Figure 4.1: Transmission electron microscopy micrographs of SWNT dispersed with 0.409 vol% NaDDBS at varying carbon nanotubes concentrations to illustrate variations in bundle size (a) 0.263 vol% CNT, bundle size 15-20nm (b) 0.789 vol% CNT, bundle size 15-60nm.	51
Figure 4.2: Schematic illustration of how copolymers utilize lypholic and lyphobic blocks as the mechanism for the dispersion of SWNTs in solution. The respective blocks associated with the solution and the carbon nanotubes allowing for the exfoliation and dispersion of the carbon nanotubes.	52

Figure 4.3: Transmission electron microscopy micrographs of SWNT dispersed with BCP at increasing BCP concentrations to illustrate the variation in bundle size as BCP concentration increases (a) 0.495 vol% BCP, 0.263 vol% CNTs, bundle size 75 nm (b) 1.980 vol% BCP, 0.263 vol% CNTs, bundle size 90 nm. 53

Figure 4.4: Transmission electron microscopy micrographs of SWNT dispersed with Pluronic F108 at increasing concentration to illustrate the variation in bundle size as the Pluronic concentration increases (a) 0.189 vol% Pluronic bundle size 15-25 nm, 0.263 vol% CNTs (b) 0.566 vol% Pluronic, 0.263 vol% CNTs, bundle size 15-40 nm. 55

Figure 4.5: This graph illustrates the effect of the dispersed carbon nanotubes at various concentrations on the epoxy glass transition temperature. The glass transition temperature is affected differently and is correlated to the dispersing agent and its properties. 57

Figure 4.6: These graphs illustrate the effect on the epoxy glass transition temperature as a function of the (a) Pluronic and (b) BCP at varying concentrations. This illustrates a contradicting effect of the copolymers on the glass transition temperature, which corresponds to the different molecular weight and interactions of the co-polymers in the epoxy matrix. 58

Figure 4.7: Experimental Dynamic Mechanical analysis data illustrating the average loss modulus for the three different dispersing agents at varying carbon nanotube concentration at two temperatures (a) 30°C (b) 10°C. This data illustrates that there is a very different effect on the loss modulus between the NaDDBS and BCP versus the Pluronic at 30°C. At 10°C, there appears to be almost no change in the NaDDBS and BCP systems, but a profound increase in loss modulus in the Pluronic system. 60

Figure 4.8: Pictures of the three bulk composite samples and corresponding light microscope images at 10x magnification of the three different dispersing agents at the same carbon nanotube concentration (a) 0.495 vol% BCP; 0.263 vol% CNTs, (b) 0.409 vol% NaDDBS; 0.263 vol% CNTs (c) 0.189 vol% Pluronic; 0.263 vol% CNTs 63

Figure 4.9: Experimental Dynamic Mechanical analysis data illustrating the average Storage modulus for the three different dispersing agents at varying carbon nanotube concentration at two temperatures (a) 30°C (b) 10°C. The storage moduli of the NaDDBS and BCP appear to decrease slightly at lower temperatures with higher concentrations of CNT. Conversely, the storage modulus of the Pluronic system increases considerably with the increase in CNT concentration beyond ~0.3 vol.%. 64

Figure 4.10: Experimental Dynamic Mechanical analysis data illustrating the average $\tan\delta$ for the three different dispersing agents at varying carbon nanotube concentration at two temperatures (a) 30°C (b) 10°C. The data had large fluctuations that were particularly pronounced in the experiments conducted at 10°C. This is due to the opposing behavior in the loss and storage moduli of the Pluronic system at 30 °C and at 10 °C. 65

Figure 4.11: Experimental SAXS data of an illustrating three different types of orientation of a lamellar structure in the composite samples (a) isotropic (b) slight anisotropy (d) complete anisotropy. The presence of lamellar structures in the pure epoxy matrix is indicative of the existence of crystalline regions. The changes in the presences of and orientation of the crystalline region in the composite samples are likely from intermolecular interactions of the epoxy with the carbon nanotubes, dispersing agents, and also the combined intermolecular interactions between the carbon nanotubes and dispersing agent. 66

Figure 4.12: Experimental calculation of the ratio between the CNT and dispersing agent for each systems and the correspond effect on the glass transition temperature. This graph illustrates two behavior regimes for the NaDDBS and the BCP composites. At low volume % the behavior is related to the dispersing molecules, but at higher volume % the behavior is dependent upon the CNTs. 68

Figure 5.1: Schematic representation of the experimental set-up: (a) Concentric cylinder arrangement in the Brookfield viscometer; (b) TEM sample retrieval and preparation 73

Figure 5.2: Schematic representation of the stabilization mechanism of carbon nanotubes: interaction between SWNT with NaDDBS, followed by the addition of CMC. 76

Figure 5.3: TEM micrographs of SWNT at different levels of dispersion and stabilization efficiency: (a) Undispersed carbon nanotubes; (b) Carbon nanotubes dispersed with NaDDBS; (c) Carbon nanotubes dispersed with NaDDBS and CMC. Note that the black spherical aggregates present in the image are the remnant metallic oxide catalyst particles used in the synthesis of the SWNT.

77

Figure 5.4: Carboxymethyl Cellulose polymer chain illustrating β 1 moiety.

78

Figure 5.5: Summary of the calculated shear stresses of the various SWNT-containing solutions used in the various experiments: (a) Plots of shear stresses as a function of angular velocity; (b) Plots of the shear stresses originating from the contribution of pure SWNT in the various systems as a function of angular velocity.

80

Figure 5.6: TEM micrographs of the orientation attempts of several systems containing SWNT: (a) Undispersed carbon nanotubes in a 1 wt% CMC suspension subjected to shear flow at 100 rpm; (b) Carbon nanotubes dispersed with NaDDBS and CMC and subjected to shear flow at 30 rpm; (c) Carbon nanotubes dispersed with NaDDBS and CMC and subjected to shear flow at 60 rpm; (d) Oriented carbon nanotubes dispersed with NaDDBS and CMC and subjected to shear flow at 100 rpm. The inset image is a four-fold magnification of the larger image (same scale bar = 5 nm) showing in more detail the local orientation of the surface-modified SWNT. Note that the black spherical aggregates present in these images are the remnant metallic oxide catalyst particles used in the synthesis of the SWNT.

82

Figure 5.7: Raman spectra of samples containing SWNT that were subjected to shear flow: (a) Orientation-dependent Raman spectra of SWNT with different angles (from 0 to 90 degrees) between the polarization of the incidence laser light and the nanotube axis using VV (parallel polarization of the incidence and scattered light) configuration. (b) The direct comparison of the experimental relative intensities of the 1594 cm^{-1} G band as a function of the angle of polarization of the incident radiation, with theoretical calculations.

84

Figure 5.8: Illustration of the Pluronic stabilization mechanism of carbon nanotubes in solution.

86

Figure 5.9: Raman spectra of the (a) aligned epoxy and (b) epoxy only samples at various orientations.

88

Figure 5.10: Raman spectra of (a) $\frac{1}{2}$ wt% CNT-NaDDBS, (b) $\frac{1}{2}$ wt% CNT-Pluronic, (c) 1 wt% CNT- Pluronic, and (d) 1 wt% CNT- NaDDBS at various angles of orientation.

89

- Figure 5.11: Raman spectra of D' peak for alignment analysis (a) ½ wt% NaDDBS (b) 1 wt% NaDDBS 90
- Figure 5.12: Glass Transition Temperature data for (a) NaDDBS Samples (b) Pluronics Samples 92
- Figure 5.13: The effect of the alignment on the Storage Modulus for (a) Pluronics Samples (b) NaDDBS Samples and the Loss Modulus for (c) Pluronics Samples (d) NaDDBS Samples 94
- Figure 5.14: The effect of alignment and CNT weight percent on Tan δ for (a) Pluronics Samples (b) NaDDBS Samples 95
- Figure 6.1: The effect of the magnetic field on the glass transition temperature of epoxy matrices reinforced with carbon nanotubes: (a) CF epoxy with both single-wall and multi-wall carbon nanotubes; (b) AP epoxy with both single-wall and multi-wall carbon nanotubes. 103
- Figure 6.2: The predicted effect of the application of an external magnetic field on the orientation and alignment of polymer chains. 105
- Figure 6.3: The effect of the applied magnetic field on the loss and storage moduli of epoxy matrices reinforced with carbon nanotubes: (a) The loss modulus of CF epoxy reinforced with single-wall and multi-wall carbon nanotubes; (b) The loss modulus of AP epoxy reinforced with single-wall and multi-wall carbon nanotubes; (c) The storage modulus of CF epoxy reinforced with single-wall and multi-wall carbon nanotubes; (d) The storage modulus of AP epoxy reinforced with single-wall and multi-wall carbon nanotubes. 107
- Figure 6.4: The effect of the applied magnetic field on the tan δ of epoxy matrices reinforced with carbon nanotubes: (a) CF epoxy reinforced with multi-wall carbon nanotubes exposed to various external magnetic fields; (b) AP epoxy reinforced with multi-wall carbon nanotubes exposed to various external magnetic fields. 109
- Figure 6.5: The effect of the applied magnetic field on the elastic modulus of epoxy matrices reinforced with carbon nanotubes: (a) AP epoxy with both single-wall and multi-wall carbon nanotubes; (b) CF epoxy with both single-wall and multi-wall carbon nanotubes. 110

Figure 6.6: The effect of the applied magnetic field on the alignment of the carbon nanotube chains for both types of carbon nanotubes as inferred from the changes of the intensity of their G band in their Raman spectra: (a) AP epoxy reinforced with both single-wall and multi-wall carbon nanotubes; (b) CF epoxy reinforced with both single-wall and multi-wall carbon nanotubes; (c) The Raman spectrum of the AP epoxy matrix reinforced with single-wall carbon nanotubes at different applied magnetic field strengths; (d) The Raman spectrum of the CF epoxy matrix reinforced with single-wall carbon nanotubes at different applied magnetic field strengths. 113

Figure 6.7: TEM images of MWCNTs embedded in epoxy matrices placed under a 17 T magnetic field. (a) AP-based composite, and (b) CF-based composite. (Note that these samples could not be tested for their mechanical properties due to inadequate sample dimensions and hence, it is assumed that these images approximate their respective nanocomposite morphology at 15 T). 115

Figure 7.1: Schematic representation of the modified sol-gel process involving the use of a surfactant, NaDDBS. In the absence of NaDDBS, the system undergoes gelation (top process), while in the presence of NaDDBS the system either does not gel or gelation is delayed (bottom process), but the particles formed are of similar size as the primary particles in the systems formed by the regular sol-gel method. 119

Figure 7.2: Schematic representation of the hydration sphere around the iron (III)/iron oxide centers coupled with the preferred location of the NaDDBS surfactant molecules. The structure depicted shows the steric and electrostatic barrier that the NaDDBS molecules create around the iron (III) centers, which inhibits the formation of a gel. The 3D schematic was achieved by the use of the commercial software ChemDraw 3D 123

Figure 7.3: Pictures of the six different iron oxide samples obtained via the modified sol-gel process. The characteristics of the specific reactions in each solution are summarized in Table 7.1. Note the bright orange color of sample 3 as compared to the brown color of all other samples. 126

Figure 7.4: High resolution transmission electron microscopy (HRTEM) images of the iron oxide products obtained from the various reactions performed as per the specifications summarized in Table 1: (a) $\text{FeCl}_3 \cdot 6\text{H}_2\text{O}$ precursor with NaDDBS added prior to the gelation process and upon drying (sample 1); (b) $\text{Fe}(\text{NO}_3)_3 \cdot 9\text{H}_2\text{O}$ precursor with NaDDBS added prior to the gelation process and upon drying (sample 2); (c) $\text{FeCl}_3 \cdot 6\text{H}_2\text{O}$ precursor with NaDDBS added prior to the gelation process (sample 3); (d) $\text{Fe}(\text{NO}_3)_3 \cdot 9\text{H}_2\text{O}$ precursor with NaDDBS added prior to the gelation process; (e) $\text{FeCl}_3 \cdot 6\text{H}_2\text{O}$ precursor without NaDDBS (sample 5); (f) $\text{Fe}(\text{NO}_3)_3 \cdot 9\text{H}_2\text{O}$ precursor without NaDDBS (sample 6). 127

Figure 7.5: Particle size distribution for the iron oxide nanoparticles obtained in the various samples, and based on the HRTEM images shown in Figure 4: (a) $\text{FeCl}_3 \cdot 6\text{H}_2\text{O}$ precursor with NaDDBS added prior to the gelation process and upon drying (sample 1); (b) $\text{Fe}(\text{NO}_3)_3 \cdot 9\text{H}_2\text{O}$ precursor with NaDDBS added prior to the gelation process and upon drying (sample 2); (c) $\text{FeCl}_3 \cdot 6\text{H}_2\text{O}$ precursor with NaDDBS added prior to the gelation process (sample 3); (d) $\text{Fe}(\text{NO}_3)_3 \cdot 9\text{H}_2\text{O}$ precursor with NaDDBS added prior to the gelation process; (e) $\text{FeCl}_3 \cdot 6\text{H}_2\text{O}$ precursor without NaDDBS (sample 5); (f) $\text{Fe}(\text{NO}_3)_3 \cdot 9\text{H}_2\text{O}$ precursor without NaDDBS (sample 6). 128

Figure 7.6: Experimental X-ray diffraction patterns for the iron oxide nanoparticles obtained in the various samples summarized in Table 1: (a) $\text{FeCl}_3 \cdot 6\text{H}_2\text{O}$ precursor with NaDDBS added prior to the gelation process and upon drying (sample 1); (b) $\text{Fe}(\text{NO}_3)_3 \cdot 9\text{H}_2\text{O}$ precursor with NaDDBS added prior to the gelation process and upon drying (sample 2); (c) $\text{FeCl}_3 \cdot 6\text{H}_2\text{O}$ precursor with NaDDBS added prior to the gelation process (sample 3); (d) $\text{Fe}(\text{NO}_3)_3 \cdot 9\text{H}_2\text{O}$ precursor with NaDDBS added prior to the gelation process; (e) $\text{FeCl}_3 \cdot 6\text{H}_2\text{O}$ precursor without NaDDBS (sample 5); (f) $\text{Fe}(\text{NO}_3)_3 \cdot 9\text{H}_2\text{O}$ precursor without NaDDBS (sample 6). 129

Figure 7.7: Theoretical X-ray diffraction patterns for various iron oxide/oxyhydroxide phases: (a) $\alpha\text{-Fe}_2\text{O}_3$ (hematite); (b) $\text{Fe}(\text{OH})_3$; (c) $\alpha\text{-FeO}(\text{OH})$ (ferrihydrite); (d) $\gamma\text{-Fe}_2\text{O}_3$; (e) $\gamma\text{-FeO}(\text{OH})$; and (f) $\delta\text{-FeO}(\text{OH})$. 130

Figure 7.8: Carbon nanotubes decorated with iron oxide particles with various CNT-NaDDBS-Iron oxide bundle sizes (a) 15-40 nm (b) 45 nm (c) 10-20 nm (d) 4 nm iron oxide particles with ~45nm bundle sizes 132

Figure 8.1: Experimental stress versus strain data from compression testing of the epoxy only at various magnetic fields. This illustrates the increase in yield point with increasing magnetic field. 142

Figure 8.2: Experimental stress versus strain data from the compression testing of the composite samples. This illustrates the effect of magnetic field on (a) $\frac{1}{2}$ wt% CNT (b) 1wt% CNT samples with various iron oxide particle concentrations. This illustrates the profound increase in plasticity that occurs with the addition of Fe_2O_3 and 0.5 wt% CNT at 0.0 Tesla, which disappears with increased magnetic fields and Fe_2O_3 content. 143

Figure 8.3: Experimental stress versus strain data from the compression testing of the composite samples. This illustrates the effect of the magnetic field on various concentrations of carbon nanotubes and iron oxide (a) 0 Tesla (b) 0.4 145

Figure 8.4: Experimental stress versus strain data from the compression testing of the composite samples. This illustrates the change in elastic modulus of the composite samples from room temperature (25°C) to above the glass transition temperature (100 °C) for (a) the epoxy only data and (b) the composite data sets at various carbon nanotube and iron oxide content. The data concludes that the epoxy only has an optimum magnetic field at 0.8 Tesla, conversely at 0.5wt% CNTs and a double batch of iron oxide there is an optimum magnetic field of 0.4 Tesla.	149
Figure 8.5: Raman spectroscopy data of epoxy only (a) complete spectra (b) CNT/epoxy G peak overlap. Therefore, the typical alignment analysis to determine alignment using the G band Raman peak is inconclusive.	151
Figure 8.6: Raman spectroscopy data of aligned the CNT samples at 0.8 Tesla using the D band to determine alignment (a) peak over lap with epoxy peak at 2000 cm ⁻¹ (b) distinct Raman peaks. Although the intensity change is not as dramatic this illustrates that there is alignment in the carbon nanotube composite samples.	153
Figure A.1: General 2 Phase Composite Microstructure	168
Figure A.2: Determining the Volume fraction	169
Figure A.3: Determining end point of the Vectors, r	170
Figure A.4: (a) High concentration (b) Low concentration of CNTs and surfactant.	174
Figure A.5: Two-point statistical data of low concentration of CNTs	175
Figure A.6: Two point statistical data of high concentration of CNTs	176
Figure A.7: Modified Corson's Equation applied to Two-point statistical data	177

SUMMARY

This research is intended to create usable carbon nanotube polymer based composites for structural applications by effectively aligning and dispersing the carbon nanotubes in a polymer matrix. The motivation for this research is to create very lightweight, high strength materials that will surpass their predecessors: carbon fibers. The final product then can be used in applications across the industries.

The ability to create a carbon nanotube polymer based composite requires the ability to overcome the barriers that are created when impregnating carbon nanotubes in to a polymer matrix and still obtain a usable product. The first barrier is the van der Waals forces that attract the carbon nanotubes together and cause aggregation to occur. The second barrier is to create good cohesion between the carbon nanotubes and the polymer matrix so that the transfer of stress can occur upon loading. The third barrier is to manipulate the carbon nanotubes to align themselves to create an anisotropic modulus.

This research will determine the effect of three different surface-active agents and two different aligning methods on the structural features and mechanical properties of the polymer-based composite. The three types of surface-active agents used in this research are a surfactant and two different block copolymers. From this research, it will be determined how different surface-active agents adequately disperse the carbon nanotube, and the effects the dispersing agent have on a final dispersed product. In addition, the dispersing agent effects on the alignment of the carbon nanotubes and the final product can be compared.

The two alignment techniques used in this research were alignment via shear flow and tethering iron oxide particles to the carbon nanotubes to induce alignment in a

magnetic field. The method of shear aligning carbon nanotubes is very simplistic in theory, but actual application becomes much more challenging. This research illustrates the effects on shear alignment in a viscous polymer flow and then applies those theories to polymers.

The second method of alignment builds upon previous research where the carbon nanotubes were added to an epoxy that reorients and aligns the polymer chains in the presence of a high magnetic field. The reorientation and alignment of the polymer chains then would induce alignment in the carbon nanotubes and create a well-oriented composite. This research builds upon the ideas of manipulating carbon nanotubes in a low magnetic field by using the addition of iron oxide nanoparticles to decorate the carbon nanotubes.

This work then compares the different alignment techniques to determine the overall increase of properties and the effective carbon nanotube alignment. This research provides a framework for the creation of dispersed and aligned composites that can be expanded upon and improved to further develop the carbon nanotubes as possible replacement fillers for composite materials.

CHAPTER 1

INTRODUCTION

Since the discovery of single walled and multi-walled carbon nanotubes (SWNT and MWNT), in the early 1990s, there has been research utilizing carbon nanotubes (CNT) as a reinforcing fiber in composites due to their exceptional and unique mechanical properties. However, early studies regarding nanotube reinforced polymer composites have failed to yield the full mechanical potential of carbon nanotubes.^{1, 2} The problem with carbon nanotube polymer composites lies in the inability to optimize the mechanical properties of the composite. The failure is due to the lack of dispersion of the carbon nanotubes due to van der Waals forces and the inability to effectively align the carbon nanotubes. In addition to the van der Waals forces that cause the carbon nanotubes to aggregate, carbon nanotubes are relatively insoluble in common solvents. This insolubility lends to poor interfacial bonding between the polymer matrix and the carbon nanotubes.³ However, it has been found that the insolubility can be minimized by the use of surface active agents. Surface active agents act as a link between the carbon nanotubes and the matrix material, thus increasing the interfacial bonding. Therefore, the insolubility of carbon nanotubes in polymer-based composites remains a crucial issue that needs to be addressed in order to create these composites.

The goal of this research is to develop new approaches for the improvement of the properties of polymer carbon nanotube composites by effectively aligning and dispersing the CNT's in the polymer matrix. Specifically, this researched explored at how to

mediate the problem of carbon nanotube insolubility in a matrix material. This was accomplished by assessing the effects of three different dispersing agents and two different alignment methods on the final composite properties. In previous research, the dispersing agents were found to either adequately disperse the carbon nanotubes or improve the mechanical properties of the composite material.⁴⁻⁶ Thus, comparing the three dispersing agents in different matrix materials and different processing methods can lead to a new understanding of interfacial interactions within the different composite materials. This understanding can then lead to the creation of more effective carbon nanotube composites that both adequately disperse the carbon nanotubes and improve the mechanical properties.

Therefore, the ability to improve the composite properties comes from understanding the nature of the interfacial interactions for each dispersing agent and utilizing these interactions to improve the composite. The understanding of these interfacial properties can be achieved by using mechanical characterization techniques such as microscopy and mechanical properties tests. The information obtained from these techniques gives insight to the microstructure of the composite. Therefore, we can understand how the different components of the composite could potentially affect the composite needs to be understood when characterizing the effectiveness of the carbon nanotubes influence on the final product.

This research also addresses the necessity of alignment to produce higher quality carbon nanotube polymer based composites. Carbon nanotubes are known for their large uniaxial modulus, making the alignment of the carbon nanotubes crucial in creating a composite with uniaxial strength for structural applications. However, alignment of the

carbon nanotubes is contingent on the ability to disperse the carbon nanotubes. Therefore, the dispersion and alignment of carbon nanotubes becomes a requirement in order to produce a higher quality carbon nanotube polymer based composite.

CHAPTER 2

BACKGROUND

2.1 Overview

Composite materials are typically made up of two materials, where one phase is the reinforcing phase, such as fibers, sheets, or particles and the other phase is the matrix material.⁷ The matrix materials can be a metal, ceramic, or polymer, where the reinforcing material typically is a low density, high strength or toughness material. The matrix material has properties that are desirable, such as corrosion, temperature or UV resistance, but doesn't have high strength and/or high toughness.⁷ Therefore, the addition of the reinforcing material allows the improvement of the material's properties by meshing high strength and toughness, of the reinforcing agent, with the properties of the matrix material.

There are two main types of composites, synthetic and natural. Synthetic composites have been around for several thousand years, where people added straw to bricks for building homes and laminated bowls made from wood.⁷ Wood, itself, consists of several different types of fibers. Another very common natural composite material is bone, which is made up of collagen and minerals. In the 1930s, the engineering of modern composite materials led to several different types of composite materials. The next section discusses the different types of synthetic composite materials

2.2 Metal, Ceramic, and Carbon Composite Materials

Polymers and metals are the most commonly used matrix materials because of their highly ductile nature. Ceramic composites materials are utilized for high temperature and high corrosion resistance applications. Other matrix materials such as carbon and glass are used with less frequency but can be useful for tailored applications such as, structural components in the building and aeronautical fields. This section will briefly discuss the different types of matrix materials and their corresponding reinforcement materials.

In the past thirty years, metal matrix composites (MMCs) have been studied to create light-weight, high-strength, chemical- and thermal-resistant materials. MMCs are made up of a number of different metal matrices but typically contain fillers such as carbon, silicon carbide, boron, alumina, and refractory metals.^{8,9} The enhanced properties of MMCs are directly related to their structure. Their structure is modified by the presence of the filler material and the physical properties of the filler material. MMCs are useful in military and aerospace applications.^{8,9}

MMCs can be divided into four types: fiber reinforced, particulate reinforced, dispersion-strengthened, and in situ.^{8,9} Fiber reinforced MMCs are made up of continuous or discontinuous fiber reinforcements (whiskers) with high length to diameter aspect ratios. Particulate reinforced MMCs are made up of particles or platelets and typically have a higher filler volume fraction than fiber reinforced MMCs.^{8,9} Dispersion-strengthened MMCs contain particles that are typically less than 0.1 micron in diameter.^{8,9} In situ MMCs are typically solidified eutectic alloys, which yield different compositions of the same materials, resulting in the formation of a composite material.

Ceramic materials are known for their high temperature resistance and strength, however, they are generally very brittle materials with low fracture toughness.^{8, 9} Ceramic matrix composites (CMCs) have increased fracture toughness due to the addition of fillers or by transformation toughening. The addition of filler materials (particulates fibers, or whiskers) hinders or impedes crack propagation. Transformation toughening occurs when stabilizing particles are added to the ceramic to retain high temperature crystal structures while at room temperature, resulting in residual stresses that hinder crack propagation.^{8, 9} CMCs are typically useful in high temperature/high toughness applications such as machining, automotive, and aeronautical applications.

Carbon based composite materials are typically known as carbon-carbon composites because both the matrix material and the filler are carbon. The matrix material can range from an amorphous carbon to graphitic carbon matrix with continuous woven carbon fibers as the filler material.⁸⁻¹⁰ This composite is the most advanced form of carbon, creating a stronger, tougher, thermal shock resistant, and light-weight material.⁸⁻¹⁰ The composite also has a low thermal expansion coefficient, but has poor oxidation resistance at high temperatures. These composites are, however, useful in the aeronautical, aerospace, and automotive industries.^{8, 9}

2.3 Polymer Matrix Composites (PMCs)

PMCs are one of the most diverse composite materials due of their ability to incorporate a number of different filler materials. The addition of these filler materials can reduce the cost, alter mechanical properties, reduce mold shrinkage, control viscosity,

and alter surface properties.^{8,9} These properties illustrated by PMCs allow them to be used for a wide variety of manufacturing applications.^{8,9}

The most commonly used filler materials for polymer composites are carbon fibers, carbon nanotubes, carbon vapor grown nanofibers, glass fibers, and metal or ceramic particulates. Glass fibers are added to polymeric materials to increase the specific strength and since both are relatively inert materials, allows for application in corrosive environments.^{8,9} The addition of glass to polymers can produce ion conducting composites,¹¹ impact resistant materials,¹² optical films,¹³ and other enhanced property materials.^{14,15}

The addition of ceramic materials to a polymeric matrix creates composites for several different potential applications. Ceramics are known to be very tough, brittle materials. The addition of a ceramic filler to a polymer matrix then becomes mutually beneficial, by increasing the strength of the polymer and increasing the ductility of the ceramic. The ceramic polymer composite can used to produce piezoelectric materials,^{16,17} bone replacement material,¹⁸ high dielectric materials,¹⁹ and materials for dental applications.²⁰

Metal materials can be added to polymeric materials for applications in a wide number of areas. Metals are high strength, ductile, and temperature resistance. The addition of a ductile metal to a ductile polymer creates a unique blend of properties for a variety of potential applications and properties. The addition of metals increases the strength of the polymer matrix, but it can also affect the electronic and optical properties. Metal-polymer composites have applications in robotics, medical devices, medical implants, actuators, and many other industrial applications.²¹⁻²⁴

2.3.1 Carbon Reinforcing Materials for Polymer Based Composites

Polymer-matrix composites are relatively easy to manufacture in comparison to their metal, ceramic, or carbon matrix counterparts.¹⁰ The ease at which the composites are manufactured stems from the low melting temperature that is typically found in polymer materials. However, this low melting temperature, which is very useful for manufacturing, limits the applications of polymer composites.

Polymer-matrix composites can be either a thermosetting or thermoplastic polymer.²⁵ Thermoplastics (e.g., polyethylene) are easier to manufacture than thermosets, because of their ability to have higher ductility or withstand high temperatures.²⁵ Thermoset polymers (e.g., epoxy) are widely used as a polymer matrix, because of their good mechanical properties, corrosion resistance, adhesion properties, and relatively inexpensive material cost.²⁵ Epoxies are unique polymers, because of their low molecular weight prior to curing leads to high molecular mobility. This high molecular mobility quickly and easily wets a filler material.²⁵ Epoxy composites are widely used in conjunction with carbon fillers.

Carbon is the most commonly used filler for polymer matrix composites. Carbon can take several different polymorphs: carbon fiber, graphite, diamond, carbon nanofiber, fullerene, and carbon nanotubes. Any one of the polymorphs can be used as a filler to enhance the properties of polymer matrix composites. Typically, the addition of carbon increases the strength, thermal, and electronic properties of the polymer matrix composite.

Carbon fibers were first made in 1887 from cotton fibers by Thomas A. Edison.²⁶

²⁷ In the 1950s, researchers at Wright-Patterson Air Force Base developed high strength carbon fibers for military use only.¹⁰ However, it wasn't until 1965 when Union Carbide commercialized rayon-based carbon fibers with enhanced mechanical properties were publicly available for use as filler materials.¹⁰

The addition of carbon fiber or any fibrous material for reinforcement to a polymer composite requires good bond (adhesion) between the fibers and the matrix.²⁵ The bonding adhesion of the matrix to the filler is especially important when the filler is a short fiber material. For uniaxial composites (fibers aligned in one direction), the longitudinal tensile strength is increased independent of the fiber-matrix bonding. However, the transverse tensile strength and flexural strength increases are dependent on the fiber-matrix bonding.²⁵

The strength properties of a composite material are not linearly related to the bonding between the matrix and the filler. Excessive bonding between the fiber and the matrix can cause the composite to take on undesirable properties of the filler material (e.g., brittleness).²⁵ Therefore, degree and type of bonding between the matrix and the filler is a key factor in creating a structural polymer based composite. The next section describes an ideal filler for polymer composites.

2.4 Early Carbon Nanomaterials

The earliest reports of vapor-grown carbon fibers are from a patent dating back to 1889, which stated that “hair-like carbon filaments” had been grown from methane decomposition in an iron crucible.²⁸ These “hair-like carbon filaments” could only be analyzed after the invention of the electron microscope 50 years later. In 1960, the first

submicron particles were created using arc, plasma, and chemical-flame furnaces. Another work was published in 1960 where there was research done on the carbon arc.²⁹ In a 1960 publication, Bacon, *et al.* melted graphite under high temperatures and pressures, and noted the observation of nanowhiskers in his samples with scanning electron microscopy (SEM).²⁹

There was a lull in research until 1976, because the “hair-like carbon filaments” which considered an undesirable by-product. Research activity picked up again after Oberlin, *et al.*’s 1976 study of filamentous growth of carbon fibers through decomposition of benzene gas. This paper states “filaments have been found to be hollow tubes with the carbon layers parallel to the fibre axis and more or less bent cylindrically so that their c axis should be perpendicular to the filament axis.”³⁰ In the 1980s there were several new discoveries. The Buckminsterfullerene, C₆₀, was discovered in 1980.³¹ In 1987, a US Patent appears to have produced carbon nanotubes by catalytic procedure, however, without mention of carbon nanotubes, but again Kroto, *et al.* describe carbon fibrils.³²

It wasn’t until 1991 that Sumio Iijima discovered and launched the carbon nanotube research area. Iijima found that carbon fibers in a carbon arc were hollow and on the nanoscale in size³³. This led to the expansion and continuation of research on nanotubes, which has allowed for numerous developments in many fields of study, such as catalyst synthesis, medicine, and electronics.³⁴⁻³⁷ The next section briefly introduces these unique carbon nanomaterials.

2.4.1 Fullerenes and Carbon Nanotubes

Carbon atoms have the ability to form different configurations and electron states to create various polymorphs.³⁸ The four valence bonds have a weaker attraction force than the two inner electrons, thus causing the electrons to mix and reduce their energy by creating a hybrid orbital called hybridization.³⁸ The two main types of hybridization seen are the sp^2 and sp^3 hybrid bonds. For sp^3 bonds typically found in diamond, the valence electrons from the $2s^2$, and $2p_{xyz}^2$ atomic orbitals combine, creating 4 new bonds called sigma bonds, which create a tetrahedral bonding structure. For a sp^2 bond typically found in graphite, the valence electrons from the $2s^2$ and $2p_{xy}^2$ combine to form 3 new bonds called sigma bonds. The remaining $2p_z$ orbital forms a pi bond, giving the carbon a trigonal planar bonding structure. The different bonding of the polymorphs leads to different properties and the formation of different chemical structures.

Carbon nanotubes and fullerenes are composed of sp^2 hybrid bonds like those of graphite; these differ from the sp^3 hybrid bonds that form diamond.²⁸ The sp^2 hybrid bonds are stronger in-plane bonds than the sp^3 hybrid bonds in diamond and give the nanotubes their unique strength.²⁸ This strength, surpassing that of diamond, makes carbon nanotubes a ideal reinforcing material for composite materials.

Carbon fullerenes are large, close caged carbon molecules that come together to form a sphere. The C60 molecule was discovered in 1985 by Richard Smalley,³¹ and became known as the “bucky ball.” The spherical molecule took on its name due to its unique structuring of carbon molecules that resembles that of a soccer ball.³⁹ It has 60 carbon atoms that are bonded together, creating 20 faces. These faces are made up of

pentagons and hexagons creating this icosahedral-shaped object,³⁹ illustrated in Figure 2.1.

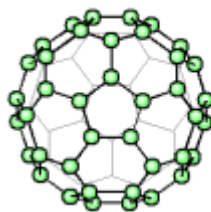


Figure 2.1 C60 Fullerene Molecule³⁹

The fullerene molecules were discovered purely by accident. In attempting to confirm the formation of polynes by time-of-flight mass spectrometry, two additional unidentified peaks were discovered. These peaks were located at mass 720, and a smaller peak located at mass 840. These peaks correspond to 60 and 70 carbon atoms, respectively. After more analysis and experiments it was determined that Kroto, *et al.* had a spherical structure made up of 60 carbon atoms with 12 pentagons and 20 hexagons forming what is known now as the “bucky ball.”^{31, 40}

The name, nanotube, is fitting, because a nanotube is only about a few nanometers wide and has a range of lengths. Typically, the length is significantly greater than the width, creating a large aspect ratio. A nanotube has a similar structure to a fullerene, but instead of forming a sphere like the fullerene atom, the atoms form a cylindrical tube that may (or may not) be capped off at each end by half a fullerene molecule.^{36, 40} Due to this unique and variable structure carbon, nanotubes are ideal filler material for polymer composites.

There are three different types of carbon nanotubes: single-walled carbon nanotubes (SWNTs), double walled carbon nanotubes (DWNTs), and multi-walled carbon nanotubes (MWNTs). A single-walled carbon nanotube contains one graphene sheet that rolls up to form a cylinder; a double walled carbon nanotubes contains two graphene sheets (one within another rolled up to form a cylinder); and a multi-walled carbon nanotube consists of several concentric cylinders. These three different types of carbon nanotubes are illustrated in Figure 2.2.

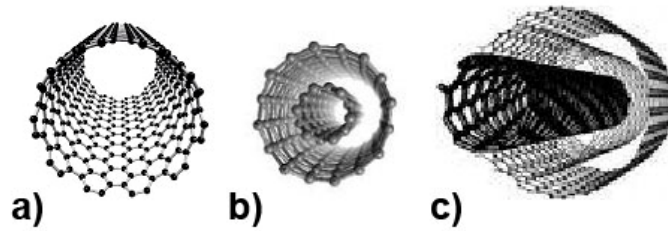


Figure 2.2: Illustrates the three different types of carbon nanotubes a) single walled b) double walled and c) multi-walled

The sidewalls of CNTs consist of only hexagonal carbon rings, whereas the end caps are made of pentagons and hexagons in order for curvature to exist. Due to the carbon-carbon bond symmetry of the cylindrical tube, CNTs have a discrete number of orientations (Chirality) that can form a closed cylinder, which is illustrated in Figure 2.5.

Figure 2.3 illustrated that there are only a select number of atoms that can be chosen (in this case O and A, or B and B') in the two dimensional graphene sheet to form a completely carbon nanotube. Thus, when the sheet is rolled up these atoms are next to each other, and determine the chirality (manner in which the sheet rolls up) of the carbon nanotube.

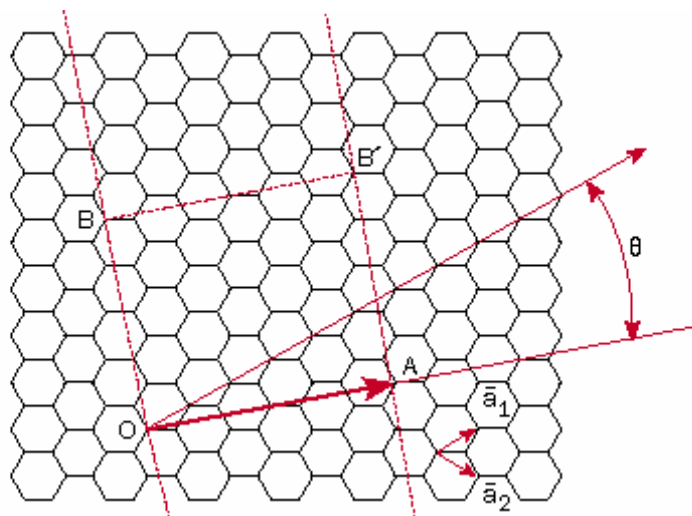


Figure 2.3: Graphene Sheet illustrating Chirality

2.5 Carbon Nanotube Properties

It was mentioned earlier that three of four valence electrons of carbon, one s-electron and two p-electrons, form the sp^2 -hybrid, which has trigonal planar σ bonds. In the bulk, these σ orbitals form strong covalent bonds with the σ orbitals from neighboring carbon atoms. The fourth (i.e., the third 2p) electron is in a $2p_z$ -orbital perpendicular to the plane and forms a weaker π bond with the $2p_z$ -orbitals of neighboring C atoms. The resulting π -bonds define the Fermi surface. Hence, they are responsible for the transport properties,⁴¹ but the π -bonds are also the reason that the carbon nanotubes aggregate. In contrast, the mechanical properties are a result of the strong covalent bond between the tightly bound σ -orbital.

In this section, the mechanical properties of SWNTs and MWNTs and their chemical reactivity will be addressed.

2.5.1 Mechanical Properties of Carbon Nanotubes

The Young's modulus of a composite material is related to the cohesion of the constituent building blocks,⁴² i.e., the adhesive forces between the polymer matrix and the filler determine the properties of the composite. Therefore, good adhesion will result in high load transfer and a composite with superior properties.^{43, 44} It has been assumed that composites reinforced with carbon nanotubes (either SWNTs or MWNTs) could be stronger and lighter than matrices otherwise reinforced with carbon black, metallic powders, or glass fibers with metal coatings.⁶⁻⁸

However, testing and calculating the mechanical properties of CNTs have proven to be very challenging, because of the difficulty in reproducing test results. The difficulties lies in the ability to isolate on single CNT and the mechanical properties of CNTs are dependent upon the perfection of the carbon nanotube structure.^{45, 46} Therefore, the differences in lattice perfection (or imperfection) would yield different results. Another major reason for the discrepancy of reported values is due how the stresses on the carbon nanotubes are determined (area of a carbon nanotube).⁴⁷

The Young's modulus of graphene sheets has been calculated using several different methods: transmission electron microscopy, atomic force microscopy, and mathematical modeling. It was determined that SWNTs have an average elastic modulus and tensile strength of 1.06 TPa^{3, 48-51} and 20 GPa, respectively.⁵² There have been different studies on the empirical lattice dynamics model of CNTs that have determined an elastic modulus of approximately 1060 GPa.^{50, 53, 54} A more detailed list of the varying SWNT mechanical properties is shown in Table 2.1.

Table 2.1: Young's Modulus Data for SWNT and MWNTs

Researcher	Technique	Young's Modulus	Type of CNT
Ruoff ⁵⁵	Graphite in-plane modulus	1.06 Tpa	SWNT
Yu ³	AFM	0.320-1.470 TPa	SWNT
Yu ³	AFM	0.270 - 0.950 TPa	MWNT
Krishnan ⁴⁹	TEM	1.3 ± 0.06 TPa	SWNT
Salvetat ⁵¹	AFM	$.80 \pm 0.41$ TPa	SWNT
Wong ⁵⁶	AFM	1.28 ± 0.59 TPa	MWNT
Lu ⁵⁰	Dynamic Modeling	0.1 TPa	SWNT
Tracey ²	TEM	1.8 ± 0.9 TPa	MWNT
Goze ⁴⁸	Modeling	1.24 TPa	SWNT

The Young's modulus data shown in Table 2.1 illustrate the large variance in data across different techniques and samples. The large variance in data illustrates two things. First, the methods for testing need to be refined in order to get reproducible measurements of the Young's modulus for CNTs. Second, there is a potentially large deviation in the moduli of the different carbon nanotubes, and that the purification and perfection of the tubes play roll in the carbon nanotube strength.^{57, 58}

2.5.2 Carbon Nanotube Reactivity

It is thought that carbon nanotubes will be more reactive than their counterpart, a planar graphene sheet.⁵⁹ They are thought to be more reactive, due to the curvature of the tube, since such curving results in a pi bonding orbital mismatch, which is illustrated in Figure 2.4.

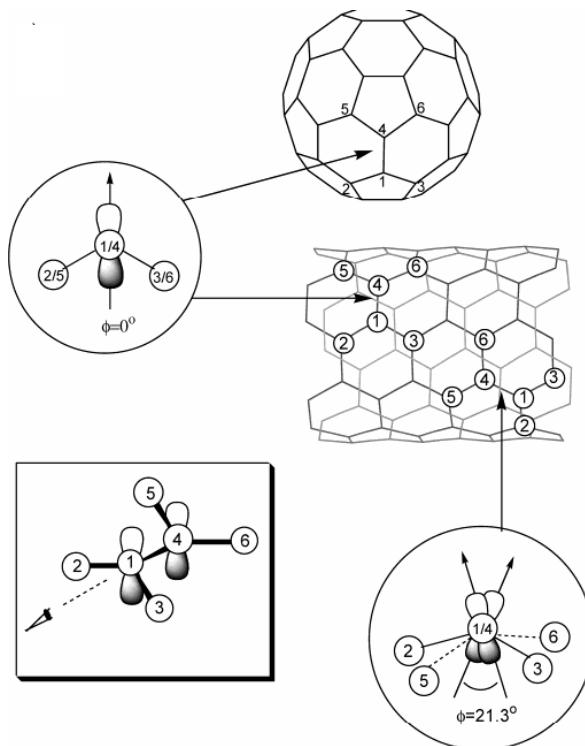


Figure 2.4: Mismatch Between π Bonding Orbitals in a Nanotube⁵⁹

For this very reason, the caps of the carbon nanotubes, resembling a fullerene, have a higher reactivity than the sidewall.⁵⁹ Tubes that have no end caps are also very reactive. Taking a closer look at the bonding of a carbon atom in the sidewall and that of a carbon atom in an end cap, they all have three bonds to the nearest neighbor. However, carbon atoms at the end of an open-ended tube only have two bonds.⁵⁹ Therefore, it is easy to introduce molecules for functionalization to the structure at the end caps.

This high reactivity of carbon nanotubes is the reason they tend to naturally align and aggregate themselves into “ropes.” These ropes are generally 30 nm in diameter, and are made up of several hundred tubes which can be highly entangled.⁶⁰ This is also due to the van der Waals forces between the carbon nanotubes. Van der Waals forces are the weakest type of intermolecular forces and are created by the attraction between induced dipoles in a nonpolar molecular. However, due to the small size of the nanotubes, the van der Waals forces become more of a problem and cause the tubes to cluster.

The van der Waals forces on a carbon nanotube are dependent upon the length, but scales at 36 KT/nm.⁶¹ Van der Waals attractive forces have a wide range of influence ranging from a distance of two angstroms to as far apart as one thousand angstroms.³³ The effect of van der Waals forces must continually be calculated with the addition of new particles; the more particles there are in a solution, the larger the difference in van der Waals forces from just two initial particles.³³ Since the van der Waals forces are relatively weak, there is a certain “ideal” distance that is needed to either cause attraction or repulsion between the carbon nanotubes, Figure 2.7

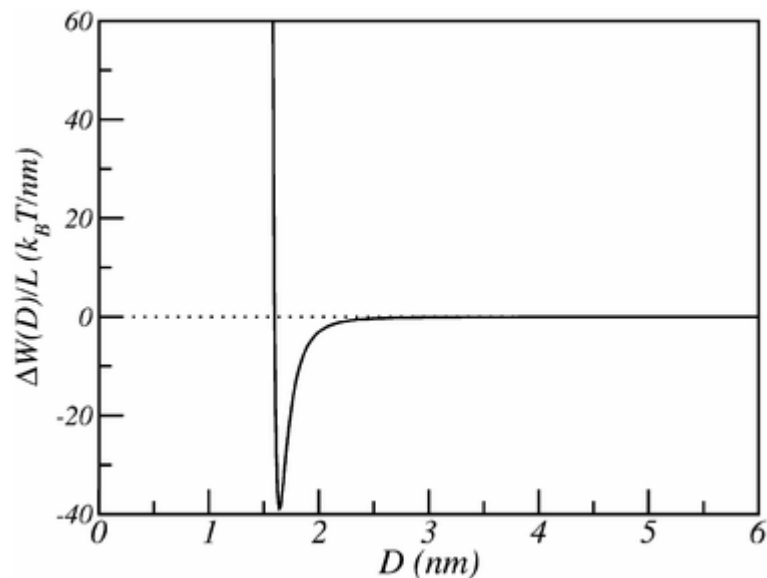


Figure 2.5: Potential of interaction between two parallel SWNTs as a function of the distance between them, as calculated by Girifalco et al.⁶¹ Note the very deep attractive well when the SWNTs are in contact.

The addition of commonly used solvents has been found to be successful in separating the tubes. The success is partly due to the intrinsic instability of the colloidal suspensions as a result of the van der Waals forces between the nanotubes⁸. The attractive force on the tubes has become very strong and can't be overcome by the repulsive forces of the solutions. Thus the solvent-nanotube suspensions are thermodynamically unstable (Figure 2.7).⁸

The use of surface active agents such as surfactants, polymers and other colloidal particles has been successful in preventing the aggregation of the tubes for long periods of time.⁸ The surface-active agents have the ability to lower the interfacial energy of the tubes by increasing repulsive forces (electrostatic and/or steric) and have the ability to alter the rheological surface properties, which contribute to increasing the stability of the colloidal suspension to a metastable form.⁸

Van der Waals forces are the reason MWNTs are able to remain encased within each other and keep from separating. The remaining un-hybridized p orbital creates van der Waals forces between the carbon nanotube layers. These forces are strong but, with enough force placed on the MWNTs, they can become unbundled. These forces also cause MWNTs to bundle, but they have been found to exist both individually and entangled, dependent upon their length.⁶⁰

2.6 Carbon Nanotube Polymer –Based Composite Properties

The idea of adding reinforcing material, or fillers, to polymers has been around for many decades. The reason for the creation of polymer composite materials came about due of the need for materials with specific properties for specific applications. For example, composite materials are unique in their ability to allow brittle and ductile materials to become softer and stronger. A soft plastic can become harder and stronger by the addition of a light weight high stiffness material.

The ideal reinforcement material for a polymer, which is characterized as a very ductile material, is a highly rigid material with a large elastic modulus. The mechanical properties of carbon nanotubes, which were discussed in the previous section, illustrate their unique properties that allow them to be ideal reinforcement materials. This section will address the need for dispersion and alignment of the carbon nanotubes within the polymer matrix, and the potential problems with current carbon nanotube composite materials.

2.6.1 Carbon Nanotube Polymer- Based Composite Mechanical Properties

The determination of the mechanical properties of composite materials has proven challenging and remains a subject of debate. There are several methods that can be

employed to theoretically determine composite properties. These methods include; the rule of mixtures, the inverse rule of mixtures, and the modified rule of mixtures.⁶⁰ The previous rules estimate properties only by the composition of the composite, but mechanical testing is necessary, because the mechanical properties are dependent on many factors. The full potential of the material isn't fully understood until samples can be made and mechanical tests can be performed.

The mechanical properties of carbon nanotube composites are largely dependent upon the quantity of CNTs in the system, the dispersion and alignment of the tubes, and the interfacial bonding between the carbon nanotubes and the matrix.¹ The ability to determine the precise amount of carbon nanotubes needed to increase the stiffness is just the beginning. Therefore, there is a need for these carbon nanotubes to be dispersed, aligned, and have favorable interactions with the matrix material.

2.6.2 Dispersion of Carbon Nanotubes

There are several different methods for dispersing carbon nanotubes, and the determination of the ideal method proves challenging. These methods utilize polymers, surfactants, acids, or a combination of several different materials to disperse carbon nanotubes.⁶²⁻⁶⁴ Several of these methods tend to utilize hazardous materials and lengthy procedures to produce the desired result, while others require less dangerous materials with shorter durations to produce a similar result.^{5, 6, 62-74} Therefore, these less dangerous methods used to disperse carbon nanotubes may not be thought of as “ideal methods.” Typically all of the methods utilize some degree of sonification, from a few minutes to several hours, to initially mechanically disperse the carbon nanotubes. This method of

mechanical dispersion in conjunction with these surface active agents reduces the van der Waals forces, provided that, the dispersing agent can separate the carbon nanotubes to prevent re-aggregation.^{71, 72} However, this method, sonification, can actually damage the carbon nanotubes, and the longer the carbon nanotubes are placed in sonification, the greater the probability of damage.⁶⁸ Therefore, in order to determine the most accurate method of dispersion, research must be conducted to determine ideal dispersing agents and sonification time period.

The ability to determine an ideal dispersing agent for carbon nanotubes has been the subject of many studies. Most notable approaches consisted of either the use of surfactants^{5, 6, 65, 71, 72, 74, 75} or polymers.^{64, 66, 69, 70, 73} Matarredonna, *et al.*⁵ studied the effect of chemical modifications to the surface of carbon nanotubes. This research found that adding an anionic surfactant sodium dodecylbenzene sulfonate (NaDDBS) to the suspension results in the exfoliation and dispersion of the carbon nanotubes. Conversely, since the experimental procedure involves the sonification of the SWNT suspensions, it is also quite likely that this generates considerable exfoliation of the nanotubes, followed by the adsorption of the surfactant molecules, which in turn, stabilizes the nanotubes due to steric repulsion.^{69, 71-73}

Moore⁶⁹ studied the dispersion of carbon nanotubes in various anionic, cationic, and nonionic surfactants, as well as polymers. It was determined that polymers with higher molecular weights were able to facilitate the dispersion of higher amounts of carbon nanotubes. In this study, it was determined that using a Pluronic[®] (multi-block co polymer, specifically polyethylene oxide – polypropylene oxide – polyethylene oxide, PEO-PPO-PEO) at varying molecular weights, led to a disperse solution of CNTs.⁶⁹

They further determined that higher molecular weights of the hydrophilic group (PEO) led to better dispersions when compared to other polymers with lower molecular weight hydrophilic groups or high molecular weight hydrophobic groups. This is due to the fact that hydrophilic groups extend into the water, impeding the carbon nanotube aggregation.⁶⁷ Therefore, it works to increase distance between the carbon nanotubes reducing the van der Waals forces (Figure 2.5). This type of stabilization doesn't occur in ionic surfactant solutions, because the surfactant systems work on charge repulsion.⁶⁹ This procedure, like the previous one, involves the mechanical separation of the carbon nanotubes through sonification, which allows the polymer to coat the carbon nanotubes.

Even after years of research, the knowledge that has been gained to adequately disperse carbon nanotubes, and create a usable carbon nanotube composite has fallen short.^{57, 76-80} The problem lies in the ability to keep the carbon nanotubes dispersed after they are placed in the matrix material. This remains a problem due to the complexity of polymer solutions. Currently, there are two methods used to incorporate the carbon nanotubes into a polymer matrix. The first method combines the dispersing agent and carbon nanotubes into the polymer matrix, and the second removes the dispersing agent prior to addition into a polymer matrix.^{4, 58, 81-84} It has been found that combining the dispersing agent and carbon nanotubes into a polymer matrix present the most potential in creating a well-dispersed composite.⁵⁸ This research, in addition to dispersing the CNTs was to determine an ideal methodology for creating a carbon nanotube composite. Since CNTs have a large uniaxial modulus, in addition to dispersion, it would prove useful to align the carbon nanotubes to make CNTs more effective as a reinforcing material.

2.6.3 Alignment of Carbon Nanotubes

The alignment of carbon nanotubes is also of great importance when attempting to determine the properties of carbon nanotube composites because of the carbon nanotubes' mechanical properties. Carbon nanotubes are uniaxially strong, and like their predecessor, carbon fiber, prove to be useful if the fibers are aligned in a uniaxial direction. There has been a significant amount of research on the alignment of carbon nanotubes as synthesized⁸⁵⁻⁹² or aligned^{74, 93-112} during polymerization. It has been shown, however, that randomly oriented carbon nanotubes embedded in polymer matrices, failed to generate composites in which the full potential of the mechanical properties of the nanotubes is exhibited.⁵⁴

There have been recent advancements in fabricating aligned carbon nanotube composites where the alignment occurs in the synthesis process.^{102, 113} The methods essentially add polymer into the synthesis process to create the composite and keep the alignment of the carbon nanotubes intact.^{102, 113} These methods have proven very useful, but they have little ability to tailor geometry or create large bulk samples.

There have been significant amounts of research on the alignment of carbon nanotubes as fillers in a polymer matrix.^{4, 54, 76, 77, 79, 81, 114-117} However, there has been only minor advances using small weight fraction of carbon nanotubes, and none of the research has produced a composite with properties close to the theoretical mechanical properties.⁷⁶ Some of the advances in creating aligned carbon nanotube composites are via melt spinning and drawing.¹¹⁸ However, even these composites have limitations due

to the amount of nanotubes that can be processed, and the final product doesn't compare to the theoretical estimates^{98, 118, 119}.

Other methods of alignment such as electrospinning and solution spinning have been found to create well-aligned samples of carbon nanotubes¹²⁰. Chae, *et al.*¹²⁰ was able to create samples that had almost 99% aligned carbon nanotube samples.¹²⁰ These samples were made with very low weight fraction of carbon nanotubes, but even in these well-aligned samples, the increase to the storage modulus of the materials was relatively low compared to that of the expected increase¹²⁰. Research done by Kim, *et al.*¹⁰⁰ has found that creating porous aligned carbon nanotube-polymer composites through electrospinning has yielded increased stress placed on the fibers versus the matrix enhancing the modulus of the materials.¹²¹

There have been numerous attempts to achieve simultaneous alignment and dispersion of carbon nanotubes, but none of these methods have proven successful in producing the truly perfect carbon nanotube polymer composite that is theorized. The reason for the inability to create a strong material even with well aligned carbon nanotubes remains unclear, but it stems from the variation in carbon nanotube mechanical properties, perfection of the carbon nanotube structure, and adhesion between the matrix and the carbon nanotube. The next section will address novel techniques for aligning carbon nanotubes in a straight forward consistent manner.

2.6.4 Novel Approach to Disperse and Align Carbon Nanotube Polymer-Based Composites

The approach that was used in this research was to initially disperse the CNTs in surface-active suspension, incorporate them within an epoxy matrix, and then align the carbon nanotube-polymer composite. The approach of initially dispersing the CNTs and then placing them into the polymer matrix to be aligned in situ was done to alleviate problems that occur when carbon nanotubes are aligned prior to embedding.^{57, 58, 76-79, 109} First, the research addressed the need to determine the most adequate dispersing agents by testing the ability of the dispersing agents in a suspension and in polymer solution. The dispersing agents used in the research were chosen based on previous research because of their ability to create a dispersed CNT suspension or lead to an increase in carbon nanotube-polymer composite properties.

The three dispersing agents used were sodium dodecylbenzene sulfonate (NaDDBS),⁵ Pluronic[®] F108 (polypropylene oxide block polyethylene oxide block polypropylene oxide),⁶⁹ and a commercial dispersing agent Disperbyk 2150.⁴ The three suspensions were studied to determine the ability to disperse the CNTs, and they were then made into epoxy composite materials in order to determine the effects of the dispersing agents on the final composite properties. This method allowed for the determination of a well rounded dispersing agent, and analyzes the effects of the dispersing agent in the epoxy matrix while still dispersing the carbon nanotubes. Since very small volume fractions of the dispersing agents are used, it is thought that there would be minimal unfavorable interactions between the matrix and the dispersing agent.^{122, 123}

The next step in the research was to take the knowledge from the dispersing study and create aligned carbon nanotube composites. There were two methods of alignment chosen in this research: shear flow and magnetic alignment. Shear flow has been studied by others to create an aligned carbon nanotube composite.^{111, 112, 124-126} It has been found in all previous research that shear flow does align the carbon nanotubes in a variety of matrix materials and shear flow set ups. However, this shear flow research is incomplete because of limited sample geometry and matrix material used. This research creates a bulk aligned carbon nanotube polymer-based composite that can be used for a variety of structural applications.

In addition to using shear flow as a method of alignment, this research also utilized alignment from an applied magnetic field. Previous research has found that the application of a magnetic field has been able to align polymers and polymer carbon nanotube composites.^{123, 127-133} The reason for the alignment of carbon nanotube composites in a magnetic field is not completely understood. The composites typically result in a moderate degree of carbon nanotube alignment. The reason for the lack of CNT alignment is that carbon nanotubes are not magnetic and will not align in a magnetic field on their own.^{97, 134, 135} Even though carbon nanotubes do not align on their own in a magnetic field, with the cooperative influence of other aligning fibrous networks, such as a polymer matrix,^{134, 136} or with an outside influence of tethering to them a magnetic material,¹³⁴ the carbon nanotubes will align. Thus, the focus of this work is to tether iron oxide nanoparticles to the carbon nanotubes in order to induce alignment while embedded in a polymer matrix.

CHAPTER 3

MATERIALS AND CHARACTERIZATION OF MATERIALS

3.1 Overview

This chapter discusses the materials used and background of several different characterization methods. Section 3.2 briefly discusses the materials that were used in this research. Section 3.3 discusses the background of transmission electron microscopy. Section 3.4 briefly describes the history and background of Raman spectroscopy for use with carbon nanotubes. Section 3.5 describes the two different mechanical property techniques, dynamic mechanical analysis and compression testing, used to characterize the composite materials in this research. Section 3.6 describes the background of differential scanning calorimetry when working with polymeric materials.

3.2 Materials

3.2.1 Carbon Nanotubes

This project utilized two types of carbon nanotubes. The work described in Chapter 4 utilized SWNTs as purchased from Carbon Nanotechnology, Inc. in high purity form (> 90%). The carbon nanotubes were synthesized by the laser ablation process with 1-2 nanometer diameters. The remaining chapters utilized SWNTs as purchased from Sigma Aldrich, in high purity form (>90%). The carbon nanotubes purchased from Sigma Aldrich, were analyzed to have 1-2 nm diameters and have varying lengths

between 1-2 microns. The tubes were analyzed using Raman spectroscopy and high resolution TEM.

3.2.2 Surfactant Sodium Dodecyl Benzene Sulfonate

Sodium dodecyl benzene sulfonate (NaDDBS), molecular weight of 348.48 g/mol) purchased from TCI was used in this research. The concentration used, 1.2 mMol NaDDBS, in this research was based on methods as described in Matarredona, *et al.*¹⁹

3.2.3 Commercial Block Copolymer Dispersing Agent

Disperbyk 2150 a commercial dispersing agent from BYK Cheme, Inc. was in solution as purchased. The solution is a 52wt% BCP with 1-methoxy-2-propylacetate as a solvent. The product is proprietary in nature, but is known to be a styrene based BCP with basic pigment affinic groups with an amine value of 57 mg KOH/g. The concentration used, 5 mg BCP, in this research was based on the methods described in Li, *et al.*⁴

3.2.4 Pluronic F108

The Pluronic F108, PEO-PPO-PEO triblock copolymer, was purchased from BASF with a PEO molecular weight of 11,680 g/mol, and a total molecular weight 14,600 g/mol. It was used in the same concentrations (2wt%) as described in O'Connell, *et al.*⁶

3.2.5 Carboxymethyl Cellulose

Carboxymethyl Cellulose sodium salt (CMC) was purchased from Sigma-Aldrich, with an average molecular weight of 250,000 g/mol and a density of 1.2 g/cc. The CMC was used at 1 wt% concentrations in an aqueous solution with a viscosity ranging from 3,000-6,000 cp.

3.2.5 Sol Gel Precursor Materials

Ferric nitrate nonahydrate, $\text{Fe}(\text{NO}_3)_3 \cdot 9\text{H}_2\text{O}$; ferric trichloride hexahydrate nonahydrate, $\text{FeCl}_3 \cdot 6\text{H}_2\text{O}$; and propylene oxide (PO), $\text{C}_3\text{H}_6\text{O}$, were purchased from Fisher Scientific and used as received.

3.3 Transmission Electron Microscopy

Transmission electron microscopy was used to determine dispersion, alignment, and attachment of metal particles in the nanotube samples. High-resolution transmission electron microscopy (HRTEM) images were obtained from a Hitachi HF 2000 FE TEM with an accelerating voltage of 200.0 keV. The most basic idea of a TEM is an electron beam, which is transmitted through a specimen that must be less than 200 nm thick, in a stable high vacuum system²⁴. TEM produces a two-dimensional projection image of the three-dimensional structure seen in experimentation. The samples can be magnified between 100-100,000 times¹³⁷. Using the TEM, it can be determined the length and diameter of the nanotubes themselves can be determined. The TEM can also be used to determine relative dispersion of samples. There were two different methods for

collecting samples: using epoxy to adhere the grid onto a wire to collect a sample in motion and dropping droplets of sample directly onto the grid.

The amount of the sample on the TEM grid is dependent upon the concentration of the solution. Therefore, the ability to analyze the solution remains dependent upon the ability to prepare an adequate TEM sample grid. An adequate sample grid will be composed of a thin layering of solution. Too dilute a solution will yield an insufficient sample, and too concentrated of a suspension will yield too thick a sample. However, typically there are areas within a sample that can determine the clustering or dispersion of the nanotubes. Other complications with the resolution of the TEM can come from diffraction aberrations, chromatic aberrations due to unstable beam or lens current, astigmatism, or spherical aberrations due to lens imperfections¹³⁷. In addition to using the equipment to its fullest potential, the sample used can prove to hinder TEM resolution. The TEM provides very useful information for crystalline materials.^{138, 139} In particular polymer crystallite size and structure, voids, phase changes, and structure changes can be determined using a TEM. However, it is well known that amorphous materials are more difficult to analyze using the TEM.^{138, 139} The difficulty lies in the interactions of the electron beam and the polymer. These interactions lead the polymer backbone chain to break and side groups to break off, resulting in free radicals and new structures.^{138, 139} Therefore, analyzing the structure of an amorphous polymer in TEM is not ideal.

3.4 Raman Spectroscopy

Raman spectroscopy is one of the most powerful tools for characterizing carbon nanotubes. Raman scattering is the weaker of two types of scattering, Rayleigh and

Raman scattering. Rayleigh scattering is the light that is scattered elastically in all directions by molecules, and is the most well known type of scattering.¹⁴⁰ Raman scattering is the inelastic scattering of light by molecules. This type of scattering provides information about the vibrational and rotational energy levels of the molecules causing the scattering.¹⁴⁰ There are two types of Raman scattering, Anti-Stokes and Stokes scattering.

Anti-Stokes lines are the high frequency form of Raman scattering and represent the scattering of a molecule that is in the excited state and results in a scattered radiation less than the incident radiation. Stokes lines are the low frequency form of Raman scattering and represent the scattering of a molecule that is in the ground state, resulting in a higher scattering radiation than incident radiation. (See Figure 3.1.¹⁴⁰) Raman scattering is useful because it is a direct measurement of the vibrational energies of a molecule, where the increase or decrease in scattered energy is related to the vibrational energy spacing of ground state molecules. Raman scattering has a direct relationship between the incident light and the intensity of the spectrum. The higher the power of the laser the more intense the spectrum is, whereas the weaker the laser the weaker the spectrum or intensity.¹⁴⁰

Raman spectroscopy remains very useful for studying carbon nanotubes because it allows the determination of the diameter, diameter distribution, defects, load transfer, electronic state, alignment, and other information. Raman is also a very useful tool due to its non-destructive nature.¹⁴⁰ Another major reason Raman spectroscopy is very useful for carbon nanotubes is the information obtained by resonance Raman.³⁹ By tailoring the wavelength of the laser to the energy separation distance between the valence and

conduction band of the carbon nanotubes (the band gap varies between tubes, see Figure 3.1) the intensity of the spectra becomes amplified.³⁹

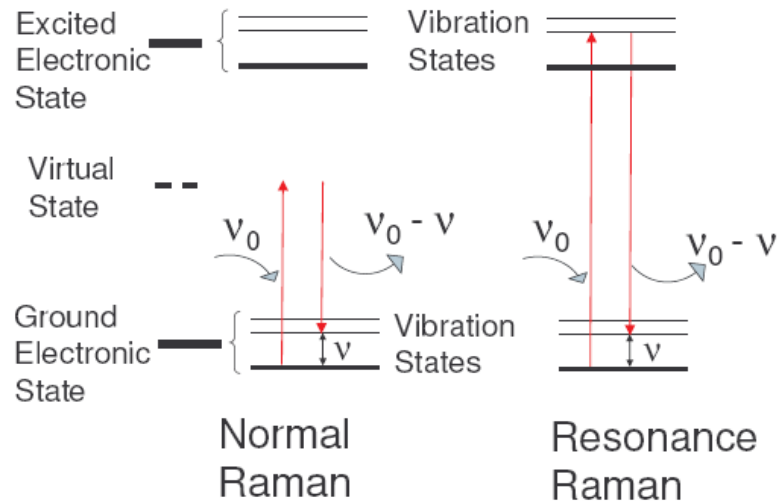


Figure 3.1: The difference between normal and resonance Raman.¹⁴⁰

There are four main characteristics of the carbon nanotube Raman spectra that are used to understand and evaluate the carbon nanotubes. Figure 3.2 illustrates the four peaks found in the Raman spectrum. The four main Raman features of CNTs are the radial breathing mode (RBM), the disordered induced D-band, the tangential G-band, and the G' band (disorder overtone of D band).^{39, 141} The radial breathing modes are found between $150\text{-}350\text{ cm}^{-1}$ for SWNTs, however, this band tends to disappear for MWNTs^{39, 141}. This band is related to the diameter of the carbon nanotubes where as the frequency of the radial breathing mode is inversely proportional to the diameter.

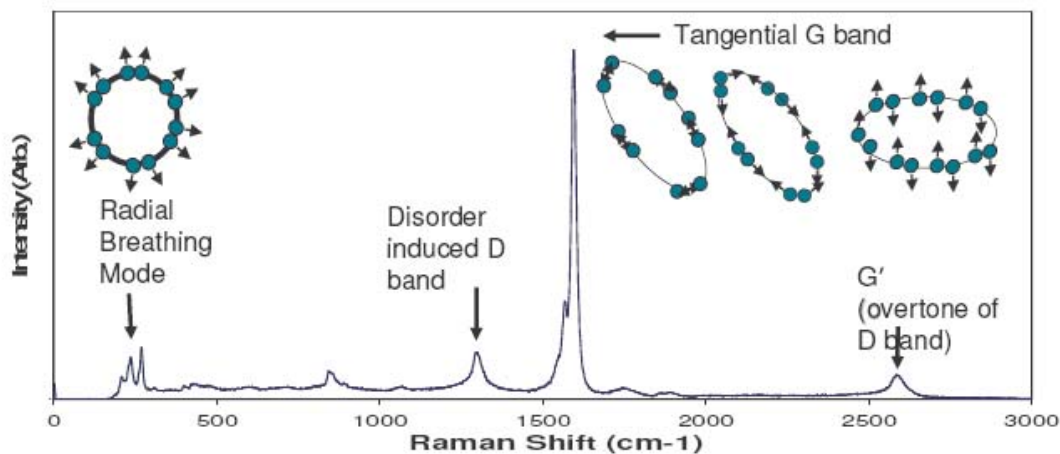


Figure 3.2: The ideal Raman spectrum for carbon nanotubes

The G band is located near 1600 cm^{-1} and can be used to determine the orientation of the carbon nanotubes in a composite by measuring the Raman spectra at angles $0\text{-}90^\circ$. The peak is at its highest intensity when the carbon nanotubes are parallel to the incident beam, and the weakest intensity is when the carbon nanotubes are perpendicular to the incident beam.¹⁴¹⁻¹⁴³ The G band peak also allows for the determination of the carbon nanotube type, metallic or semiconducting, of the carbon nanotube being observed. The peak broadens for semiconducting tubes and narrows for metallic tubes, allowing the tube type to be distinguished.^{144, 145}

The D-band, which is found in the range of $1250 - 1450\text{ cm}^{-1}$, is due to the defects within the carbon nanotubes. This band illustrates the differences between a perfect carbon nanotube (low intensity) and an imperfect carbon nanotube (high intensity). This peak also changes with the functionalization of carbon nanotubes, because sidewall functionalization generally occurs on defect sites. This band works in conjugation with the G' band, the defect overtone, located between $2500\text{-}2900\text{ cm}^{-1}$, and

originates from defects. The load transfer between CNTs and the matrix shifts this band, allowing the composite-filler interaction to be determined.

3.5 Mechanical Property Characterization

The mechanical behavior of materials is an important property to study because it provides quantitative analysis of how a material will perform under loading conditions. There are several different types of tests that can be used to characterize the mechanical behavior of a material. In section 3.5.1, the use of dynamic mechanical analysis to determine polymer properties will be discussed in detail. In section 3.5.2, the use of compression testing to determine properties will be discussed.

3.5.1 Dynamic Mechanical Analysis (DMA)

The properties of polymers are both dependent on time and temperature making understanding the dynamic mechanical analysis of polymers and polymer blends very important.¹⁴⁶ The dynamic mechanical properties of polymers allow the temperature dependence of the dynamic modulus to be determined and give other structural information.¹⁴⁶ DMA can determine the dynamic viscoelastic behavior with temperature dependence of polymers allowing the overall performance of the polymer to be evaluated.¹⁴⁶

DMA can test over a large range of temperatures and frequencies allowing the difference in storage, loss, and tan delta to be evaluated graphically. DMA can test the frequency two different ways, with a free vibration or fixed vibration. In the case of free vibration, the frequency is applied and allowed to decay, whereas in fixed vibration it is maintained over the entire test.

The sample then has an oscillatory (sinusoidal) strain or stress applied to it, resulting in a stress or strain in the material, respectively. In viscoelastic materials there is partial Hookean and partial Newtonian flow giving rise to a delay in the strain rate. The strain rate can vary from 0 - 360° from that of the stress, with rates greater than zero degrees and less than ninety degrees causing interference in the data.¹⁴⁷ An illustration of this can be seen below in Figure 3.3.

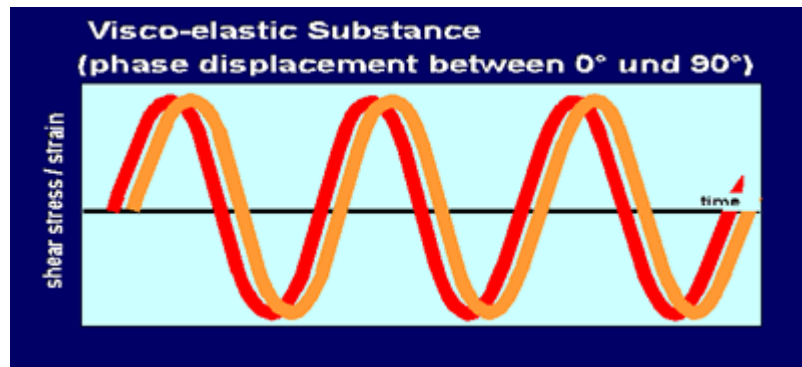


Figure 3.3: Viscoelastic Stress-Strain Relation²⁷

There is variation in the DMA data within each data set, and these variations allow us to understand the cohesion of the composite samples being tested, and we can learn from this variation. If the samples are being made consistently uniform, the properties remain consistent between samples. However, if there are large variations from sample to sample, then this indicates that the samples are not being made uniformly.

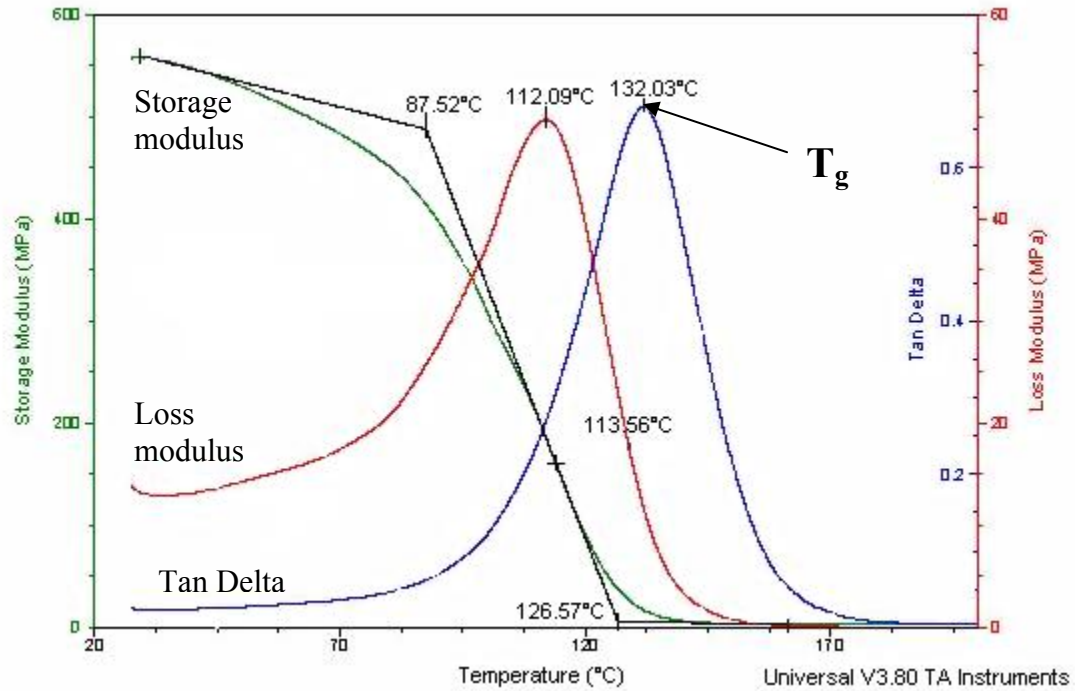


Figure 3.4: Typical DMA Plot

In addition, the results from collected DMA data can be compared, see Figure 3.4, to that of currently used composite materials. The data can also be analyzed to illustrate the change in loss modulus, storage modulus, and tan delta of a material with change in temperature to determine ideal composite compositions. DMA not only allows the determination of structural properties, but specific points of interest (e.g., T_g). The T_g of the polymer sample corresponds to a transition point as the sample goes from glassy to rubbery states, and its properties change.

3.5.2 Compression Testing

Compression testing is theoretically the exact opposite of simple tension. The stress-strain relationship of the material is characterized by measuring the response of the material as a load is applied. This test, unlike DMA, works best preformed until sample

failure, giving rise to a large amount of data: compressive yield stress, compressive ultimate stress, compressive modulus of elasticity, toughness, and deformation properties^{148, 149}.

The idealized relationship for stress and strain is relatively simple, but becomes more complicated when taking into account real systems. The stress-strain relationship⁷ is:

$$\sigma = \frac{F}{A} \quad \text{and} \quad \varepsilon = \frac{\Delta l}{l} \quad (\text{eqn 3.1})$$

Where stress, σ , equals uniaxial force, F , divided by the cross-sectional area, A , of the sample, and strain, ε , is the relationship of the change in length of the material, Δl , divided by the sample length, l . Thus, the sample geometry plays a very important role in testing and in calculating stress and strain. Typical sample geometries that are used in compression testing are cylinders or prisms. To get optimal data, the sample should have a length twice its width or diameter and should be consistent within the sample set (i.e., all samples should have the same dimensions).^{148, 149}

There are two main types of stress, true stress and engineering stress. True stress is calculated from the instantaneous area while the sample is deformed, and engineering stress is calculated from the original area of the sample. This work is concerned with engineering stress. The stress-strain relationship is dependent upon the properties of the material, but can be classified by the material used.⁷ For instance, ceramics are typically brittle, metals are ductile, and plastics are tough, see Figure 3.5.

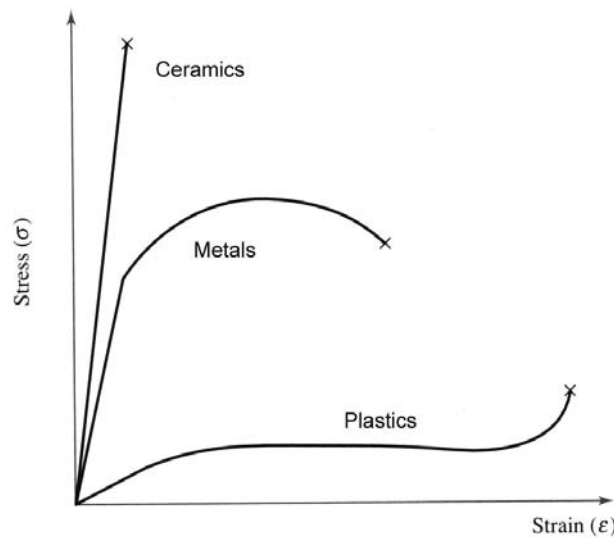


Figure 3.5: Stress-Strain relation for various types of materials⁷

The stress-strain data can be compared across several different samples tested under the same conditions, resulting in the determination of how compositional changes affect the material. Even within the same sample composition there can be inconsistencies between samples that could be influenced by residual stress, anisotropy, stress and strain gradients, and nonhomogeneity. Therefore, compression tests can determine how reliable the sample preparation between the different samples are by the changes in stress-strain relation.^{148, 149}

Testing can also be done at several different temperatures to determine the effect of temperature on the stress-strain properties. From this, a working temperature range can be determined for the material. This temperature range would then guarantee that the material will be able to perform properly.^{148, 149}

The samples in this research were tested using a MTS Insight 2. The samples were tested in compression using the 643 compression platens. The samples were tested at 25 °C and 100 °C to obtain information below and above the glass transition temperature. The sample geometry (4 mm squares) used was not an ideal geometry,¹⁴⁹ but was used to ensure consistent data for testing in both aligned and unaligned directions.

3.6 X-ray Diffraction

X – Ray diffraction (XRD) is used to identify materials by determining their crystallographic structure, and in this way it is a characterization tool on the scale of nanometers, and even angstroms, thus providing a high degree of accuracy.^{150, 151}

XRD works by shooting X-Rays and collecting reflected X-Rays at a known angle relative to the sample.^{150, 151} The scattered beam is used to determine the atomic structure of the lattice.^{150, 151} Lawrence Bragg was able to use the information from analyzing basic crystal materials, using X-Ray diffraction to determined that diffraction occurs from parallel planes in the target material.

Diffraction occurs on these parallel planes, based upon the distance between the planes, commonly called the d-spacing (d). From this information Bragg was able to determine the crystal structure using Bragg's Law (eqn 3.2), where the d value is characteristic of a specific material.

$$n\lambda = 2d \sin \theta \quad (\text{eqn 3.2})$$

In equation 3.2, n is an integer, d is the distance between atomic layers in the crystal (d-spacing), λ is the wavelength, and θ is the angle of incidence.^{150, 151} However, it is known that as the crystal size decreases from micrometers to nanometers, there is a broadening

of the XRD peaks. The broadening results from the decrease number of crystal planes that are being diffracted.¹⁵² This decrease in crystal planes is a result of less destructive interference at off Bragg angles from the bulk material, yielding broader peaks.¹⁵²

3.6.1 Small Angle X-ray Scattering (SAXS)

SAXS is a well-established analytical X-ray technique for the structural characterization of solid and fluid materials on a nanometer length scale.^{150, 153, 154} Applications of SAXS used can be found in structural biology, polymer science, colloid chemistry, catalyst development, and metallurgy.^{150, 155-161} This technique used in conjunction with imaging techniques (transmission electron microscopy), provides the ability to fully understand the microstructure on multiple levels (e.g. in solution).¹⁵⁵⁻¹⁶¹ Microscopy data yields a 2-dimensional image (or reduces 3D to 2D), leaving the need for assumptions to be made to completely analyze the particle size and morphology data.

It is known that SAXS is well developed for systems containing identical particles and can easily analyze aggregated particles, whereas in microscopy techniques aggregated particle analysis can be difficult to analyze.¹⁵⁵⁻¹⁶¹ Exact scattering functions have been calculated and widely accepted for simple bodies such as spheres, cylinders, ellipsoids, etc¹⁶¹. Colloidal systems are more complicated to analyze because the particles may vary in both shape and size. However, SAXS can provide both structural and kinetic information on the nano-sized inhomogeneities in the medium of interest, such as inhomogeneity/particle shape, size, number density and polydispersity (standard deviation in particle size), in addition to aggregate size, interparticle interactions, mass fractal dimension, and degree of branching¹⁵⁹⁻¹⁶¹.

3.7 Differential Scanning Calorimetry (DSC)

Differential Scanning Calorimetry is a type of thermal analysis used to study the effects of temperature in polymers when heated. Figure 3.6 illustrates the basic set-up for a DSC. The DSC uses thermocouples to monitor the temperature of an empty, reference sample pan and a polymer sample pan. The two samples are mounted on their own heating blocks. These samples are continually measured to ensure that the temperature of both samples remains constant. Thus, when there is a temperature differential between the sample pans, the different amounts of energy required to maintain this equilibrium provides insight to the thermal events that are occurring.^{122, 123}

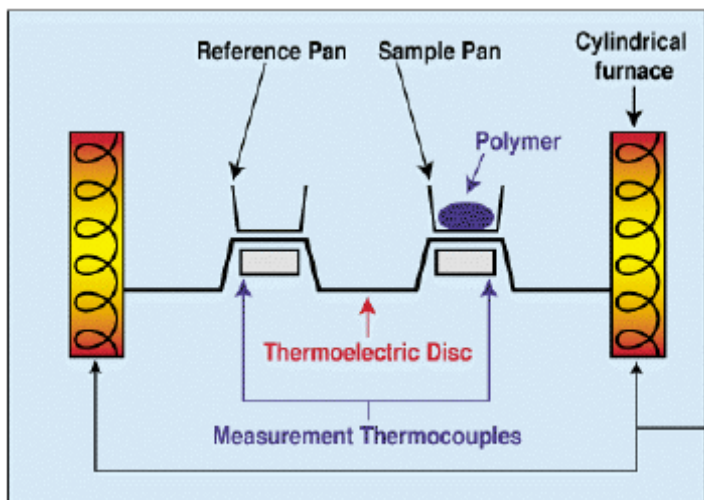


Figure 3.6: Illustration of DSC set-up

The difference between the sample pans is directly related to the specific heat of the sample. Specific heat is the measure of how much energy (heat) per unit of mass is required to raise the temperature of the sample 1°C. Thus, specific heat varies between

the different polymer characteristics, and a plot can be made of the changes in the specific heat of the polymer sample pan in relation to the reference sample pan.^{122, 123}

The typical characteristics that can be analyzed using the DSC are the glass transition temperature (T_g), melting temperature (T_m), and crystallization temperature (T_c). A typical DSC scan, which illustrates all three characteristics, can be seen in Figure 3.7.

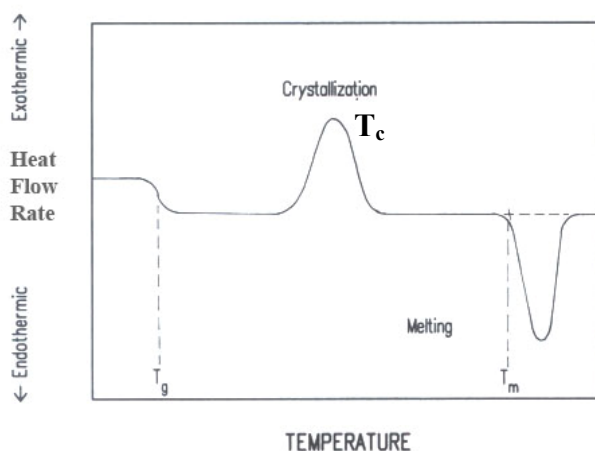


Figure 3.7: Sample DSC scan¹²³

The glass transition temperature represents the change from glassy (rigid, hard) behavior to rubbery (soft, flexible) behavior. This change in behavior is based on an increase in molecular motion within the polymer chains. These motions can be thought of to be like Brownian motion for polymer chains; translation motion of entire molecules, cooperative wiggling and jumping of chain segments (40-50 carbon atoms in length), motion of side groups or a few main chain atoms, and vibrations of atoms within their equilibrium positions.^{122, 123}

The melting temperature of polymers requires significantly more energy to stay at a constant temperature. This is because as a polymer melts, the chain motion increases so

that the chains are able to slip past each other. Thus, this is an endothermic reaction. The crystallization of polymers requires very little energy to stay at the temperature of the reference pan, and in many cases heats up more quickly. This is because crystallization is an exothermic reaction. The chains in the polymer organize themselves creating a less randomized structure. This is the result of long-range ordering of polymer chains as the polymer cools.^{122, 123}

In order to accurately measure the polymer properties, the samples must meet the sample weight requirements for the individual DSC. Typical sample weights range from 5-20 mgs and heating rates range from 10-40°C/min. The heating rate does play a role in the values obtained for the T_g , T_m , and T_c of polymer materials. Generally, there is a range of results. For instance, as a material is heated slowly, the polymer chains have a chance to equilibrate, and the property in question will occur at a lower temperature. If the heating rate is fast, the polymer chains don't equilibrate as quickly and the property in question will occur at a higher temperature.^{122, 123}

CHAPTER 4

EFFECTS OF DIFFERENT DISPERSING AGENTS ON POLYMER CARBON NANOTUBE COMPOSITES

4.1 Overview

In this chapter, we probed the effects of three different dispersing agents on the ability to disperse carbon nanotubes and their effects on the mechanical properties of the composite systems. Section 4.2 gives a brief introduction and background surrounding the motivation and previous research which leads to the need of this type of research study. Section 4.3 details the experimental procedure used to disperse the carbon nanotubes and make the composite samples. Section 4.4 describes the results of the dispersion and alignment of carbon nanotubes in viscous polymer flow. Section 4.5 describes the results of the alignment of carbon nanotubes in an epoxy matrix. In conclusion, Section 4.6 summarizes the dispersion and alignment results of the two systems. The next chapter expands upon this research by attempting to align the carbon nanotubes utilizing a different dispersion system.

4.2 Introduction

This dispersion of the carbon nanotubes through the use of surface-active agents that reduce the van der Waals forces of the CNTs, allows for a better expression of their

enhancement capabilities of the mechanical properties of the polymer matrix material in which they are embedded. Therefore, the optimization of the most efficient dispersing agent becomes a pivotal, albeit challenging, step in the design of CNT-polymer composite materials. The dispersing agent not only needs to tether itself to the carbon nanotubes, but also to create an interfacial layer between the matrix and the filler (i.e. the dispersed CNTs).¹⁶² Therefore, the optimal dispersing agent has to exhibit favorable interactions both with the matrix and with the CNTs. These criteria constitute a fundamental requirement in the design of polymer-CNT composite materials in which the mechanical properties are noticeable enhanced as compared to those of the matrix material alone.

In this present work, three different surface-active agents were used to create carbon nanotube/polymer matrix composites and to determine their effects on the mechanical properties of the composite. The dispersing agents were sodium dodecyl benzene sulfonate, NaDDBS, an anionic surfactant, a polystyrene-based commercial block copolymer (BCP) and a Pluronic, i.e. a PEO-PPO-PEO block copolymer. The dispersed CNTs were then embedded in an epoxy matrix and the resulting composite was subjected to a variety of mechanical tests in order to determine its glass transition temperature and its various moduli (elastic, viscous, etc.) as compared to the pure epoxy matrix. Since all composite samples were identical with the exception of the dispersing agent used, the differences in these properties would indicate the degree and effect of the CNT dispersion.

4.3. Experimental Procedure

The composites were made with EPON Resin 826, a transparent, highly viscous resin. The manufacturer's specification (Miller-Stephenson Chemical Co., Inc.) states that the resin is a material containing bisphenol-A-(epichlorhydrin) with a number average molecular weight ≤ 700 . The hardener used was diethanolamine (Fisher Scientific, $C_4H_{11}NO_2$, FW 105.14 g/mol), a colorless viscous liquid.

Three different 10 ml base solutions were prepared. Solution 1 contained 1.2 mM NaDDBS with 5.0 mg carbon nanotubes. Solution 2 consisted of ethanol (100%) and 5.0 mg BCP with 5.0 mg carbon nanotubes. Solution 3 consisted of 2 wt% PEO-PPO and 6.0 mg carbon nanotubes. Solution 1 was then placed in a vibracell sonicator (Sonics and Materials, Inc., 20 kHz) at 14 % amplification for 30 minutes. Solution 2 was placed in an ultrasonic bath at room temperature for 5 minutes. Solution 3 was placed in a sonic dismembrator (Fisher Scientific, 20 kHz) for 30 minutes. After sonication, TEM samples of all solutions were prepared to determine extent of SWNT dispersion: a droplet of solution was placed onto a TEM grid (Ted Pella, Inc. carbon coated copper, PELCO® Center-Marked Grids, 400 mesh, 3.0 mm O.D.) and allowed to dry for later analysis in a Hitachi HF-2000 field emission gun, 200 kV transmission electron microscope (TEM).

In order to determine the effects of the dispersing agents on the composite samples, 14 different samples were made varying carbon nanotube concentration and block copolymer (BCP and Pluronic) concentration. It is evident in the paper by Matarredona et al.⁵ that increasing the concentration of NaDDBS would only lead to micellization and were untested in this study. However, in this study the solutions varied in CNT content from 5-15 mg^{4,5} (BCP and NaDDBS) or 6-12 mg⁶ (Pluronic), the BCP

varied from 5-20 mg, and the Pluronic varied from 2-6 wt%. The BCP solutions were made into composite samples following the methods described by Li et al.⁴ The Pluronic solutions were made as described by O'Connell et al.⁶, however the centrifugation step was excluded to keep results consistent between all three dispersing agents. The Pluronic and NaDDBS composites were then made using a modified procedure, where water and not ethanol was used, based on the method by Li et al.⁴ Composite samples were made using a pre-formed metal dog bone molds. The dog bone sample dimensions were 11.5 cm, 2cm, and 0.6 cm for length, width, and gage length, respectively.

The samples were tested using dynamic mechanical analysis (DMA, TA Instruments Q800) to determine the effects of dispersing agents on the composite samples. The samples were tested at 10-200 °C at 3 °C/min to obtain information across the glass transition temperature. The data collected was then analyzed and graphed to determine elastic modulus, glass transition temperature, and trends within the data which can be seen in Table 4.1.

Table 4.1: Summary of the measured and calculated mechanical properties, such as glass transition temperature, elastic modulus, storage modulus, and loss modulus for the various samples characterized in this work.

Dispersing Agent	Concentration (vol %)	CNT (vol %)	Glass Transition		$\tan\delta$	Storage Modulus (MPa)	Loss Modulus (MPa)
			DSC (°C)	DMA (°C)			
none		0.0	65.5	69.5	0.733	2951	152
BCP	0.495	0.263	63.1	64.1	1.026	2076	272
BCP	0.495	0.0	52.4	61.7	1.174	865	92
BCP	0.495	0.526	59.2	69.1	0.909	2239	313
BCP	0.495	0.789	52.7	62.8	0.946	2311	143
BCP	1.485	0.263	63.0	71.5	0.645	2250	194
BCP	1.980	0.263	62.4	77.9	0.717	3404	192
NaDDBS	0.409	0.263	43.5	80.6	0.742	2457	185
NaDDBS	0.409	0.526	45.8	74.4	0.656	2869	204
NaDDBS	0.409	0.789	45.7	79.5	0.690	2660	117
Pluronic	0.189	0.316	56.7	55.8	0.554	1274	89
Pluronic	0.189	0.632	64.7	58.5	0.557	1746	253
Pluronic	0.189	0.947	57.0	58.4	0.599	3089	367
Pluronic	0.377	0.316	56.4	58.4	0.599	2555	314
Pluronic	0.566	0.316	56.8	61.1	0.632	2100	168
NaDDBS	0.409	0.0	40.9	n/a	n/a	n/a	n/a
Pluronic	0.189	0.0	83.8	n/a	n/a	n/a	n/a
NaDDBS	0.000	0.0	46.4	n/a	n/a	n/a	n/a
Pluronic	0.000	0.0	-63.6	n/a	n/a	n/a	n/a

Dynamic Scanning Calorimetry (DSC, TA Instruments Q100) tests were run on the samples to determine the glass transition temperatures of the samples. The samples were tested using a cyclical heating cycle the data was collected on the second heat which was run from 0.0- 200°C at 10°C/min. The data was collected then analyzed using TA Universal Analysis program.

The samples in this research were tested with a Rigaku MicroMax-002 Microfocus X-ray Generator equipped with a R-axis IV++ WAXS/SAXS detector (45kV, 0.66mA). The samples were tested from 0.0 -7.0 ° with a 0.02 step size. The small angle X-ray scattering (SAXS) data was collected in order to analyze structurally analyze the samples through statistical methods. SAXS was chosen because of the potential of using the results in conjunction with additional analysis, i.e. the calculation of structure using a two-point probability function protocol. The data collected was analyzed to determine if material properties could be determined from the SAXS data¹⁵⁵⁻¹⁵⁸.

4.4. Results and Discussion

4.4.1. Dispersion Mechanisms

The high degree of aggregation of SWNT is due to the high cohesive energy of the tubes, which has been estimated to be on the order of 36 kT for each nanometer of length overlap between adjacent tubes⁶¹. The addition of NaDDBS to the suspension results in the exfoliation and dispersion of the carbon nanotubes, as shown in Figure 4.1.

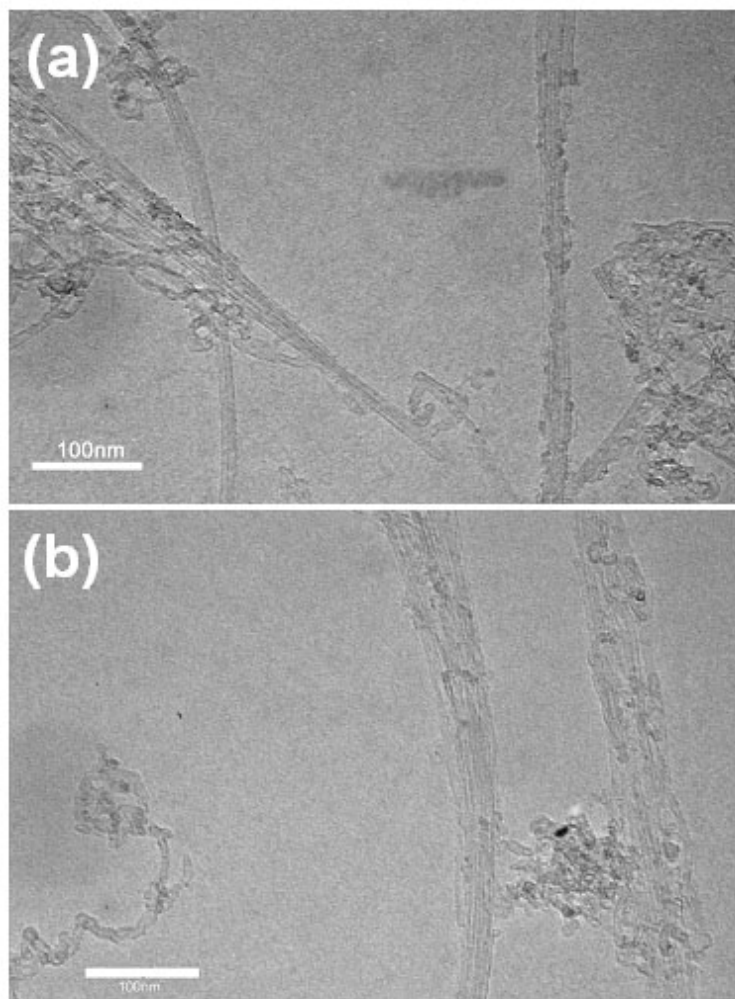
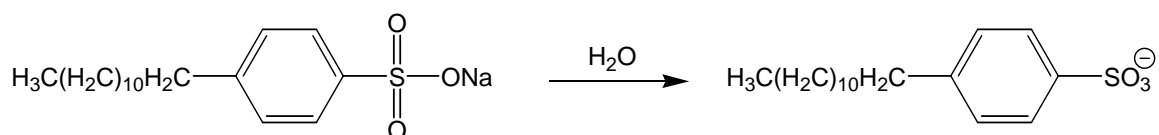


Figure 4.1: Transmission electron microscopy micrographs of SWNT dispersed with 0.409 vol% NaDDBS at varying carbon nanotubes concentrations to illustrate variations in bundle size (a) 0.263 vol% CNT, bundle size 15-20nm (b) 0.789 vol% CNT, bundle size 15-60nm.

NaDDBS dissociates in an aqueous environment to generate a sulfonium group, as shown below:



The hydrocarbon moiety interacts with the surface of the carbon nanotube, while the surrounding water molecules solubilize the anionic group. This increases the solubility

of the carbon nanotubes and allows their exfoliation and dispersion in the aqueous medium. Conversely, since the experimental procedure involves the sonication of the SWNT suspensions, it is also quite likely that this generates considerable exfoliation of the nanotubes, followed by the adsorption of the surfactant molecules, which in turn, stabilizes the nanotubes due to steric repulsion.^{69, 72, 73, 84}

Figure 4.1(a,b) illustrates the effect of increasing CNT content on the ability of NaDDBS to adequately disperse the CNTs. Figure 4.1a illustrates a SWNT bundle diameter range of 15-25 nm, confirming the fact that NaDDBS is capable to disperse the CNTs into small bundles⁵. However, when the concentration of the CNT in solution doubles, the bundle size range increases to 15-60 nm, as shown in Figure 4.1b. Thus, in order to stabilize a narrow distribution of small bundle sizes, larger concentrations of NaDDBS would be required, commensurate with the increase of the concentration of CNTs. Unfortunately, such an increase may prove difficult, because once the concentration of NaDDBS in solution rises above its critical micelle concentration, it will no longer be able to provide the appropriate dispersion capability.

The polystyrene based BCP and the Pluronic dispersants both have lyophobic blocks and lyophilic blocks that act as interfacial binding agents between the solution (ethanol) and the carbon nanotubes,⁴ a mechanism that is illustrated schematically in Figure 4.2.

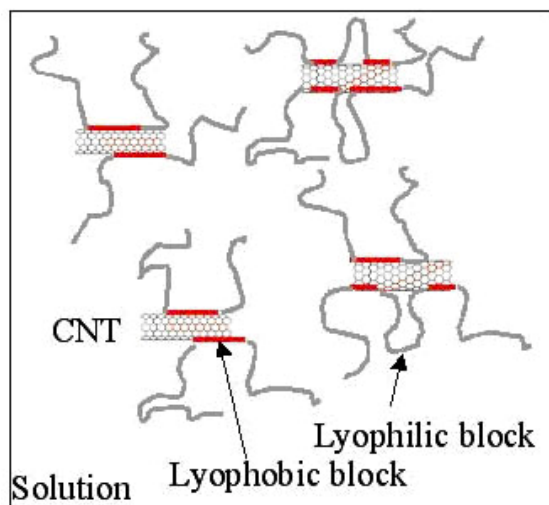


Figure 4.2: Schematic illustration of how copolymers utilize lyophilic and lyophobic blocks as the mechanism for the dispersion of SWNTs in solution. The respective blocks associated with the solution and the carbon nanotubes allowing for the exfoliation and dispersion of the carbon nanotubes.

These lyophilic and lyophobic blocks increase the solubility of the carbon nanotubes, which in conjunction with the mechanical separation created by the ultrasonic bath, results in a dispersed suspension of carbon nanotubes.

The addition of the block copolymer Disperbyk 2150 to the CNT suspension leads to the exfoliation and dispersion the carbon nanotubes as well. The high molecular weight of the BCP reduced the quality of the TEM images obtained for this system, but nevertheless, the approximate bundle size of the nanotubes could still be determined, as shown in Figure 4.3 (a,b). The BCP-CNT solution appears to be well dispersed after sonication, but further examination shows that there are actually large bundles of CNTs with an average diameter of approximately 75 nm, as illustrated in Figure 4.3a. Upon increasing BCP concentration, the bundle size increases to 90 nm, as shown in Figure 4.3b. This is most likely due to the ability of the long chains of the BCP to adsorb on

more than one CNT, thus inducing a higher degree of proximity between small bundles and generating an opposite effect to good dispersion. This leads to the conclusion that the BCP is not an effective dispersing agent for the CNT, as it clearly stabilizes only significantly larger bundles than those obtained with the NaDDBS system.

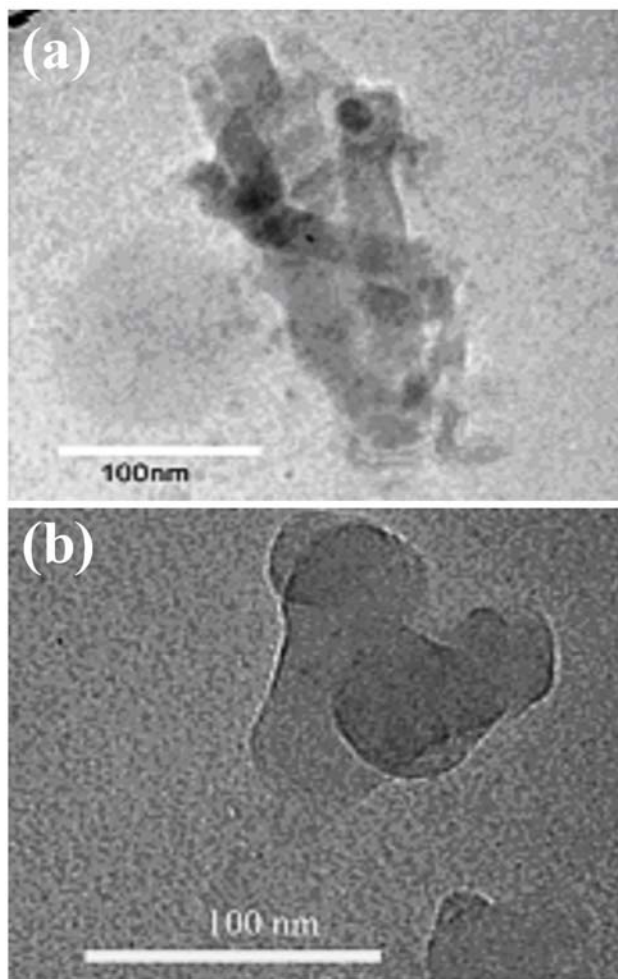


Figure 4.3: Transmission electron microscopy micrographs of SWNT dispersed with BCP at increasing BCP concentrations to illustrate the variation in bundle size as BCP concentration increases (a) 0.495 vol% BCP, 0.263 vol% CNTs, bundle size 75 nm (b) 1.980 vol% BCP, 0.263 vol% CNTs, bundle size 90 nm

The addition of the Pluronic F108, a PEO-PPO block copolymer works in the same manner as the commercial BCP. It helps suspend, exfoliate, and disperse the carbon tubes by increasing the distance between the CNT chains, as shown schematically

in Figure 4.2. The lyophilic block interacts with the solvent molecules, in this case water, and the lyophobic block interacts with the carbon nanotubes, thus separating the carbon nanotubes and reducing the van der Waals forces between them. The Pluronic is added during the sonication or mechanical dispersion step of the carbon nanotubes, which promotes its immediate intercalation and interactions with the nanotubes. It was shown that while Pluronic molecules allow the dispersion of carbon nanotubes, the carbonaceous particles and catalyst particles precipitate out.⁸⁴

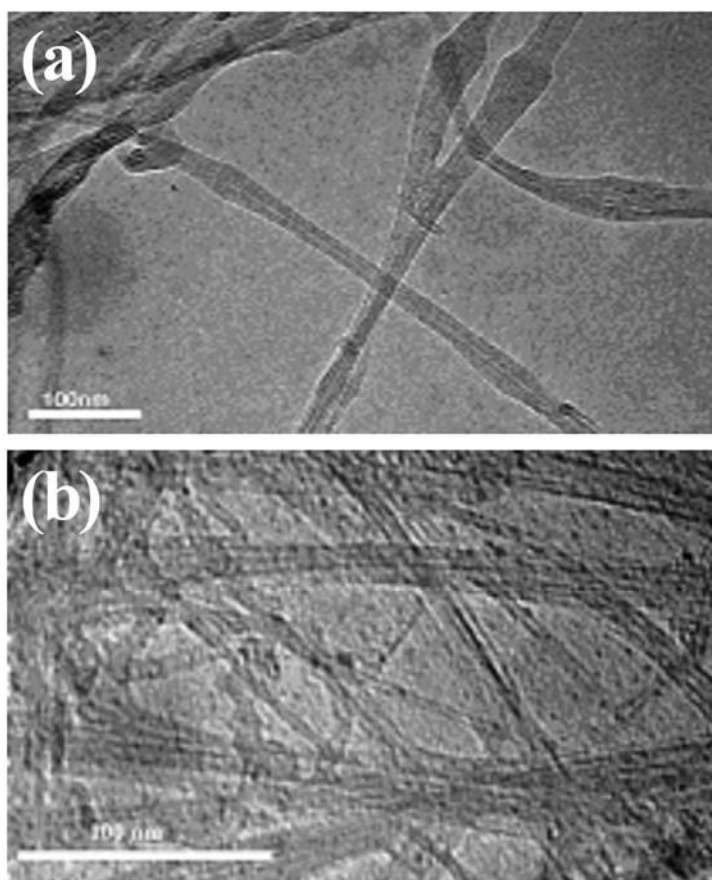


Figure 4.4: Transmission electron microscopy micrographs of SWNT dispersed with Pluronic F108 at increasing concentration to illustrate the variation in bundle size as the Pluronic concentration increases (a) 0.189 vol% Pluronic bundle size 15-25 nm, 0.263 vol% CNTs (b) 0.566 vol% Pluronic, 0.263 vol% CNTs, bundle size 15-40 nm.

Figure 4.4 (a,b) illustrates the effect of the Pluronic concentration on the CNT bundle size. Similarly to the NaDDBS system, the Pluronic gives rise to a small and narrow range of CNT bundles of sizes 10 – 25 nm, as shown in Figure 4.4a. At a higher concentration of Pluronic, the range of the bundle sizes exhibited only a limited increase to 10 – 40 nm. Since the Pluronic chains are relatively short (since the Pluronic has a relatively low molecular weight), the "corralling" effect observed with the BCP system is rather limited. Therefore, the Pluronic proves to be a useful method for dispersing the carbon nanotubes into small bundles, as it is also insensitive to the CNT/Pluronic ratio.

4.4.2 Effect of Glass Transition Temperature

The glass transition temperature of any polymer depends on four factors: free volume and chain stiffness, intramolecular and intermolecular interactions of chains, internal mobility of chains, and the degree of polymer cross-linking.¹²³ Ideally, the addition of the CNTs and the dispersing agent to an epoxy matrix would cause little to no change in the glass transition temperature, as long as the carbon nanotubes concentration is below the percolation threshold. However, given the complexity of the composites in this study, the determination of the variations in the glass transition (if any), could shed some light on the organization of the CNTs and the various dispersing molecules in the system and provide useful design tools for potential applications.

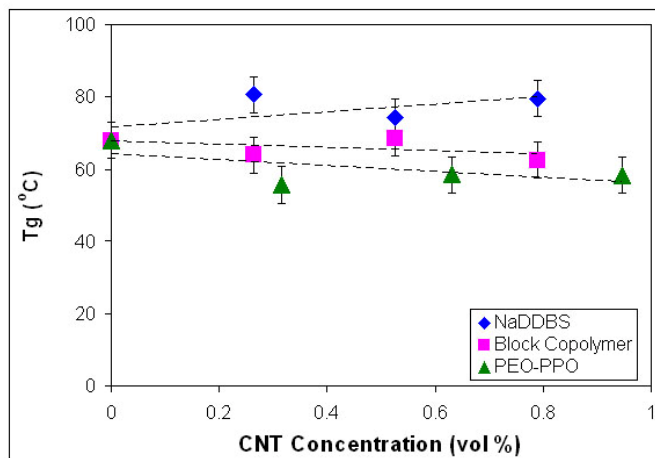


Figure 4.5: This graph illustrates the effect of the dispersed carbon nanotubes at various concentrations on the epoxy glass transition temperature. The glass transition temperature is affected differently and is correlated to the dispersing agent and its properties.

As illustrated in Figure 4.5, the addition of the carbon nanotubes does indeed appear to have a limited effect on the glass transition temperature of the epoxy matrix, depending upon the dispersing agent used¹⁶³. This could be attributed to several different factors: the carbon nanotubes could act as heterogeneous crystallization sites for the polymer, poor interactions between dispersant and matrix, and poor interaction between dispersant and CNTs.

For both BCP and Pluronic dispersing systems, the increase in the concentration of CNTs at constant co-polymer concentration depressed the glass transition temperature. As the CNT concentration approached its percolation threshold ($< 1 \text{ wt}\%$)^{164, 165}, the number of bundles increased and the effect of the unfavorable interactions between adjacent adsorbed co-polymer chains became more dominant. This caused an increase of the volume associated with each bundle and an overall increase in entropic energy, thus lowering the glass transition temperature of the composite.¹⁶⁶ In the case of the addition

of the NaDDBS surfactant, the small increase in the glass transition temperature of the composite is due to the effective dispersion of the carbon nanotubes coupled with only a small associated volumetric change given the small size of the dispersing molecule, resulting in an increase in local carbon nanotube and epoxy network organization, i.e. formation of crystalline regions within the epoxy matrix.¹⁶⁷⁻¹⁷⁰

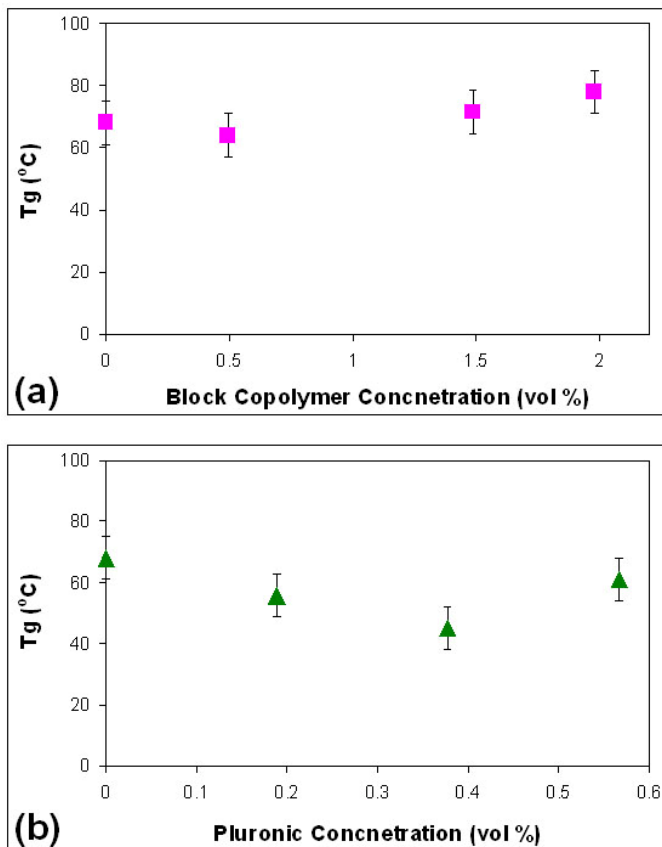


Figure 4.6: These graphs illustrate the effect on the epoxy glass transition temperature as a function of the (a) Pluronic and (b) BCP at varying concentrations. This illustrates a contradicting effect of the copolymers on the glass transition temperature, which corresponds to the different in molecular weight and interactions of the copolymers in the epoxy matrix.

Conversely, increasing the concentration of the BCP and Pluronic dispersing agents at constant CNT concentration appeared to have a more significant effect on the glass transition temperature. The drop in T_g caused by the addition of the Pluronic and

shown in Figure 4.6a, could be the result of a plasticizing effect that this low molecular block co-polymer exerted on the system. Alternately, it is possible that the PPO-PEO-PPO blocks did not interact with the epoxy matrix resulting in a limited degree of phase separation (at the nanoscopic level), thus reducing the T_g .¹⁷¹⁻¹⁷⁴ While DSC data indicated that phase separation was not occurring on a macroscopic level (because the data showed that there was only one glass transition temperature for the Pluronic-epoxy system), this does not preclude the presence of a limited phase separation on a local, nanoscopic level.

The limited increase in the T_g of the composite in the presence of BCP-dispersed carbon nanotubes, as seen in Figure 4.6b, may be attributed to the contribution of the high molecular weight of the dispersant and its more favorable interactions with the epoxy matrix through the presence of the styrene block.¹⁷⁵⁻¹⁷⁷ As the amount of BCP increases, the contribution of bridging adsorption of chains increases as well, generating a higher degree of effective CNT-mediated cross-linking and matrix connectivity, thus increasing the glass transition temperature of the composite.

4.4.3 Effect on Storage, Loss Modulus and Tan Delta

The loss modulus of a viscoelastic material is the measurement of the energy dampening effect (or energy lost, usually as heat) during the deformation of the sample, whereas the storage modulus is a measurement of the energy stored within the sample during deformation.¹³⁴ The addition of carbon nanotubes and dispersing agent to the matrix material would ideally lead to create a product that has a significantly higher storage modulus, which would correspond to an increase in loss modulus as well.

However, to increase the overall strength of the material the storage modulus increase should be higher than that of the loss modulus. The addition of the carbon nanotubes should help to distribute and store the energy during deformation. This would then be reflected in a decrease in $\tan \delta$.¹⁷⁸⁻¹⁸³

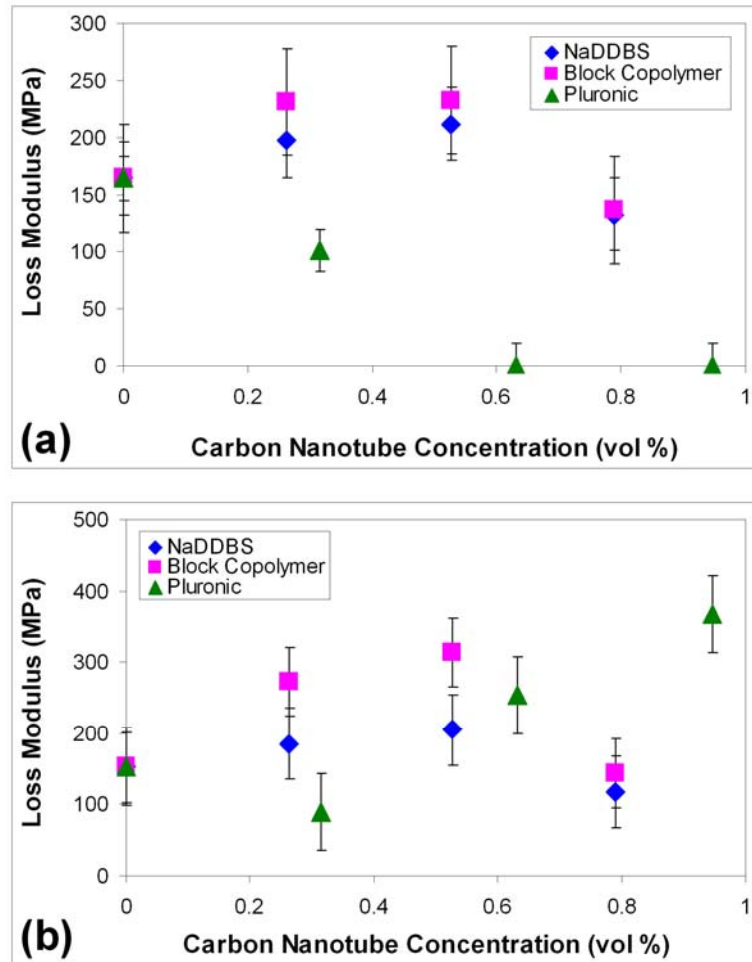


Figure 4.7: Experimental Dynamic Mechanical analysis data illustrating the average loss modulus for the three different dispersing agents at varying carbon nanotube concentration at two temperatures (a) 30°C (b) 10°C. This data illustrates that there is a very different effect on the loss modulus between the NaDDBS and BCP versus the Pluronic at 30 C. At 10 C, there appears to be almost no change in the NaDDBS and BCP systems, but a profound increase in Loss modulus in the Pluronic system.

In Figure 4.7 (a,b), the average loss modulus for the three different samples at varying carbon nanotube concentration is reported for an experiment whose onset was at

30 °C (Figure 4.7a). It can be seen that with increasing carbon nanotube concentration there is a decrease in the loss modulus for the Pluronic samples, whereas in the NaDDBS and the commercial BCP systems the loss modulus exhibits a parabolic behavior with respect to the CNT concentration. The magnitude of the loss modulus in these systems is increased at CNT concentrations below ~0.4 vol.%, but at higher CNT concentrations it was actually lower than that of the epoxy matrix without CNTs.

When the same dynamic experiment was conducted starting from 10 °C (and not from 30°C), the behavior of the NaDDBS and BCP systems at 10 °C remains similar to the one at 30 °C (Figure 7b). This non-linear change in loss modulus with increasing CNT content could be related to two effects; (1) The ballistic thermal transport found in CNTs as stress is placed on the sample, the epoxy chains reconfigured themselves to relieve the strain. With the increase in CNT content, the energy dissipated as heat in the chains is transported efficiently through the carbon nanotubes, especially at concentration near the percolation threshold, and the large content of nanotubes in the sample reduced the amount of reconfiguration the chains would be required to undergo under stress; or (2) As the CNT in the sample increases, the number of bundles increases, the efficiency of their interactions with the matrix decreases (due to larger volumes associated with each bundle) and the efficiency of the thermal transport decreases. This decrease in loss modulus is accompanied by a moderate increase in storage modulus, which might indicate that the increase in carbon nanotube concentration may be actually hindering the strength of the sample. In the case of the NaDDBS systems, the increase in CNT content promotes the formation of crystalline domains, which, while they increase the system glass transition, they also lower the ability of the system to dissipate heat.^{167-170, 173}

The loss modulus in the Pluronic system measured starting at 10 °C, initially decreased, but at CNT concentrations above ~0.3 vol.% it steadily increased with carbon nanotube content to reach values that were considerably higher than that of the epoxy matrix without CNTs. The difference between the measurements at 10 °C and at 30 °C in the Pluronic system is due mainly to the “softening” of the composite at the higher temperature, as was also evidenced by the decrease in the T_g of the material. If the loss modulus is measured at lower initial temperatures, well below the T_g of the composite, changes in the loss modulus reflect only the contribution from the well-dispersed CNTs. Under these circumstances, at concentrations above ~0.3 vol.%, the carbon nanotubes were organized in a stable network that could provide an efficient energy dissipation mechanism.

The storage moduli for all the dispersing systems examined in this work measured at 30 °C were lower than that of the pure epoxy. The reasons for this lack of mechanical strength could be due to the fact that the carbon nanotubes were dispersed only in bundles, and in most cases, also exhibited poor interactions between the dispersing agents and the epoxy, resulting in poor interfacial properties.¹⁷⁴⁻¹⁷⁷

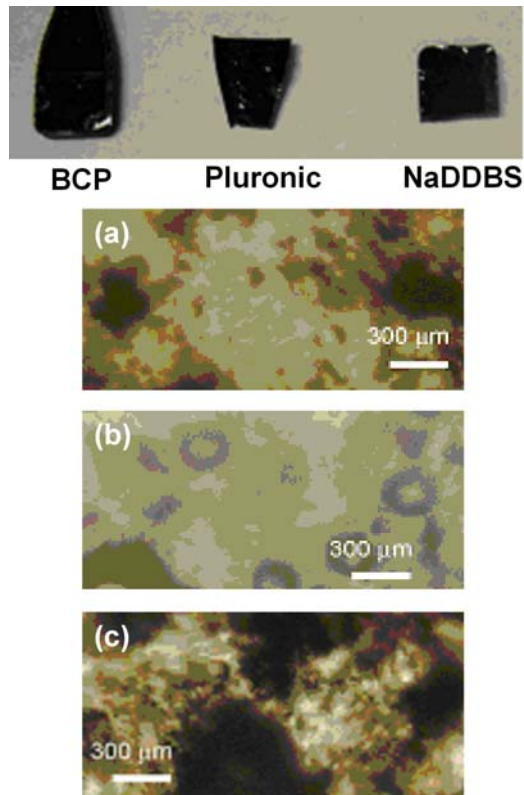


Figure 4.8: Pictures of the three bulk composite samples and corresponding light microscope images at 10x magnification of the three different dispersing agents at the same carbon nanotube concentration (a) 0.495 vol %BCP; 0.263 vol% CNTs, (b) 0.409 vol% NaDDBS ; 0.263 vol% CNTs(c) 0.189 vol% Pluronic; 0.263 vol% CNTs

Figure 4.8, which illustrates the bulk composite samples, shows that initially the samples appear to be uniform. However, pictures of the bulk samples under light microscopy at 10x magnification show that the BCP sample appears to have a significant amount of phase separation, which is also seen in the NaDDBS sample. The NaDDBS sample has an increased amount of porosity, which is not observed in the other two samples. While some aggregation seems to occur in all the samples, the Pluronic samples appear to be more uniform: The sample is significantly more opaque and an image could only be obtained on a fracture surface.

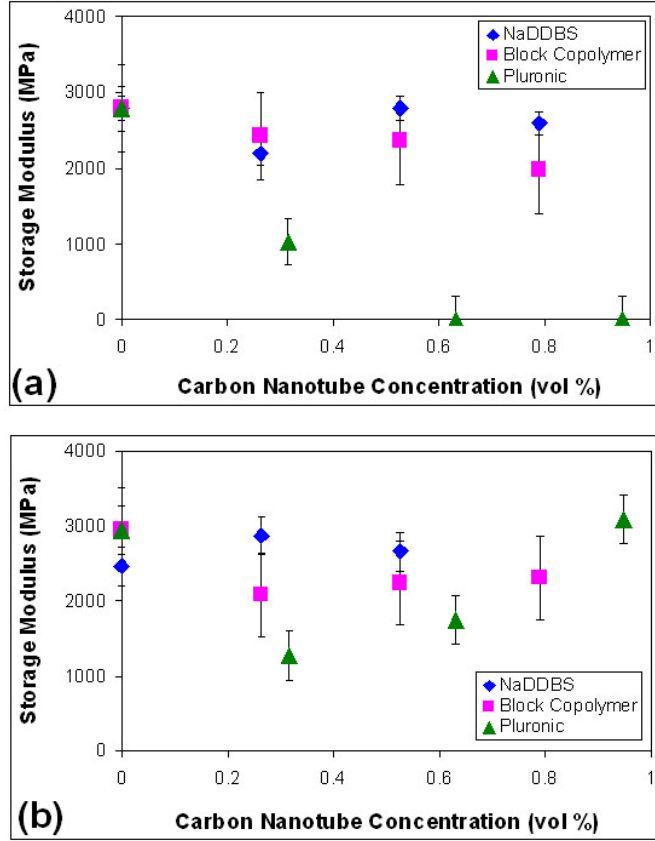


Figure 4.9: Experimental Dynamic Mechanical analysis data illustrating the average Storage modulus for the three different dispersing agents at varying carbon nanotube concentration at two temperatures (a) 30°C (b) 10°C. The storage moduli of the NaDDBS and BCP appear to decrease slightly at lower temperatures with higher concentrations of CNTs. Conversely, the storage modulus of the Pluronic system increases considerably with the increase in CNT concentration beyond ~0.3 vol.%.

Figure 4.9 (a,b) highlights the difference in the behavior of the storage moduli for the three different dispersion systems when the temperature at the onset of the measurement is lowered from 30 °C (Figure 4.9a) to 10 °C (Figure 4.9b). The storage moduli of the NaDDBS and BCP appear to decrease slightly at lower temperatures with higher concentrations of CNTs. Conversely, the storage modulus of the Pluronic system increases considerably with the increase in CNT concentration beyond ~0.3 vol.%.^{164, 171}

This is similar to the behavior of the loss modulus at the low onset temperature.

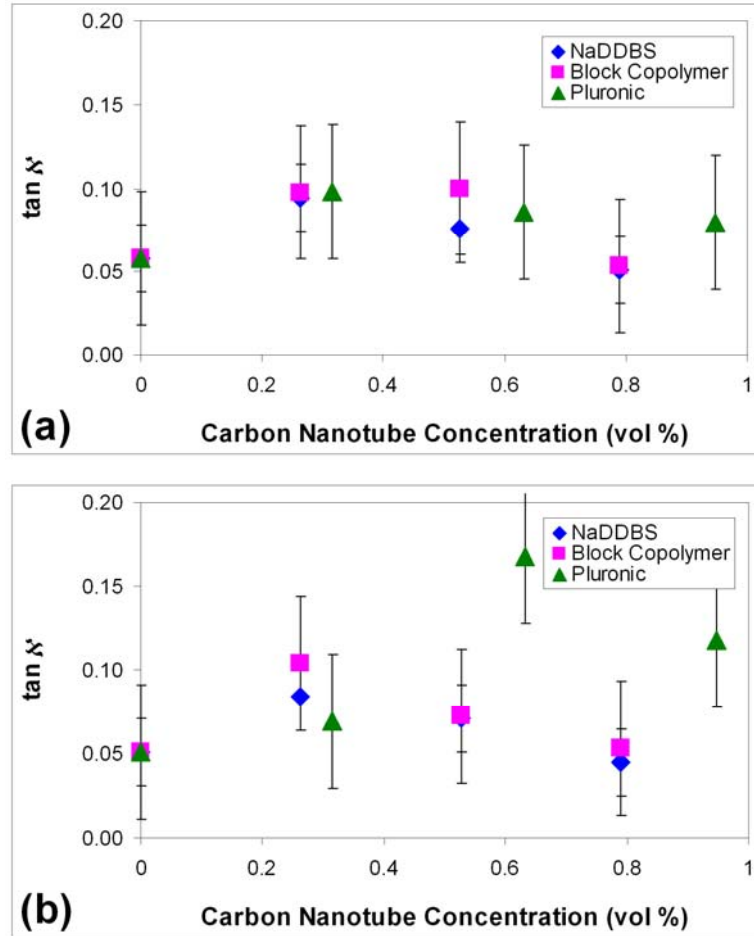


Figure 4.10: Experimental Dynamic Mechanical analysis data illustrating the average $\tan \delta$ for the three different dispersing agents at varying carbon nanotube concentration at two temperatures (a) 30°C (b) 10°C. The data had large fluctuations that were particularly pronounced in the experiments conducted at 10°C. This is due to the opposing behavior in the loss and storage moduli of the Pluronic system at 30 °C and at 10 °C.

The $\tan \delta$ of all the samples, irrespective of the dispersing agent, exhibited relatively constant values at all concentrations of CNTs that were examined, as shown in Figure 10 (a,b). The data had large fluctuations that were particularly pronounced in the experiments conducted at 10 °C (Figure 10b). This is due to the opposing behavior in the loss and storage moduli of the Pluronic system at 30 °C and at 10 °C.

4.4.4 Small Angle X-Ray Scattering (SAXS) of SWNT-Epoxy Composites

The SAXS results were used to analyze the distribution of CNT in the composite using two-point probability distribution functions.^{184, 185} This type of analysis can lead to an understanding of the CNT dispersion in the matrix, which can, in turn, be correlated to the potential mechanical properties (stiffness, toughness, etc) of the composites. However, the SAXS did not produce any peaks from the CNTs, most likely due to the low volume fractions used in this study. So the data was not useful at this junction to allow for the two-point distribution analysis.

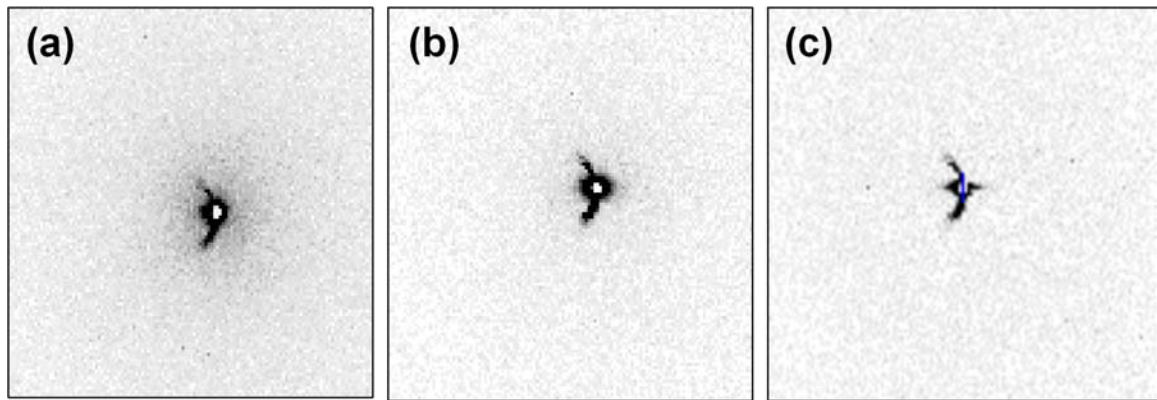


Figure 4.11: Experimental SAXS data of an illustrating three different types of orientation of a lamellar structure in the composite samples (a) isotropic (b) slight anisotropy (d) complete anisotropy. The lamellar structure can be inferred by the dark circular/elliptical region surrounding the center, where the flare is due to the X-Ray machine. The presence of lamellar structures in the pure epoxy matrix is indicative of the existence of crystalline regions. The changes in the presences of and orientation of the crystalline region in the composite samples are likely from intermolecular interactions of the epoxy with the carbon nanotubes, dispersing agents, and also the combined intermolecular interactions between the carbon nanotubes and dispersing agent.

However, SAXS measurements revealed the presence of a lamellar structure in some of the samples, as shown in Figure 4.11 (a-c). The circular to elliptical halo (left to right) is the result of the lamellar structure, and the flare seen in all three figures is due to the beam. The pure epoxy samples exhibited a completely isotropic lamellar structure, as

shown in Figure 4.11a. The commercial BCP showed a completely isotropic lamellar structure at high concentrations of CNTs, a slight preferred orientation of the lamellar structure at high concentrations of BCP, as shown in Figure 4.11b, and a complete anisotropic lamellar structure at low concentrations of both CNTs and BCP, as shown in Figure 4.11c. The NaDDBS system exhibited the presence of an isotropic lamellar structure, while in the Pluronic system no such structures were detectable. The presence of lamellar structures in the pure epoxy matrix is indicative of the existence of crystalline regions. The fact that in some cases these regions are either increased and/or oriented is most likely a function of the interplay between the amount of CNTs in the system, the amount of dispersing agent available to the CNTs moiety, and the nature of the intermolecular interactions between the dispersing agent and the CNTs and the epoxy matrix. The possible presence of crystalline regions in both the NaDDBS and the BCP systems has been postulated based on the changes in the glass transition of the composites and their mechanical properties^{186, 187}. The dependence of the glass transition temperature on the ratio between the CNT and dispersant in each system, shown in Figure 4.12, demonstrates two behavior regimes for the NaDDBS and the BCP composites. At low ratios, i.e., $V_{\text{CNT}} < V_{\text{Dispersant}}$, the system is dominated by the behavior of the dispersing molecules and their interactions with the CNTs and the epoxy matrix.

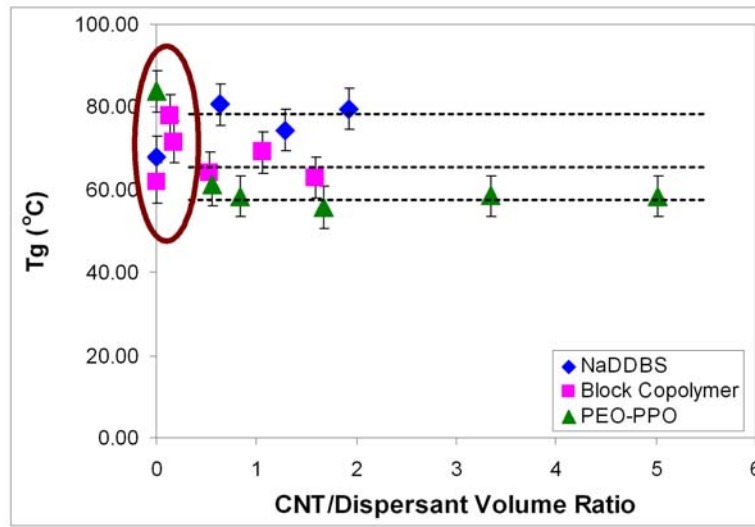


Figure 4.12: Experimental calculation of the ratio between the CNT and dispersing agent for each systems and the correspond effect on the glass transition temperature. This graph illustrates two behavior regimes for the NaDDBS and the BCP composites. At low volume % the behavior is related to the dispersing molecules, but at higher volume % the behavior is dependent upon the CNTs.

Under these circumstances, the NaDDBS provides a good dispersion, but being small molecules, does not impose a significant steric barrier to CNTs proximity, and hence, allows the formation of crystalline regions. The BCP molecules, in this case, can interact with several CNT bundles simultaneously, creating inhomogeneous regions of high CNT concentration within the matrix and promote the formation of crystalline regions. This is evidenced by the increase in the glass transition. At higher ratios, $V_{\text{CNT}} \geq V_{\text{Dispersant}}$, the system is dominated by the behavior of the CNTs, i.e. their degree of dispersion a solubilization in the matrix. In this region, all dispersant behave in a similar manner and the glass transition temperature for each system becomes independent of the CNT/Dispersant ratio.

4.5 Summary of the Dispersant Effects on Composite Properties

In this work we have shown that the addition of an anionic surfactant and a Pluronic to a carbon nanotube aqueous suspension facilitated its dispersion. It was also determined that the BCP used in this study did not produce an adequately disperse sample, but rather stabilized large CNT bundles.

It became very clear that the dispersing agents affect the properties of the systems in different ways, and hence, the creation of a product with enhanced mechanical properties is system dependent (epoxy and dispersing agent). A dispersing agent used with one epoxy may not adequately disperse the carbon nanotubes in another epoxy due to the nature of the interactions between the two moieties that are a function of their intimate chemical make-up.

The composites created in this work exhibited mechanical properties that were inferior to those exhibited by the pure epoxy matrix. The reasons for this decrease in properties may be partly due to poor interactions between the epoxy and the dispersing agent, and the low volume fractions of CNTs and dispersants used. It might be beneficial to increase the amount of the carbon nanotubes and determine the effect of this increase on the various parameters that were examined.

The complexity of the interactions between the epoxy matrix and the dispersing agents is a very challenging issue. Given the complex behavior of each dispersing agent with both the CNTs and the epoxy matrix at different concentration regimes, the efforts for the optimization of the properties should be concentrated on a specific system (epoxy and dispersing agent) that demonstrates enhancement of properties under a narrow array of conditions.

CHAPTER 5

ALIGNMENT OF CARBON NANOTUBES UNDER SHEAR VISCOUS FLOW FOR POLYMER AND EPOXY COMPOSITES SYSTEMS

5.1 Overview

In this chapter, we probed the effects of shear flow on the alignment of dispersed single-walled carbon nanotubes in polymer solutions. Section 5.2 gives a brief introduction to polymers and carbon nanotubes. Section 5.3 details the experimental procedure used to align the carbon nanotubes. Section 5.4 describes the results of the dispersion and alignment of carbon nanotubes in viscous polymer flow. Section 5.5 describes the results of the alignment of carbon nanotubes in an epoxy matrix. In conclusion, Section 5.6 summarizes the dispersion and alignment results of the two systems. The next chapter explores alternative methods to align carbon nanotubes by decoration with iron(III) oxide particles.

5.2 Introduction

In addition to the impact of the degree of carbon nanotube dispersion on composite properties, their degree of alignment in the respective matrix plays a crucial role as well. There are several different methods available to align carbon nanotubes, including slicing,⁹³ chemical vapor deposition,⁹¹ melt processing,¹⁸⁸ mechanical stretching,⁹⁹ electrophoresis,¹⁸⁹ application of magnetic fields,^{97, 127, 190-193} and

electrospinning.¹⁹⁴⁻¹⁹⁶ A problem with most alignment processes arises when combining the carbon nanotubes with the polymer matrix to form the composite materials. Under the experimental conditions, a well-aligned array of carbon nanotubes tends to become isotropic and cluster upon mixing into the composite. Hence, the alignment of the carbon nanotubes prior to mixing into a composite is reversed, and once again, they may disperse into random orientations.²⁷

In this present work, shear flow was used to align the carbon nanotubes in a surfactant/polymer matrix. This alignment method has distinct advantages over electrospinning because it can generate polymer sheets rather than polymer fibers. Hence, it is possible to create a nanocomposite in which the SWNT are organized as 2D layers, rather than as highly confined 1D sequence. Evidently, a smaller shear stress will be required to orient the SWNT in a 2D polymer film than into a polymer fiber generated by electrospinning.¹⁹⁷

The nanotubes were initially dispersed with sodium dodecyl benzene sulfonate, NaDDBS, an anionic surfactant, and placed in a polymer solution that was subjected to a circular shear flow, resulting in a well-dispersed, uncoiled, and aligned carbon nanotube structure within the matrix. The addition of a weakly-binding polymer, such as carboxymethyl cellulose, CMC, serves, in this case, two purposes; constituting the polymer matrix in which the SWNTs will be dispersed and aligned and providing a secondary mechanism for the promotion of carbon nanotube dispersion. Samples of the polymer-carbon nanotube suspensions were collected while under the shear flow, both parallel to the shear flow and perpendicular to it. Both the efficiency of the dispersion

process and the carbon nanotube alignment in the polymer solution were analyzed by means of transmission electron microscopy (TEM).

5.3 Experimental Procedure

5.3.1 Polymer Viscous Flow

Two different solutions were prepared, one solution made with 50 mL of 1.2 mM NaDDBS containing 0.4 mg carbon nanotubes and the second solution consisting of 25mL 1.2mM NaDDBS, containing 0.4 mg carbon nanotubes. Both solutions were then placed in a vibracell sonicator (Sonics and Materials, Inc., 20 kHz) at 14 % amplification for 30 minutes. After sonication, 25 mL of a 1 wt% carboxyl methylcellulose (CMC, $\bar{M}_w = 350,000$ g/mol) solution was added to the NaDDBS/SWNTs solution, and the new combined solution was again placed in the vibracell sonicator at 14% amplification for 30 minutes. After sonication, TEM samples of both solutions were taken to determine extent of SWNT dispersion: a droplet of solution was placed onto a TEM grid and allowed to dry for later analysis in the TEM. The solutions were then re-sonicated at 14 % amplification for 30 minutes. The solutions were then placed in a 27.5 mm diameter (I.D.) stainless-steel cylinder. A Brookfield DV-E viscometer with a stainless-steel rotating spindle having 19.0 mm diameter (O.D.) and 65.0 mm in length, was used for viscosity measurements.

The sample solutions were placed in the 8.5 mm gap between the outer cylinder and the spindle, as shown in Figure 5.1a. In turn, the spindle was allowed to rotate for 1 week at several different angular velocities ranging from 12 to 100 rpm, corresponding to approximately 1 to 10 rad/s. A second set of TEM samples were taken in situ from the

solutions flowing in circular motion in the gap between the outer cylinder and inner cylinder (spindle). The sample grids were affixed to a small diameter wire, and slowly dipped into the solution parallel and perpendicular to the flow, as illustrated in Figure 1b, to determine the position of maximum stress after analysis in the TEM. These samples were then analyzed using the JEOL 100CX II, 100kV transmission electron microscope (TEM).

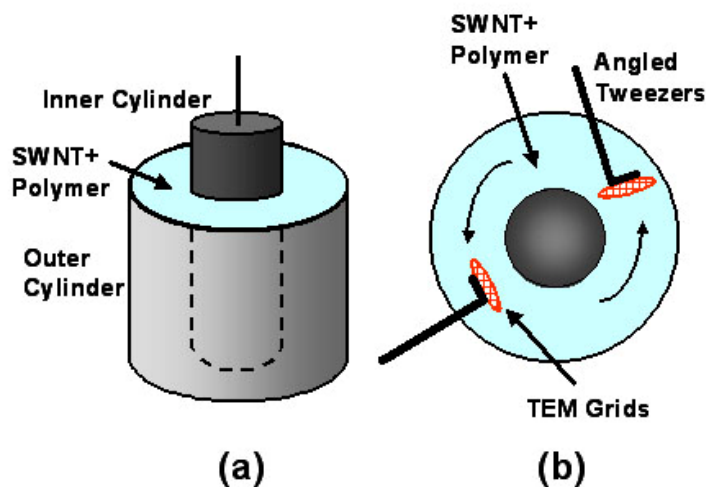


Figure 5.1: Schematic representation of the experimental set-up: (a) Concentric cylinder arrangement in the Brookfield viscometer; (b) TEM sample retrieval and preparation

Samples for Raman spectroscopy were prepared as follows, 20 mL of the CMC/NaDDBS/SWNT solution was mixed with 10mL of epoxy. The mixture was placed it in a Brookfield viscometer equipped with a UL attachment, creating a very small gap ($R_b/R_c \leq 0.1$) that allowed the achievement of higher shears in viscous fluids. Once the shear flow was adequately developed, a hardener was added in order to promote cross-linking in the epoxy, thus rapidly increasing the solution viscosity as to prevent the de-alignment of the SWNTs in the solution. The samples were tested on a, Holo Probe VPT

system, with integrated fiber coupled Raman system (Kaiser Optical Systems, Inc.), using a 731 nm incident laser radiation and VV (parallel/parallel) configuration, to determine orientation of MWNTs.³⁴⁻³⁷ The samples were tested at various polarization angles ranging from 0 to 90 degrees, to determine the development of SWNT orientation after being subjected to shear flow.

5.3.2. Epoxy Composite

The composites were made with Araldite GY 6008, a clear liquid resin. According to the manufacturer's specification (Huntsman Advanced Materials Americas Inc.) the resin is a Bisphenol A Diglycidyl ether. The hardener used was ANCAMINE AEP curing agent (Air Products), and is an aminoethyl piperazine, 1-(2-, (AEP), a colorless liquid.

Each sample was made in a 30 mL graduated glass vial with a fairly uniform 27.5 mm diameter. The solutions used to initially disperse the carbon nanotubes were made in the same procedure as described previously,¹⁹⁸ and the final composite is a 10 gram sample with 0, ½, or 1 weight percent carbon nanotubes. The carbon nanotubes were first dispersed in the surfactant solutions and then added to the resin. That mixture was stirred at 100 RPMs for 24 hours at 80°C to evaporate off the excess water and allow for the resin and dispersed carbon nanotubes to mix. Then, the solution was allowed to cool to room temperature, after which hardener was added. Then it was stirred again at 100 RPMs for 10 minutes. A Brookfield DV-E viscometer with a stainless-steel rotating spindle having 19.0 mm diameter (O.D.) and 65.0 mm in length was used to align the carbon nanotubes.

The sample solutions were placed in a sample chamber that has a 8.5 mm gap between the sample chamber and the spindle, as shown in Figure 5.1a. In turn, the spindle was allowed to rotate for approximately 30 minutes (or until turbulent flow occurred) at 100 rpm (10.46 rad/s).

The samples were then tested on a Holo Probe VPT system, with integrated fiber coupled Raman system (Kaiser Optical Systems, Inc.), using a 731 nm incident laser radiation and VV (parallel/parallel) configuration to determine the orientation of the SWNTs.³⁴⁻³⁷ The samples were tested at various polarization angles ranging from 0 to 90 degrees to determine the development of SWNT orientation after being subjected to shear flow.

The samples were tested using dynamic mechanical analysis (DMA, TA Instruments Q800) to determine the effects of dispersing agents. The samples were tested at 0-150°C to obtain information across the glass transition temperature. The data collected was then analyzed and graphed to determine the elastic modulus, glass transition temperature, and trends within the data.

5.4. Viscous Polymer Flow Results and Discussion

5.4.1. Dispersion of SWNT

The high degree of aggregation of SWNTs is due to the high cohesive energy of the tubes that has been estimated to be on the order of 36 kT for each nanometer of length overlap between adjacent tubes, translating into several thousand kT for micron-long tubes.³⁸ Since maintaining a stable dispersion is a necessary condition for the utilization of SWNTs in various composite applications, the promotion of exfoliation and dispersion of

SWNTs has been a very active field of research in recent years. Coupling the effects of both surfactants and polymers, such as treatment with NaDDBS and CMC, may result in a superior and more stable dispersion of SWNTs, as shown schematically in Figure 5.2.

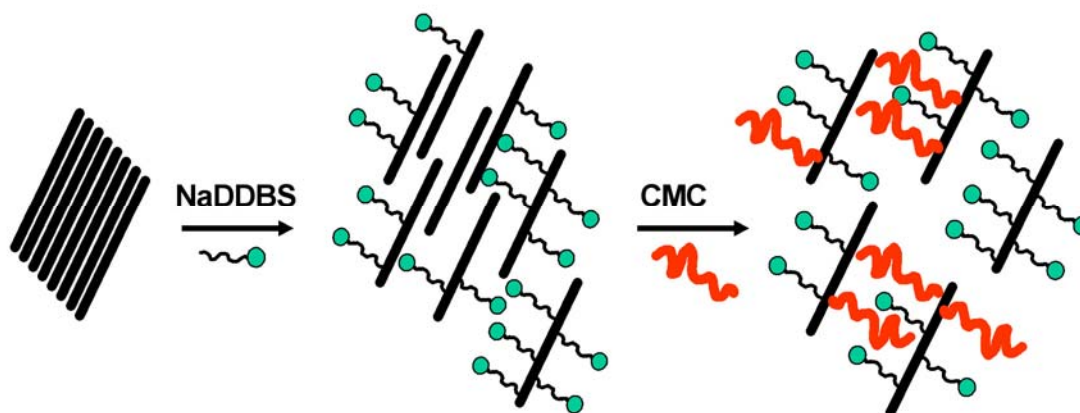
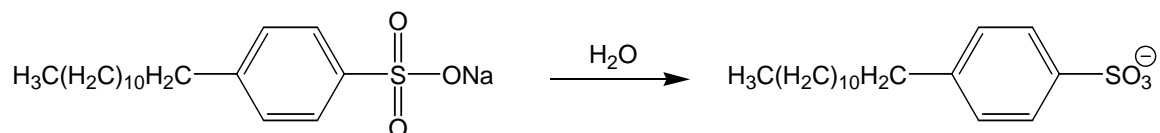


Figure 5.2: Schematic representation of the stabilization mechanism of carbon nanotubes: interaction between SWNT with NaDDBS, followed by the addition of CMC.

An example of an aqueous suspension of carbon nanotubes without proper dispersion is illustrated by the TEM image in Figure 23a. The addition of NaDDBS, an anionic surfactant, to the suspension results in the exfoliation and dispersion of the carbon nanotubes, as shown in Figure 5.3b. NaDDBS dissociates in an aqueous environment to generate a sulfonium group, as shown below:



The hydrocarbon moiety interacts with the surface of the carbon nanotube, while the anionic group is solubilized by the surrounding water molecules. This increases the solubility of the carbon nanotubes and allows their exfoliation and dispersion in the aqueous medium. Conversely, since the experimental procedure involves the sonication

of the SWNT suspensions, it is also quite likely that this generates considerable exfoliation of the nanotubes, followed by the adsorption of the surfactant molecules, which in turn, stabilizes the nanotubes due to steric repulsion.^{20,21,42,43}

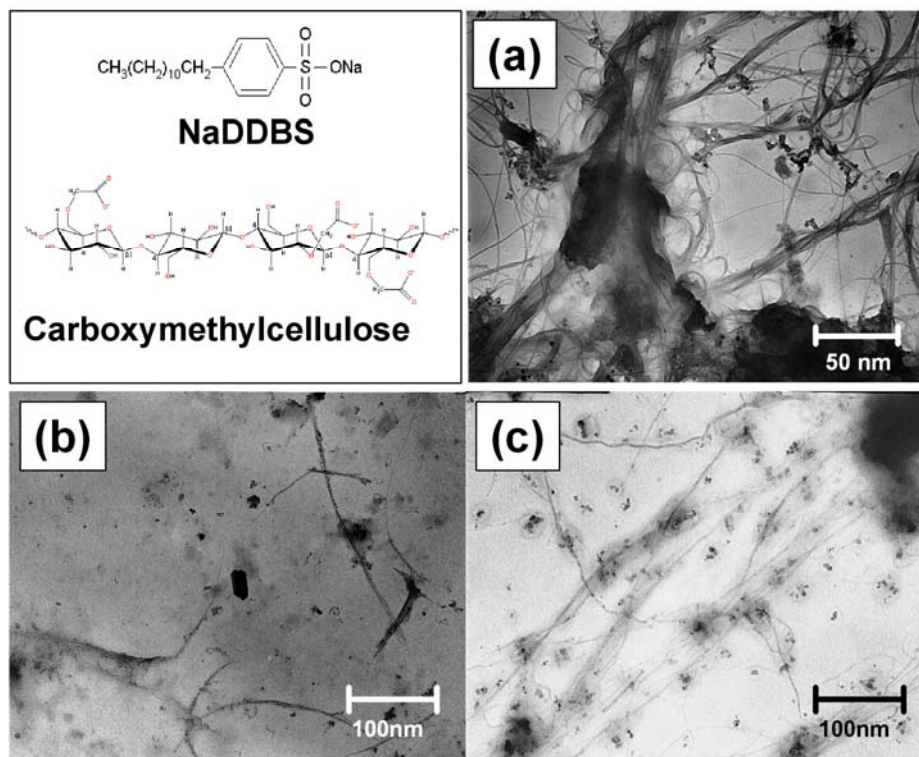


Figure 5.3: TEM micrographs of SWNT at different levels of dispersion and stabilization efficiency: (a) Undispersed carbon nanotubes; (b) Carbon nanotubes dispersed with NaDDBS; (c) Carbon nanotubes dispersed with NaDDBS and CMC. Note that the black spherical aggregates present in the image are the remnant metallic oxide catalyst particles used in the synthesis of the SWNT.

The addition of CMC to the SWNT/NaDDBS solution has a moderate effect on the resulting dispersion as shown in the TEM image in Figure 23c. CMC adsorbs weakly on the surface of the carbon nanotubes, most likely via the interactions of the $\beta 1$ moiety with the SWNTs.^{20,21} Because at low concentration the CMC molecules are largely uncoiled (intrinsic persistence length $L_{p0} = 160 \text{ \AA}$, indicating a semi-flexible polymer⁴⁷),

this interaction is most likely to occur with the polymer end segments, e.g. as shown in Figure 5.4.

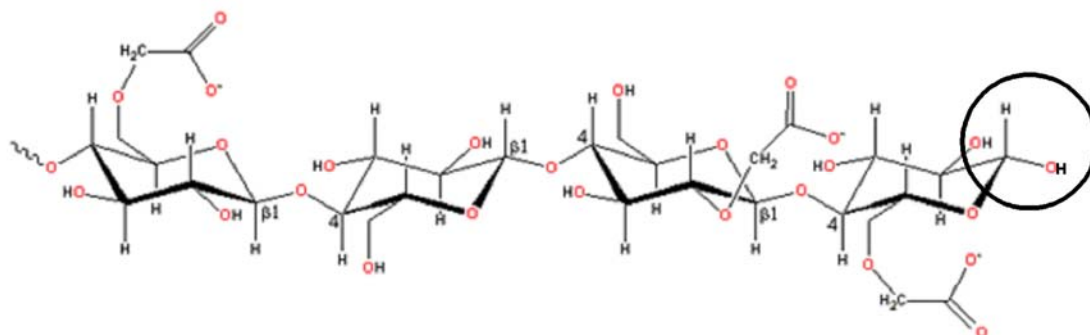


Figure 5.4: Carboxymethyl Cellulose polymer chain illustrating $\beta 1$ moiety

The abundance of carboxylic functional groups along the polymer chain will ensure the presence of a large number of associated water molecules, effectively increasing the hydrodynamic radius of the individual chains ($R_g \approx 1000 \text{ \AA}$,⁴⁸ as compared to $\approx 20 \text{ \AA}$, the size of the NaDDBS molecule), thus introducing a large steric hindrance into the system, that promotes additional dispersion and separation of the carbon nanotubes.

5.4.2 Orientation of SWNT in Shear Flow

A Brookfield viscometer was used to generate a shear flow for the alignment of the carbon nanotubes. Predictions for optimal shear forces generated by this set-up (see Figure 5.1) were based on non-Newtonian flow characteristics of the CMC-containing solutions (the fluid constants for this system were established separately) and on a gap for which the ratio of the inner cylinder and outer cylinder radii, R_b/R_c respectively, is 0.69, i.e. between 0.5 and 0.99 for which the model holds.⁴⁹ The measurement of the torque, T , necessary to maintain a constant angular velocity ω of the inner cylinder, is related to the

shear stress τ_w according to the relationship $\tau_w = \frac{T}{2\pi R_b^2 L}$, where L is the length of the inner cylinder in contact with the fluid. The shear rates and shear stresses obtained for the various systems that were examined are summarized in Table 5.1 and Figure 5.5a.

Table 5.1: Summary of the mechanical properties of the various SWNT-containing solutions.

Conditions	NaDDBS		NaDDBS/SWNT		CMC/NaDDBS		CMC/NaDDBS/SWNT	
Angular velocity (rad/s)	Shear Rate (s ⁻¹)	Shear Stress (MPa)	Shear Rate (s ⁻¹)	Shear Stress (MPa)	Shear Rate (s ⁻¹)	Shear Stress (MPa)	Shear Rate (s ⁻¹)	Shear Stress (MPa)
1.26	4.27	0	4.70	0	4.70	0.35	4.70	0.36
3.14	10.67	0.20	11.75	0.12	11.75	1.14	11.75	1.15
5.24	17.78	0.33	19.58	0.33	19.58	1.86	19.58	1.87
6.28	21.34	0.45	23.49	0.48	23.49	2.21	23.49	2.22
10.48	35.57	0.74	39.15	1.10	39.15	3.65	39.15	3.68

In the absence of polymer, the shear stresses that are due to the presence of the carbon nanotubes are negligible at low angular velocities, but become considerable at high angular velocities, as shown in Figure 5.5a. For example, at 6.28 rad/s (60 RPM), the shear stress at the wall, τ_w , exerted by the carbon nanotubes is ~30 kPa, while at 10.48 rad/s (100 RPM), it is ~350 kPa. Conversely, the presence of CMC in the solution has the effect of increasing the shear stresses of the system at all angular velocities, due to the higher viscosities exhibited by the polymer medium. Moreover, the shear stresses that are

due only to the presence of the carbon nanotubes in the solution are small, but increase linearly with the angular velocity, as shown in Figure 5.5b.

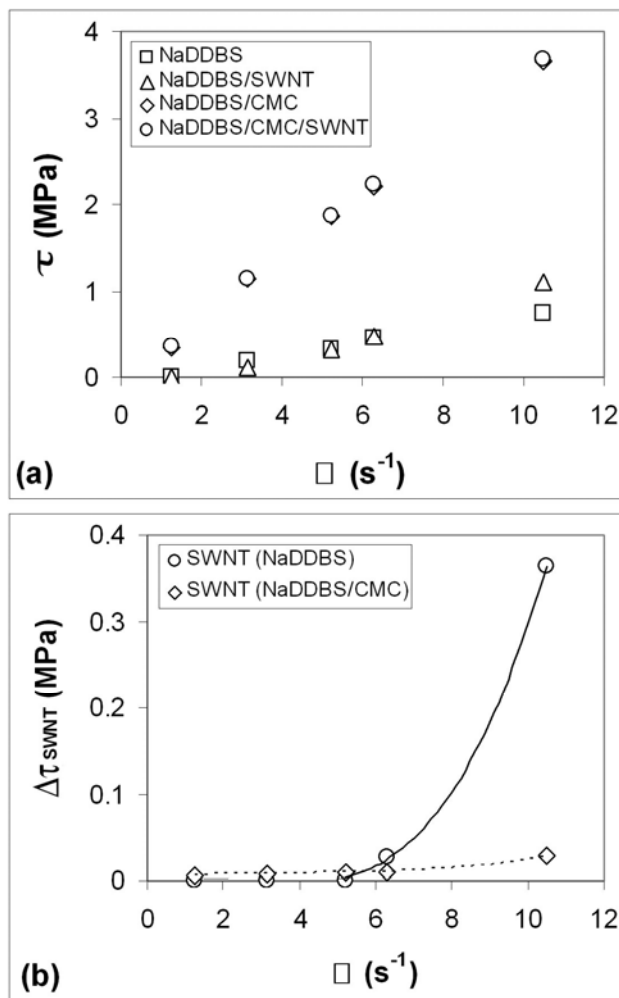


Figure 5.5: Summary of the calculated shear stresses of the various SWNT-containing solutions used in the various experiments: (a) Plots of shear stresses as a function of angular velocity; (b) Plots of the shear stresses originating from the contribution of pure SWNT in the various systems as a function of angular velocity.

It is important to note that CMC may be considered as a uniformly charged semi-flexible cylinder with a radius of 0.95 nm and an average coiled length of ~ 250 nm, and hence

each chain may be viewed as having comparable dimensions to those of SWNTs. Under these circumstances, the presence of the CMC chains in solution "catalyzes" the dynamic behavior of the carbon nanotubes and in effect attenuates the development of the stresses associated with their movement in the solution.⁵⁰ This is due to the fact that the CMC molecules are tethered to the carbon nanotubes (albeit via weak interactions), and hence, create a network of entanglements that in effect, lowers the change in shear stress of the system.

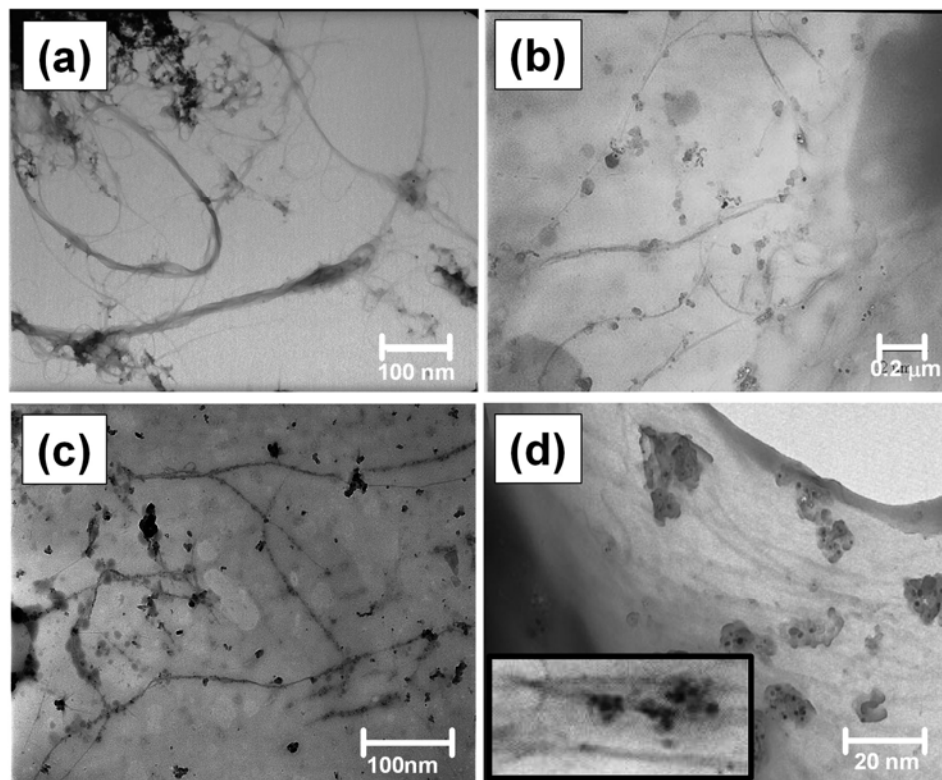


Figure 5.6: TEM micrographs of the orientation attempts of several systems containing SWNT: (a) Undispersed carbon nanotubes in a 1 wt% CMC suspension subjected to shear flow at 100 rpm; (b) Carbon nanotubes dispersed with NaDDBS and CMC and subjected to shear flow at 30 rpm; (c) Carbon nanotubes dispersed with NaDDBS and CMC and subjected to shear flow at 60 rpm; (d) Oriented carbon nanotubes dispersed with NaDDBS and CMC and subjected to shear flow at 100 rpm. The inset image is a four-fold magnification of the larger image (same scale bar = 5 nm) showing in more detail the local orientation of the surface-modified SWNTs. Note that the black spherical aggregates present in these images are the remnant metallic oxide catalyst particles used in the synthesis of the SWNTs.

The development of directional anisotropy in carbon nanotube solutions, when subjected to shear flow stresses, was possible only in systems in which the carbon nanotubes were dispersed by the cooperative surface interactions with both NaDDBS and CMC. Subjecting a SWNT suspension to shear flow at high angular velocities did neither contribute to their exfoliation nor to their orientation, as shown in Figure 5.6a. No

noticeable orientation of the SWNT was observed in systems in which the dispersion was achieved with NaDDBS only.

For systems in which effective dispersion of the carbon nanotubes was achieved by the combined action of both NaDDBS and CMC, no alignment was observed for lower angular velocities, as can be seen in Figures 5.6 b,c. The only system in which tube alignment was observed was for the NaDDBS/CMC/SWNT solution that was subjected to shear stresses at the highest angular velocity used in the experiments (10.48 rad/s), as shown in Figure 5.6sd.

Additional confirmation for the results illustrated by TEM regarding the alignment of the SWNT was obtained with Raman spectroscopy. Since the Raman intensity of a vibration depends on the relative directions of the crystal axis and the electric wave polarization of the incident and scattered light, this technique may also be used to determine the orientation of nanotubes in polymer matrices.^{34-37,51-56} Figure 5.7a shows the orientation-dependent Raman spectra of SWNTs with different angles between the polarization of the incidence laser light and the nanotube axis using VV (parallel polarization of the incidence and scattered light) configuration. The G band at 1594 cm^{-1} , corresponding to the resonantly excited metallic SWNTs, shows a maximum intensity when the polarization of the incident radiation is parallel to the nanotube axis (i.e. $\alpha = 0^\circ$), and is minimal when the polarization of the incident radiation is perpendicular to the nanotube axis (i.e. $\alpha = 90^\circ$).⁵²⁻⁵⁶ The Raman spectra allow a direct comparison of experimental data with theoretical calculations, as shown in Figure 5.7b.

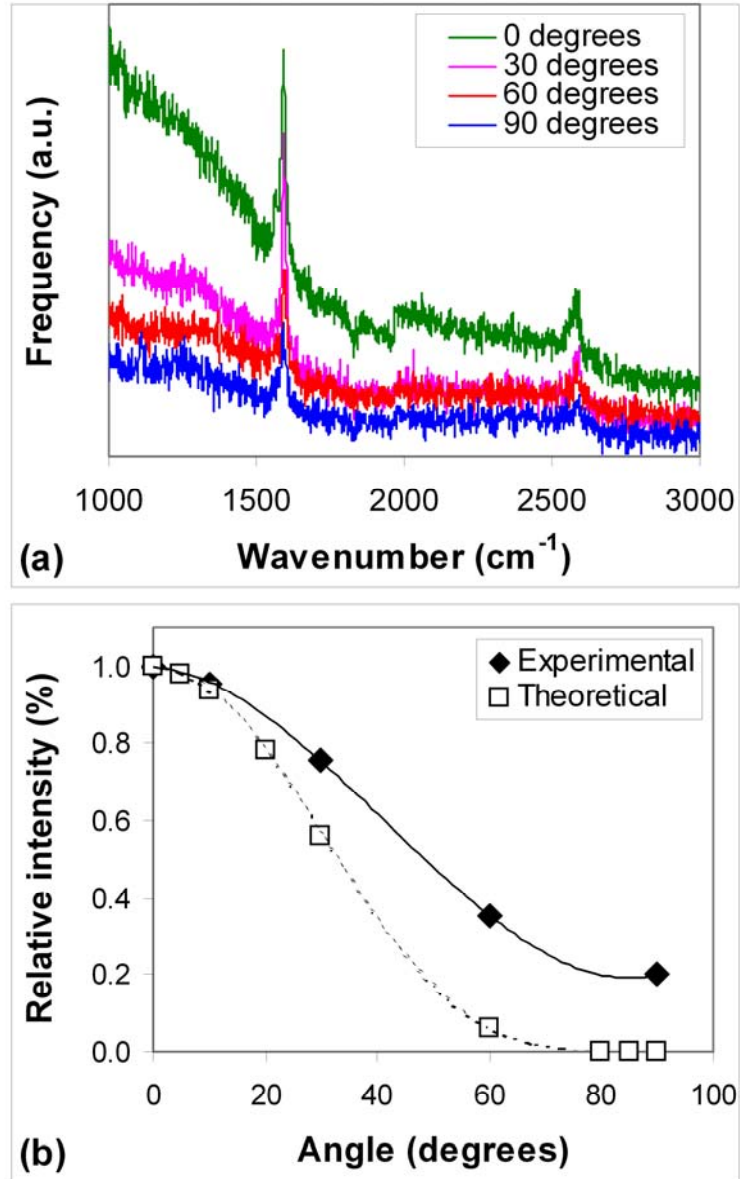


Figure 5.7: Raman spectra of samples containing SWNTs that were subjected to shear flow: (a) Orientation-dependent Raman spectra of SWNTs with different angles (from 0 to 90 degrees) between the polarization of the incidence laser light and the nanotube axis using VV (parallel polarization of the incidence and scattered light) configuration. (b) The direct comparison of the experimental relative intensities of the 1594 cm⁻¹ G band as a function of the angle of polarization of the incident radiation, with theoretical calculations.

The experimental angular dependencies in our system exhibit a non-negligible deviation from the selection rules predicted by theoretical studies, where intensities scale with

$\cos^4\alpha$.⁵⁵ These differences may be attributed to depolarization effects generated by the pronounced anisotropic structure of the nanotubes and to electronic resonance effects. As shown in Figure 5.7, there appears to be some fluorescence due to the CMC matrix, but it also illustrates that the nanotubes are highly oriented in the polymer matrix.

These results illustrate the fact that the orientation of carbon nanotubes in a polymer matrix by the application of shear forces can be achieved only if two requirements can be satisfied: (a) the carbon nanotubes are well dispersed in the polymer matrix and (b) the shear forces applied to the dispersed carbon nanotubes are large enough to induce their orientation. In general, the presence of the CMC molecules, given their size and their semi-flexible characteristics, provided a molecular template that promoted carbon nanotube alignment at lower shear stresses.

5.5 Epoxy Composite Results and Discussion

5.5.1 Dispersion of SWNTs in Viscous Epoxy Flow

The addition of the Pluronic F108, a PPO-PEO-PPO block copolymer helps to suspend, exfoliate, and disperse the tubes by increasing the distance between the CNT chains, as shown in Figure 5.8. It has been found that some pluronics allow the dispersion of carbon nanotubes, but the carbonaceous particles and catalyst particles precipitate out limiting their strength hindrance.⁸⁴ The lyophilic block associates with the solution, in this case water, and the lyophobic block associates with the carbon nanotubes separating the carbon nanotubes, reducing the van der Waals forces.

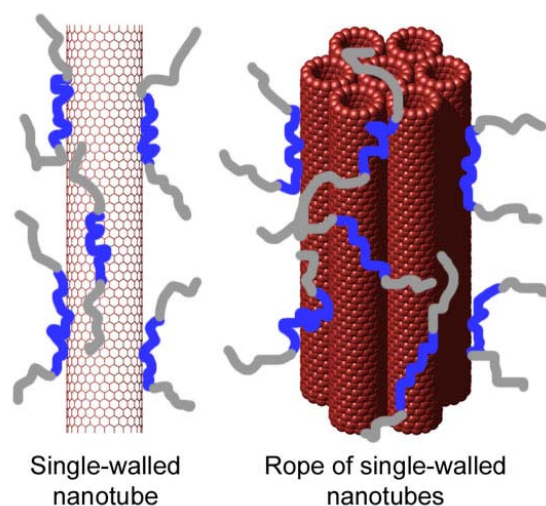


Figure 5.8: Illustration of the Pluronic stabilization mechanism of carbon nanotubes

Conversely, since the experimental procedure for both surfactant agents involves the sonication of the SWNT suspensions, it is also quite likely that this generates considerable exfoliation of the nanotubes, followed by the adsorption of the surfactant molecules, which in turn, stabilizes the nanotubes due to steric repulsion.^{69, 73, 199}

5.5.2 Orientation of SWNTs in Epoxy Composites

A Brookfield viscometer was used to generate a shear flow for the alignment of the carbon nanotubes. The predictions for optimal shear forces generated by this set-up (see Figure 5.1) were based on non-Newtonian flow characteristics of the CMC-containing solutions previously tested. Therefore, the polymer medium used in this case epoxy, the goal is to maintain this behavior and create an aligned carbon nanotube composite.

The carbon nanotube composite samples were unable to be analyzed by transmission electron microscopy (TEM) due to the high molecular weight and difficulty in analyzing polymer solutions in TEM. However, the samples were able to be analyzed using DMA and Raman spectroscopy.^{34-37,51-56}

5.5.3 Raman Spectroscopy of SWNT in Epoxy Composites

The orientation-dependent Raman spectra of SWNT can be determined with different angles between the polarization of the incidence laser light and the nanotube axis using VV (parallel polarization of the incidence and scattered light) configuration. The G band which is found around 1591 cm^{-1} , corresponds to the resonantly excited metallic SWNT and shows a maximum intensity when the polarization of the incident radiation is parallel to the nanotube axis (i.e. $\alpha = 90^\circ$) and is minimal when the polarization of the incident radiation is perpendicular to the nanotube axis (i.e. $\alpha = 0^\circ$).^{130, 143, 200-202}

The analysis of the Raman spectra for this particular epoxy system can't determine if alignment occurred, due to the Raman peaks of the epoxy. The Raman spectra of the aligned epoxy and epoxy only samples are shown in Figure 5.9 (a,b)..

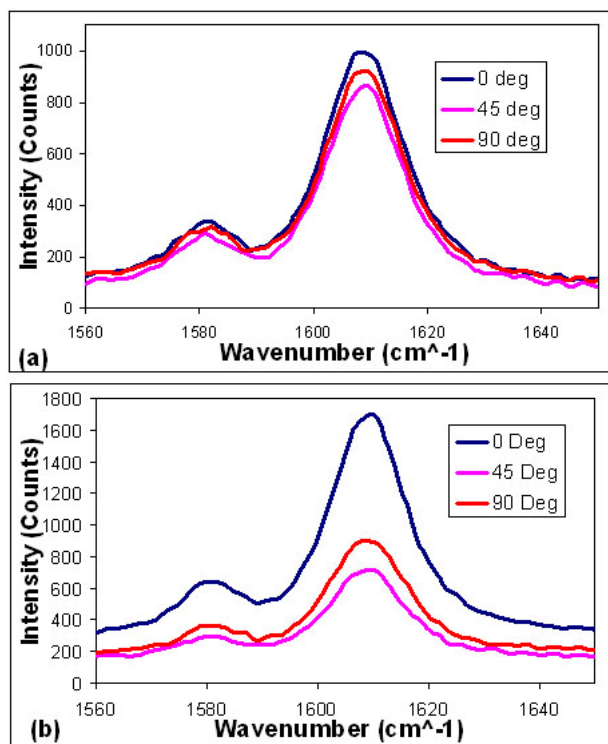


Figure 5.9: Raman spectra of the (a) aligned epoxy and (b) epoxy only samples at various orientations.

From this data, it can be seen that there are two peaks that surround the 1591 cm^{-1} G band peak that allows the orientation of carbon nanotubes to be determined. Therefore, when looking at the G band peaks for the various samples at various angles, Figure 5 (a,b,c,d), significant amount of noise is present in the samples, and the appearance of two joined peaks is seen in all data sets. Therefore, we can't completely determine that we have orientation in the samples based on solely on the G band peak. However, the systems depicted in Figure 5 (a,b) show increased intensities in the G band peak, which indicate a significant amount of aligned carbon nanotubes.

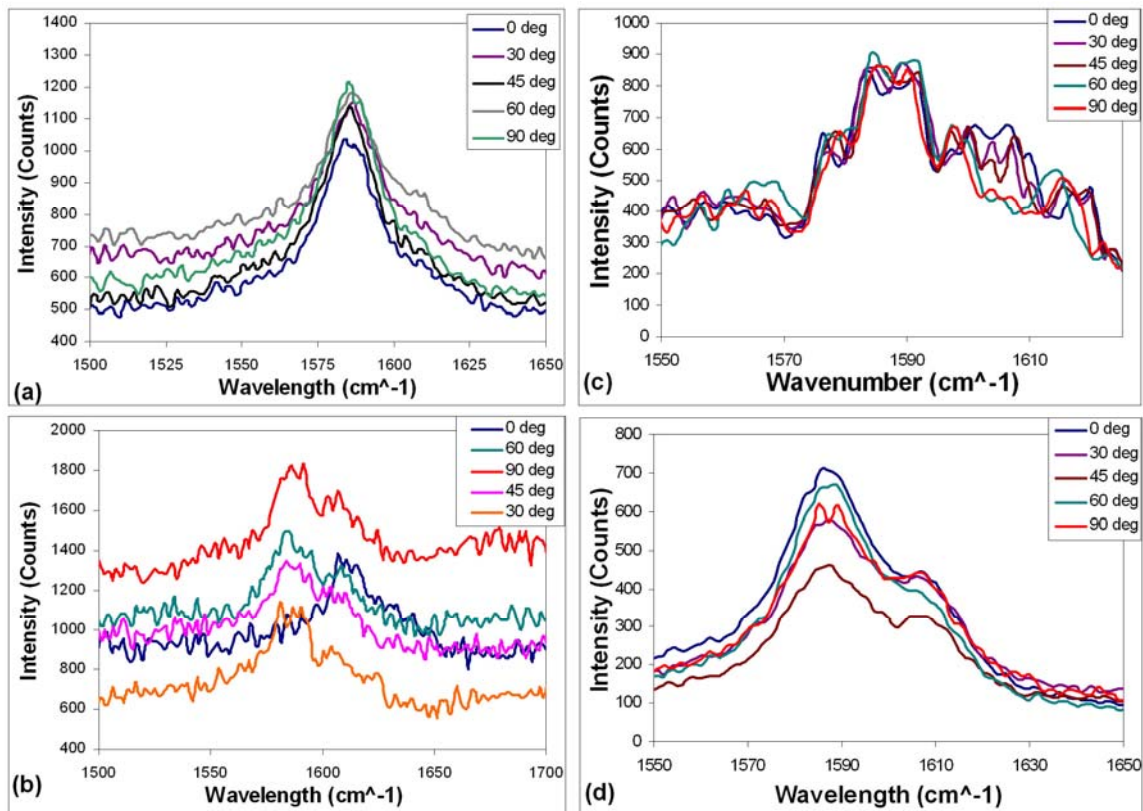


Figure 5.10: Raman spectra of (a) $\frac{1}{2}$ wt% CNT-NaDDBS, (b) $\frac{1}{2}$ wt% CNT-Pluronic, (c) 1 wt% CNT-Pluronic, and (d) 1 wt% CNT-NaDDBS at various angles of orientation.

It was previously determined by Frogley, *et al.*¹²⁹, that the G band peak is not the only peak that alignment can be determined from, but other peaks can be used, such as the D^* band, a second overtone of the D band whose location depends upon the laser excitation energy used and the dispersion relation used between the D and D^* bands. For this system the band is around $\sim 2600 \text{ cm}^{-1}$.¹²⁹ Therefore, the data from the samples were reanalyzed to determine if that peak could be used. From this peak, the alignment of our samples was confirmed for the NaDDBS system, Figure 5.11(a,b)

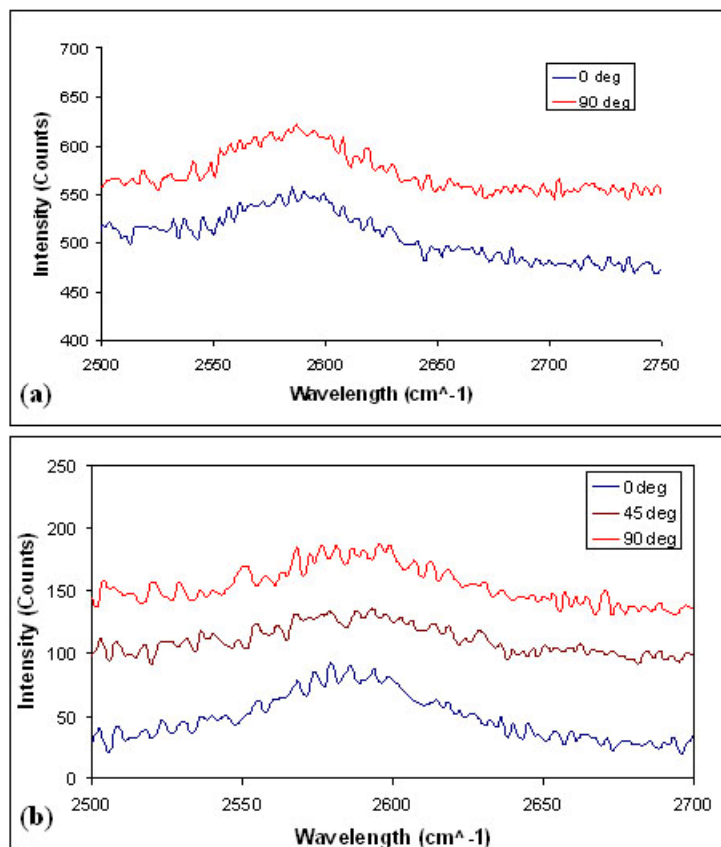


Figure 5.11: Raman spectra of D' peak for alignment analysis (a) 1/2 wt% NaDDBS (b) 1 wt% NaDDBS

The samples which used pluronics to disperse the carbon nanotubes didn't appear to have any alignment that was seen in the Raman spectra and in one of the samples, there was no apparent D' band peak, due to peak overlap. However, the intensity difference between the peaks is very small (on the order of 80 cm⁻¹). Therefore, no conclusive answer the question (are the tubes aligned?), can be made. Since Raman spectroscopy only looks at a small area of the samples the DMA tests of the samples were also tested in the direction of alignment and perpendicular to alignment to determine the difference in mechanical properties.

5.5.4 Dynamic Mechanical Analysis of SWNTs in Epoxy Composites

The goal of using shear flow on carbon nanotube composites was to promote the directional alignment of the carbon nanotubes, a fact that would be expected to improve the mechanical properties of the composite. This improvement in the mechanical properties would most notably be in the direction in which the CNTs are oriented. Composite samples were prepared to allow compression testing of the samples in two directions, of the same sample, allowing for alignment to be determined if there is a significant difference in the modulus in the aligned direction.

5.5.4.1 Effect on Glass Transition Temperature

The effects on the glass transition temperature should be relatively simple to predict. It is expected that increasing the extent of alignment and orientation of the carbon nanotubes and epoxy matrix chains¹²⁷ will result in an increase in the glass transition temperature of the composite because the ordering of the chains/CNTs will increase the entropy of the system.¹²³ The effects of alignment on the glass transition temperature are well documented.¹²³ Therefore, it was expected that by increasing the carbon nanotube content, and thus the degree of alignment of the carbon nanotubes will increase and as a result, the glass transition temperature of the composites will increase as well.

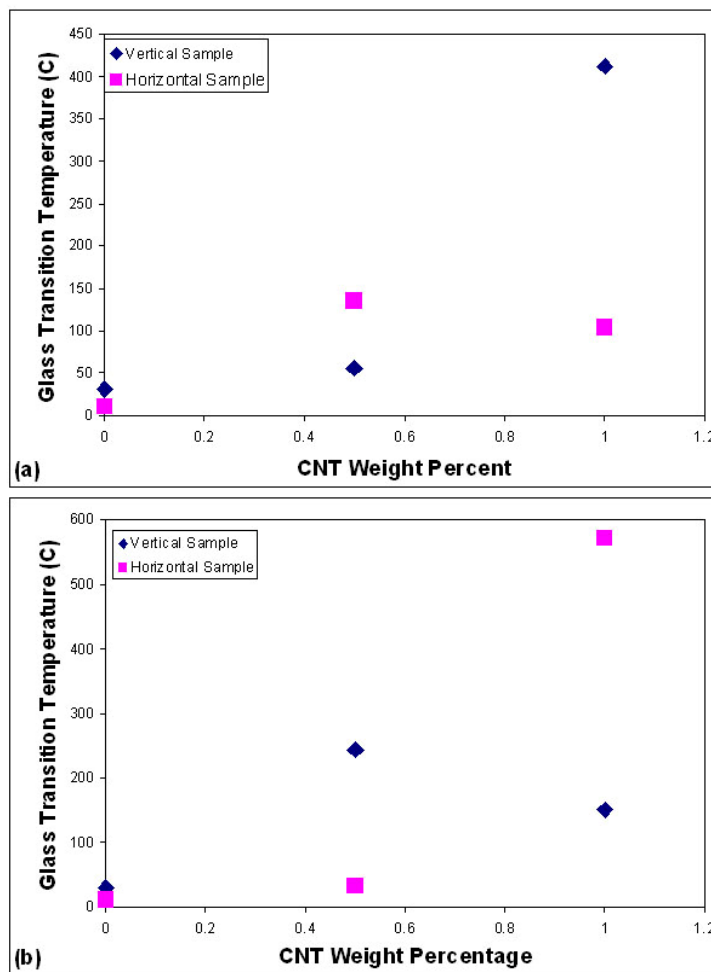


Figure 5.12: Glass Transition Temperature data for (a) NaDDBS Samples (b) Pluronic Samples

This was exactly the result that was found for the system that used the surfactant, NaDDBS, as a dispersing agent. Figure 5.11a, illustrates that the glass transition temperature, T_g , does just what was predicted. However, Figure 5.11b, illustrates the exact opposite effect on the T_g for the Pluronic system. The reason for this could be due to: (a) reverse orientation, where alignment occurred perpendicular to the shear flow due to the high molecular weight of the Pluronic compared to that of the NaDDBS, or from chain interactions of PEO-PPO could have prevented the sample from orienting in the

direction of shear flow, (b) no overall orientation occurred, but there could be localized regions of oriented and un-oriented CNTs, which could cause there to be samples with increase T_g s.

5.5.4.2 Effect on Storage and Loss Moduli and Tan Delta

The effects of the alignment on the storage modulus and loss modulus appear to confirm the assumptions made previously, Figure 5.13(a-d). The storage and loss modulus data for the NaDDBS samples were as expected. There was a higher storage modulus and corresponding loss modulus for the samples tested in the direction of alignment. Although generally all epoxies are known for their structural properties this particular epoxy was not very strong. The epoxy was chosen based on its ability to harden at room temperature. So even though the overall modulus data is not very high, at ½ wt% CNTs and 1 wt% CNTs, the modulus in the direction of predicted alignment increased by 1100 % and 67%, respectively, in the NaDDBS samples. However, the modulus of the ½ wt% CNT composite perpendicular to flow had a modulus increase of 1100% also, but at 1 wt% the modulus increase was 875%. This could illustrate that there could possibly regions in both samples of localized aligned parallel as well as perpendicular to flow. This could yield a composite that has potential for structural applications that require strength in biaxially versus just uniaxial strength. The data provided here also appears to be significantly higher than previously reported^{58, 128, 203, 204} and may lead to an ideal method or creating structural carbon nanotube polymer composites.

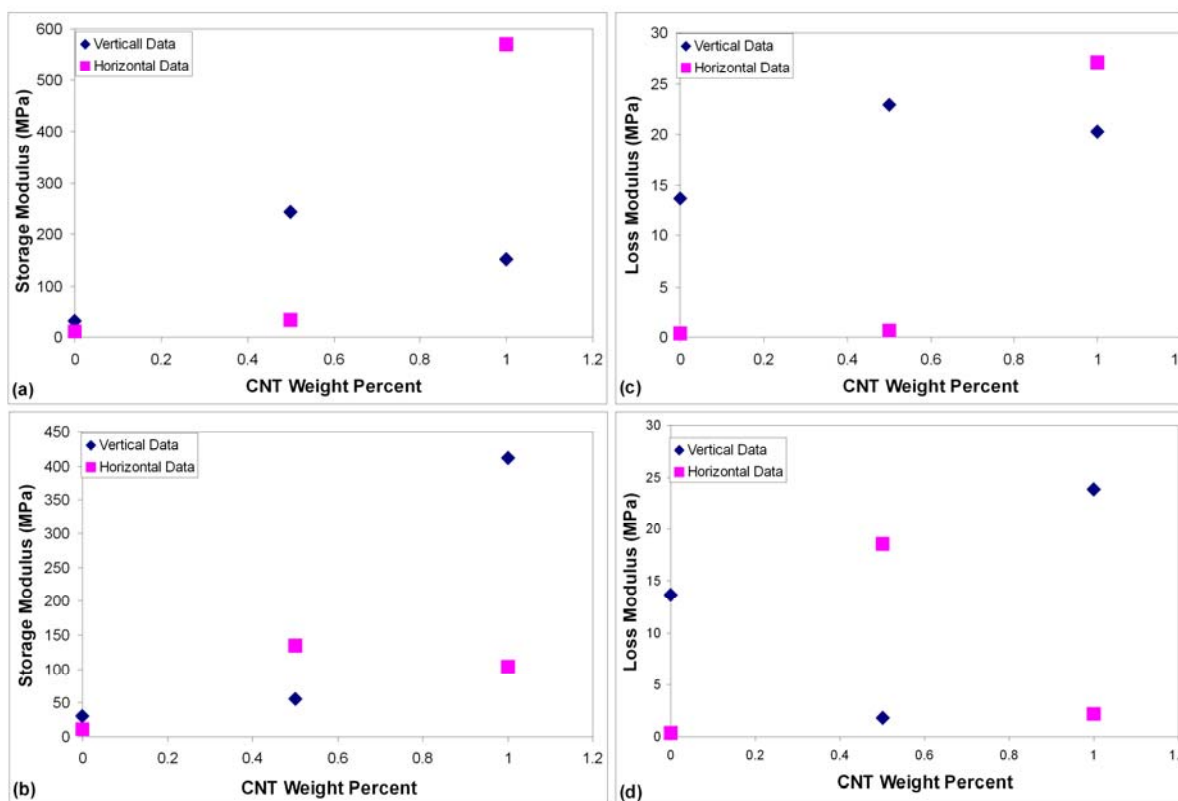


Figure 5.13: The effect of the alignment on the Storage Modulus for (a) Pluronic Samples (b) NaDDBS Samples and the Loss Modulus for (c) Pluronic Samples (d) NaDDBS Samples

The effects of alignment for the Pluronic samples seem to illustrate there is either (a) alignment perpendicular to flow or (b) localized areas of perpendicular alignment. The storage moduli for the sample tested perpendicular to flow were significantly higher than those tests in the direction of predicted alignment. Again the overall modulus data is not very high but at $\frac{1}{2}$ wt% CNTs and 1 wt% CNTs the modulus perpendicular to flow increased by over 200% and 5000%, respectively, whereas the modulus parallel to flow increased by 300% and 600%, respectively.

The data shown in Figure 5.14 (a,b), confirms the results that have been concluded previously. The results obtained for the two polymer systems were not

uniform. For the Pluronic samples the $\tan \delta$ appears to decrease with increasing CNT content, whereas with the NaDDBS samples the $\tan \delta$ appears to initially decrease and then increase.

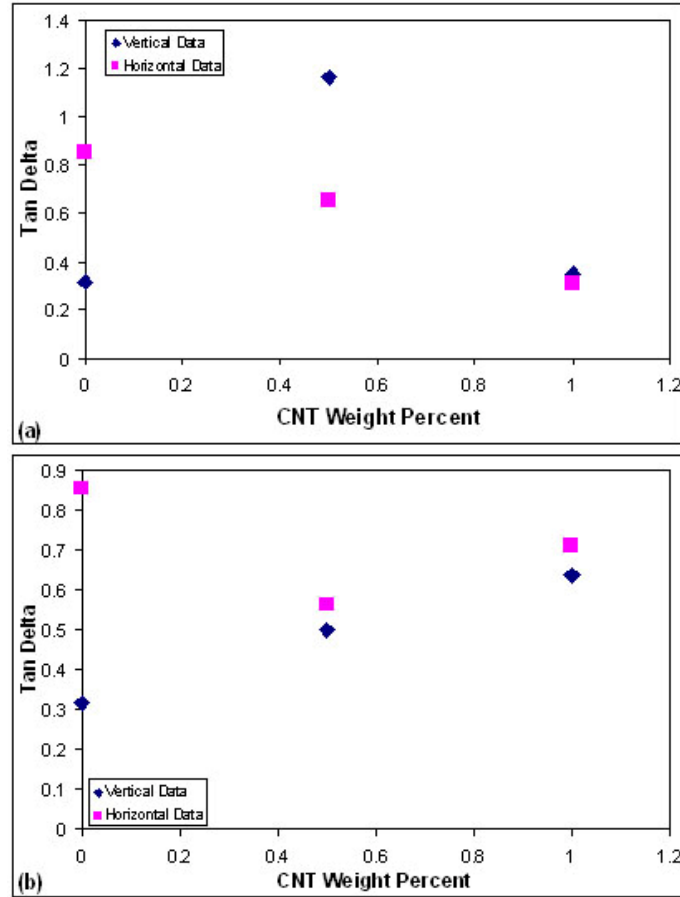


Figure 5.14: The effect of alignment and CNT weight percent on Tan δ for (a) Pluronic Samples (b) NaDDBS Samples

The decrease in $\tan \delta$ behavior could be caused by inhibited chain movement resulting in chain scission or chain entanglement due to the presence of the carbon nanotubes in the Pluronic system. However, the increase in $\tan \delta$ could be due to organized and aligned carbon nanotubes that do not require a significant amount of chain restructuring resulting in adequate dissipation of energy. This non-uniform behavior

could be due to the localized regions of parallel and perpendicular alignment of carbon nanotubes in the samples.

Therefore, in this research we have effectively been able to increase the strength of the composite material significantly over that of the epoxy. However, the goal of increase strength uniaxially by inducing alignment was not obtained. Modifications of this procedure may very lead to alignment by reducing the viscosity of the polymer, removing the system before turbulent flow can begin, and using a viscometer/rheometer with higher viscosity ranges to track the viscosity data.

5.6 Summary of Viscous Polymer and Epoxy Composite Systems

In this work we have shown that the addition of an anionic surfactant or a Pluronic to a carbon nanotube aqueous suspension facilitated their dispersion. It was found that in the surfactant alone in solution was ineffective as a tool of enhancing the ability to orient them when subjected to shear forces. We have also determined that the addition of CMC, a weakly-binding, semi-flexible ionic polymer and mild detergent, to the surfactant/nanotube system, helped increase carbon nanotube dispersion and was a necessary condition for the onset of the orientation of the carbon nanotubes in the polymer solutions, provided the shear stresses that developed in the system were sufficiently high. However, the incorporation of the CNT solution into an epoxy matrix may have inhibited the alignment of the CNTs when subjected to shear forces. From this, we have learned that it may possibly create regions of localized aligned carbon nanotubes parallel and perpendicular to the shear forces. The data was determined to significantly increase stiffness of the carbon nanotube polymer composite.

CHAPTER 6

PROPERTIES OF CARBON NANOTUBE-POLYMER COMPOSITES ALIGNED IN A MAGNETIC FIELD

6.1 Overview

In this chapter, a magnetic field was used to align carbon nanotubes in an epoxy and the properties of the resulting composites were explored. Section 6.2 gives a brief introduction and background of previous research done on polymer composites and polymer nanotube composites. Section 6.3 details the experimental procedure used to align the carbon nanotubes. Section 6.4 describes the results of the composites that were placed in a magnetic field. In conclusion, Section 6.5 describes summarizes the alignment results of the two systems. The next chapter will use the research to improve upon the alignment processes.

6.2 Introduction

Producing SWCNT-reinforced polymer-based composites in which the SWCNTs are both well dispersed and aligned, so that the full potential of their reinforcing capacity will be exhibited, has become a daunting task. There have been several different methods to align carbon nanotubes in a magnetic field.^{97, 127, 190} However, a problem with these alignment processes arises when combining the carbon nanotubes with the polymer matrix to form the composite materials. Under the experimental conditions, a well-

aligned array of carbon nanotubes tends to become isotropic and cluster upon mixing into the composite. Hence, the alignment of the carbon nanotubes prior to mixing into a composite is reversed, and once again, they may revert to random orientations.¹⁹⁵

In this research, both SWCNTs and MWCNTs were embedded in two different epoxy matrices Aeropoxy (AP) and Coldfix (CF), in order to determine the effect of alignment on the mechanical properties of the resulting composites. Despite the fact that MWCNTs have a lower elastic modulus than SWCNTs, they are easier to manufacture at low cost and relatively high yields, and hence, constitute a reasonable practical alternative to the use of high-cost SWCNTs.^{1, 205} The alignment of the carbon nanotubes in the epoxy matrices was indirectly determined by probing the various mechanical characteristics of the composites, and directly verified by Raman spectroscopy. The goal of the work was to determine if indeed the mechanical properties exhibited by the composites are correlated with CNT alignment, as expected, and if this alignment is indeed induced or aided by the applied magnetic field.

6.3 Experimental Procedure

This research expands upon previous research by Garemstani *et al.*⁹⁷ and Al-Haik *et al.*¹²⁷, where it was determined that a polymer epoxy underwent alignment in the presence of an external magnetic field. The samples were produced with ~3 wt% SWCNTs and MWCNTs purchased from Carbon Nanotechnologies, Inc. The SWCNTs and MWCNTs were dispersed ultrasonically in the resin, and the magnetic processing was carried out at the National High Magnetic Field Laboratory (NHMFL) at the Florida State University. The samples were produced according to the same methods and

concentrations as described by Al-Haik *et al*¹²⁷ having dimensions of varying lengths and widths, ranging from 7 mm by 4 mm to 40.5 mm by 4.8 mm. The samples are comprised to two different types of epoxies: Aeropoxy (AP) and Caldofix (CF). Aeropoxy, which is a medium viscosity (~900 cps), unfilled, light amber laminating resin designed for structural applications,¹²⁷ was used for half the samples. According to specifications from the manufacturer (PTM&W industries, Inc.), the components of the epoxy used here are the following: (a) Aeropoxy PR2032 (AP), a material containing diphenylolpropane (bisphenol A) and a multifunctional acrylate, and (b) the hardener component Aeropoxy PH3660, which is a modified amine mixture.¹²⁷ The epoxy contained also some acrylic monomers.¹²⁷ Caldofix (CF) epoxy, which is a cold cure epoxy resin generally used for embedding metallographic samples, with a viscosity of ~900 cps, was used for the remaining samples. According to specification from the manufacturer (Struers), the components of the epoxy used here were bisphenol A-epichlorhydrin and bisphenol F-epichlorhydrin. It was previously determined that the addition of CNTs has little effect on the viscosity measurements of viscous polymer solutions,¹⁹⁸ and therefore, the viscosity of the composite mixture was assumed to be the same as that of the epoxy.

The samples were tested on two different DMA instruments due to the wide range of samples sizes. Half the samples were run using a DMTA 2890 (TA Instruments), while remaining half of the samples were run using an RSA III. The individual sample sets were tested from room temperature, ~25 °C to 250 °C, and repeated 5 times. The heating ramp rate was 5°C and the frequency was 1 kHz. The samples varied by epoxy

type, carbon nanotube type, and magnetic field strength. A detailed summary of the sample experimental and calculated data is shown in Table 6.1.

The data collected was then analyzed and graphed to determine the elastic modulus, glass transition temperature, and trends within the data. The samples were then tested with a DSC Q100 (TA instruments) differential scanning calorimeter, using a cyclical temperature test from 0–100 °C at a heating rate of 10 °C per minute. This allowed the comparison between the T_g values obtained by thermal analysis and by dynamic mechanical analysis.

Raman spectroscopy was used in order to determine the presence and extent of the alignment of the carbon nanotubes in the epoxy matrix as a result of the application of the magnetic field. The samples were tested on a Holo Probe VPT system, with integrated fiber coupled with a Raman system (Kaiser Optical Systems, Inc.), using a 731 nm incident laser radiation and VV (parallel/parallel) configuration.²⁰⁶⁻²⁰⁹ To ensure that the data was accurate, the samples were tested on a flat surface, and the testing site for each angle remained the same. The samples were tested at various polarization angles ranging from 0 to 90 degrees, to determine the development of CNT orientation after being subjected to a magnetic field.

Table 6.1: Summary of the measured and calculated mechanical properties, such as glass transition temperature, elastic modulus, storage modulus, and loss modulus for the various samples characterized in this work. Note that the concentration of CNTs in the samples was $\sim 3 \text{ wt}\%$ ⁹⁷.

Epoxy	CNT Type	Magnetic Field (Tesla)	Tan Delta	Modulus		Tg (°C)		Young's Modulus (MPa)
				Loss (MPa)	Storage (MPa)	DSC	DMA	
AP	none	15	0.817	3070	2508	58.8	75.6	3964
AP	SWNT	0	0.752	248	1330	55.1	80.6	1353
AP	SWNT	15	0.649	224	2277	70.9	77.2	2288
AP	SWNT	25	0.726	219	2002	55.6	83.8	2014
AP	SWNT	25	0.634	270	2760	62.5	72.4	2773
AP	MWNT	0	1.120	22	1099	54.2	70.8	1099
AP	MWNT	15	0.825	86	1295	64.6	65.6	1298
AP	MWNT	25	0.565	117	3377	64.3	86.5	3379
AP	MWNT	25	0.530	150	2492	48.1	63.7	2497
CF	none	15	1.139	205	1914	60.2	79.1	1925
CF	none	25	1.260	285	2900	45.5	64.3	2914
CF	SWNT	0	0.764	249	1330	54.9	80.6	1353
CF	SWNT	15	1.127	117	1099	51.1	77.1	1105
CF	SWNT	25	1.093	244	982	68.3	73.5	1012
CF	SW/MW	0	1.102	274	2051	52.4	85.2	2069
CF	MWNT	15	0.916	201	1952	79.1	97.9	1963
CF	MWNT	25	1.174	113	1192	54.8	64.6	1197
CF	MWNT	25	1.197	244	1430	52.0	65.8	1450

6.4. Results and Discussion of Magnetic Field Aligned Carbon Nanotubes

The properties of polymers, as reflected by their response to externally applied cyclical stresses, are dependent on both time and temperature. The dynamic mechanical analysis (DMA) of polymers, polymer blends and polymer-based composites provides important insight into the intimate conformation of the polymer chains in the sample, as well as the interactions of these chains with other components in the composite

system.²¹⁰⁻²¹² Hence, the dynamic mechanical measurements of polymers allow the evaluation of the temperature dependence of the dynamic modulus and give direct information on various other characteristic structural parameters,²¹⁰⁻²¹² such as dynamic viscoelastic behavior, glass transition temperature (T_g), storage and loss moduli, and $\tan \delta$. The results of these measurements for all samples were compared, and allowed the evaluation of the effect of a magnetic field on the polymer composites.

6.4.1. Effect on Glass Transition Temperature

The initial goal of using a magnetic field on carbon nanotube composites was to promote the directional alignment of the carbon nanotubes through polymer-CNT interactions; this would be expected to improve the mechanical properties of the composite. The effects on the glass transition temperature should be relatively simple to predict. It is expected that increasing the extent of alignment and orientation of the carbon nanotubes and epoxy matrix chains^{97, 127} will result in an increase in the glass transition temperature of the composite^{127, 213, 214}. This effect is well documented and arises from the increase in matrix packing density upon chain alignment, and hence, an increase in matrix rigidity.^{213, 215-217} Therefore, our working hypothesis is that by increasing the magnetic field strength applied to the samples, the degree of orientation and alignment of the polymer epoxy chains followed by carbon nanotubes alignment will increase, and as a result, the glass transition temperature of the composites will increase as well. This hypothesis was tested using two polymer epoxy matrices.

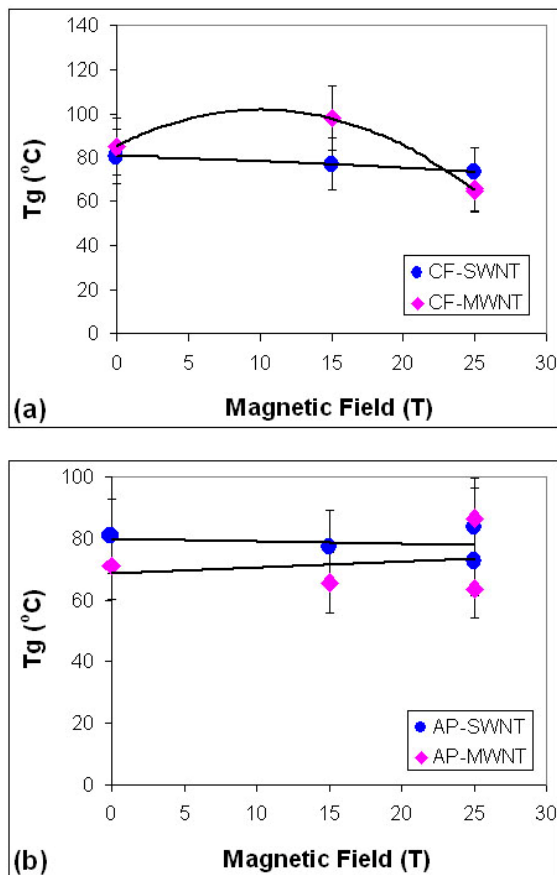


Figure 6.1: The effect of the magnetic field on the glass transition temperature of epoxy matrices reinforced with carbon nanotubes: (a) CF epoxy with both single-wall and multi-wall carbon nanotubes; (b) AP epoxy with both single-wall and multi-wall carbon nanotubes.

The results of the T_g of the CF epoxy composites that were reinforced with both SWCNTs and MWCNTs are summarized in Figure 6.1a. In the CF-SWCNT system, a monotonic decrease in the T_g is observed with increasing external magnetic field strength. In the CF-MWCNT system, the glass transition temperature (T_g) increased as the applied magnetic field increased from 0 to 15 T, but at 25 T, the T_g decreased below that observed with 15 T and below that observed in the absence of an external magnetic field. Hence, the overall dependence of the T_g on the strength of the external magnetic field for both CF-based composites, exhibits a behavior that is contrary to the expected

effect. Several explanations may account for this behavior. (a) The change in polymer chain conformation induced by an external magnetic field may cause not only chain orientation, but also chain alignment and the formation of crystalline regions, resulting in a phase separation and the segregation of the crystalline domains and the amorphous domains. In this case, to compensate for the decrease in entropic energy due to alignment, the chains in the amorphous regions will undergo additional coiling resulting in a lowering of the T_g .^{97, 127, 206-209, 212, 218-229} (b) Under high magnetic field, the presence of carbon nanotubes in the polymer matrix could catalyze chain scission, resulting in a reduction in average chain length, and a decrease in the T_g .²³⁰ (c) If the alignment of the carbon nanotubes in the composite are out-of-phase with the alignment of the polymer chains, a steric barrier to the alignment of the polymer chains could develop, coupled with an enhanced folding of the chains in order to compensate for higher energies associated with the local stresses that occur in this process.^{58, 218, 226, 230, 231} Hence, the polymer chains could become more coiled, causing a decrease of the T_g . The fundamental differences between the effects of 15 T and that of 25 T are still not well understood, because the fundamental processes that are responsible for molecular motion as a function of the presence of an external magnetic field are not yet fully established.

In the case of the AP-epoxy composites, the changes in the T_g as a function of the applied magnetic field are less obvious, as shown in Figure 6.1b. There is an overall small increase in T_g as function of the external magnetic strength, fact that indicates at least a partial alignment of both polymer chains and carbon nanotubes. Both SWCNTs and MWCNT systems exhibit similar behavior. The differences between the behavior of the AP-based systems as compared to the CF-based systems stems most likely from the

difference in their degree of interaction with the carbon nanotubes and their chemical make-up, specifically, the cross-linking molecules in each system, Figure 6.2.

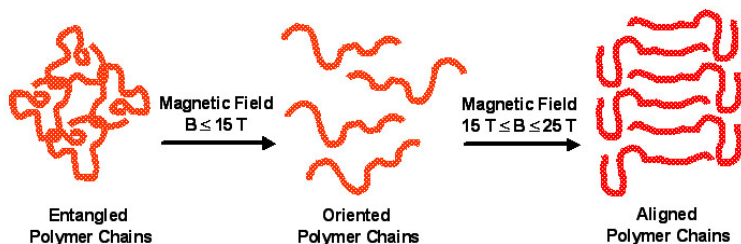


Figure 6.2: The predicted effect of the application of an external magnetic field on the orientation and alignment of polymer chains.

The T_g of the composites was measured by two different techniques: dynamic mechanical analysis and DSC (see experimental section). It is difficult to compare the glass transition temperature from the DMA tests and DSC tests because the heating rates and the underlying physical phenomena that are measured are quite different. The DSC data is a more direct indication of the glass transition and it is consistently lower than the DMA results, but the general change in T_g is the same with both techniques. The results found in this work are consistent with those found in the literature and hence, the differences of the glass transition temperature values are due to the type of instrumentation employed²³².

6.4.2 Effect on Storage and Loss Moduli and Tan Delta

The storage modulus, G' , is a measurement of the elastic energy stored within the sample during deformation, whereas the loss modulus, G'' , is the energy that is the

measurement of dampening, or dissipation of energy (usually as heat) during the deformation of the sample. From these two different moduli, the Young's modulus or complex modulus, may be calculated, as shown in Equation 1.¹⁷⁸

$$\sigma = G^* \varepsilon = \left(\sqrt{(G')^2 + (G'')^2} \right) \varepsilon \quad \tan \delta = \left(\frac{G''}{G'} \right) \quad (\text{eqn 6.1})$$

In this equation, σ represents the stress, ε represents the strain, G^* is Young's modulus, G' is the storage modulus and G'' is the loss modulus. The ratio of the loss modulus to the storage modulus is $\tan \delta$, thus making all three properties inter-related as they are analyzed together in the same experimental set-up. The expected effect of an external magnetic field on the storage modulus is such that with increasing magnetic field and the alignment of the polymer chains and CNTs, the storage modulus should increase as well. The effect of an external magnetic field on the loss modulus is expected to be similar, albeit to a different extent than that expected on the storage modulus.

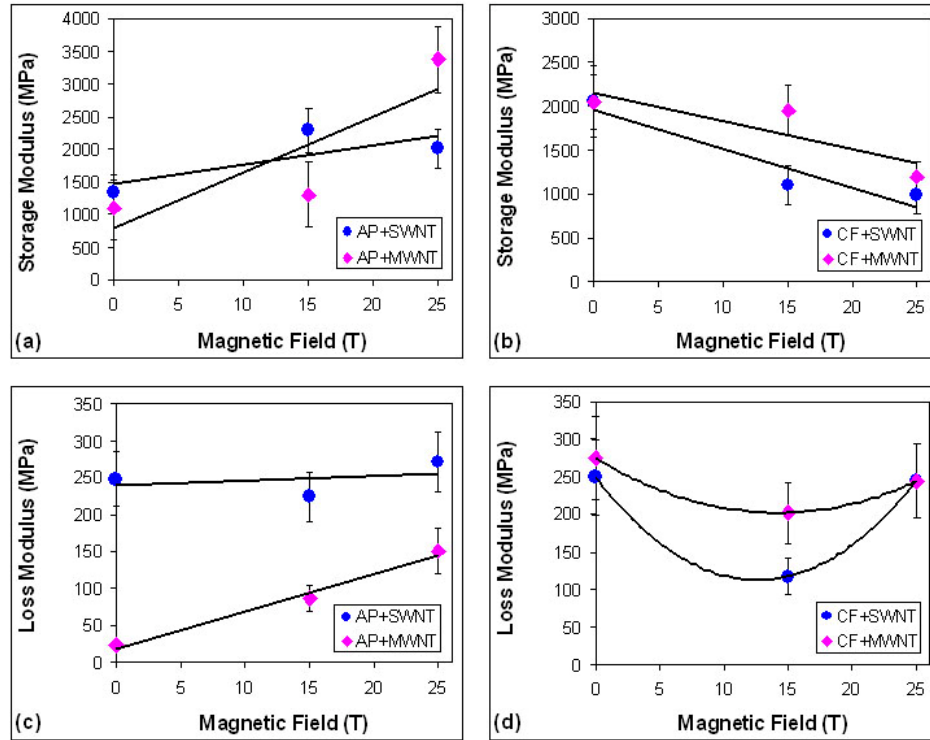


Figure 6.3: The effect of the applied magnetic field on the loss and storage moduli of epoxy matrices reinforced with carbon nanotubes: (a) The loss modulus of CF epoxy reinforced with single-wall and multi-wall carbon nanotubes; (b) The loss modulus of AP epoxy reinforced with single-wall and multi-wall carbon nanotubes; (c) The storage modulus of CF epoxy reinforced with single-wall and multi-wall carbon nanotubes; (d) The storage modulus of AP epoxy reinforced with single-wall and multi-wall carbon nanotubes.

The effect of the magnetic field on the storage modulus is different for both AP and CF epoxy-based systems, as shown in Figure 6.3 (a, b). The AP- MWCNT composite system exhibits an increase in the storage modulus with an increase of the external magnetic field, as expected. The AP-SWCNT composite system behaves in a similar manner, even though the increase in the storage modulus in this case is less pronounced. Given their more rigid structure, MWCNTs coil to a lesser degree and are less prone to aggregation than SWCNTs, and hence, their alignment due to the influence

of the magnetic field may be more uniform than that achieved with SWCNT. The ability of SWCNTs to buckle under stress, coupled with their high degree of entanglement, makes it more difficult for them to stay separated and undergo alignment under the experimental conditions that we have used.^{179-181, 183}

Conversely, in the CF epoxy composites, the storage modulus decreases with the increase in magnetic field. The rate of decrease of the storage modulus for the CF-SWCNT composite appears to be larger with increasing magnetic field as compared to that of the CF-MWCNT composite. This behavior points to an overall “softening” of the composite, and is consistent with the observed decrease in the T_g .

The effects of the magnetic field on the loss modulus for both epoxy-based composite systems, are shown in Figure 6.3 (c, d). The AP- MWCNT composite system exhibits an increase in the loss modulus with an increase of the external magnetic field, as expected. The AP-SWCNT composite system behaves in a similar manner, even though the loss modulus in this case is practically unchanged. This difference in the behavior of the AP-MWCNT and AP-SWCNT may, as before, be attributed to the more rigid nature of the MWCNTs, fact that renders them less conducive to promote energy dissipation within the sample.

In the case of the CF-based system, the loss modulus with both MWCNTs and SWCNTs decreases at 15 T, and then increases at 25 T, contrary to the predicted behavior. Clearly, this unpredicted, non-linear behavior of the loss modulus of the CF-based composites as a function of the applied external magnetic field points to a complex materials behavior. Moreover, given the implications derived from the “softening” effect that these systems exhibited, as indicated by the decrease in their storage modulus, an

actual increase in the loss modulus would have been expected. The decrease in the ability of the CF-based composites to dissipate the stored internal energy indicates the presence of a metastable structure, possibly comprised of both oriented and disordered domains, in which the CNTs are either misaligned, or not necessarily oriented in the direction of the polymer chains. Hence, the dampening mechanism of the critical stresses that may build up upon exposure to an external magnetic field are inhibited in the absence of a co-alignment of polymer chains and CNTs, causing a decrease in the loss modulus [64, 65].

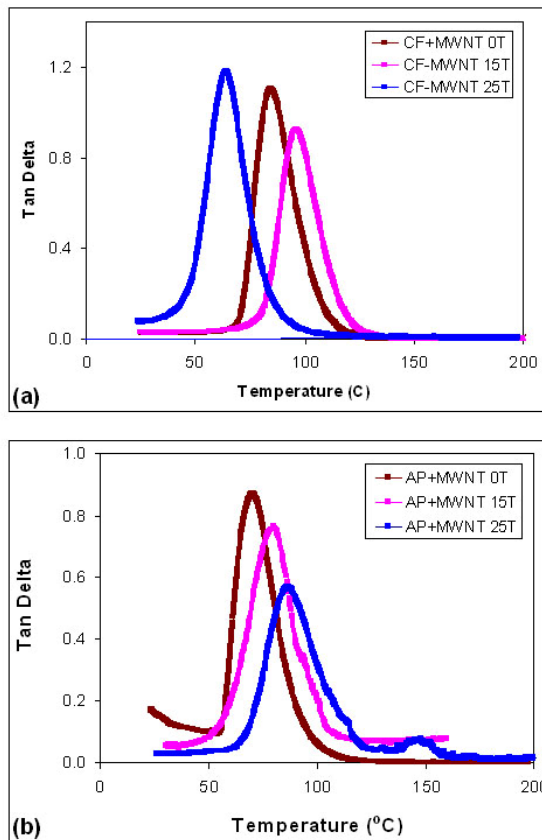


Figure 6.4: The effect of the applied magnetic field on the $\tan \delta$ of epoxy matrices reinforced with carbon nanotubes: (a) CF epoxy reinforced with multi-wall carbon nanotubes exposed to various external magnetic fields; (b) AP epoxy reinforced with multi-wall carbon nanotubes exposed to various external magnetic fields.

The variations of $\tan \delta$ as a function of the magnetic field strength are shown in Figure 6.4. The results obtained for the two polymer systems were not uniform, however, when coupled with prior data, confirm the fact that the two polymer systems exhibit different and complex responses to the applied magnetic field.^{97, 127}

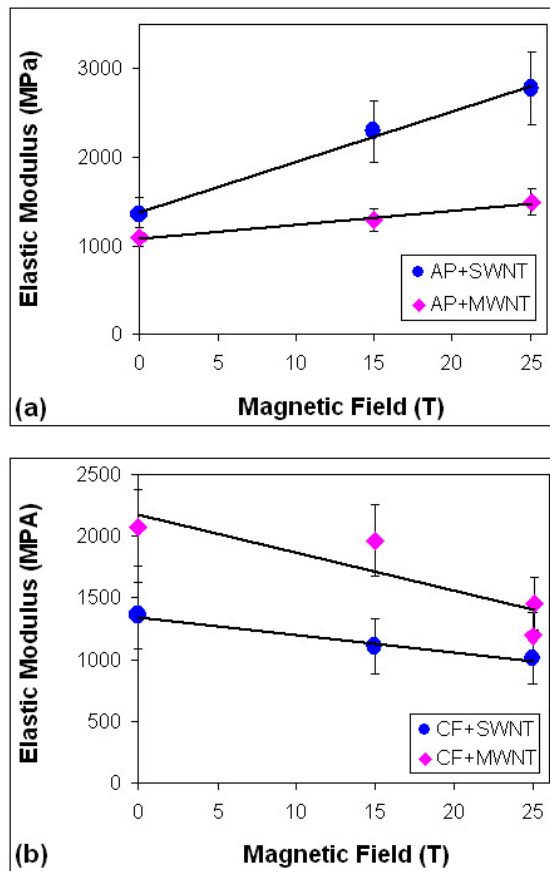


Figure 6.5: The effect of the applied magnetic field on the elastic modulus of epoxy matrices reinforced with carbon nanotubes: (a) AP epoxy with both single-wall and multi-wall carbon nanotubes; (b) CF epoxy with both single-wall and multi-wall carbon nanotubes.

The AP-MWCNT epoxy composite shows a gradual decrease in the $\tan \delta$ peak height with increasing magnetic field and an increase in peak location (shifts right to

higher temperature), as shown in Figure 6.5a. Since $\tan \delta$ is a measure of the relative energy distribution in the sample, i.e. it is the ratio between the dissipated energy and the elastic energy of the system, its values decrease due to the more pronounced increase of the storage modulus as compared to that of the loss modulus as a function of the magnetic field strength. The AP-SWCNT exhibits similar qualitative behavior. Conversely, the CF-MWCNT composite exhibits a decrease in the $\tan \delta$ peak height and increase in peak location (shifts right) when the external magnetic field increases to 15 T. However, at 25 T the $\tan \delta$ peak increases and the location decreases (shifts far left to lower temperature). This behavior is consistent with the previous results for the CF systems, and is due to the complex dependence of their mechanical properties on the applied magnetic field strength.

6.4.3 Effect on Young's Modulus

The Young's moduli of the epoxy-CNT composites were calculated based upon the data collected from the DMA experiments, using Equation 6.1. The Young's moduli of the polymer carbon nanotube composites for the two different epoxy types shown in Figure 6.5 (a,b) were significantly different^{58, 180, 181, 231}. Based on results from previous work using similar epoxy systems^{97, 127}, it is expected that increasing polymer chain and CNT alignment should result in an increase in the modulus of the material. Indeed, the AP-based nanocomposites exhibited the predicted behavior, as shown in Figure 6.5a. Unlike the AP system, in which a gradual increase in modulus is observed with the increase of the external magnetic field, in the CF-based epoxy systems a decrease in the modulus is observed as a function of the external magnetic field, as shown in Figure 6.5b.

While in the AP epoxy system there is considerable evidence of the alignment of both polymer chains and CNTs under an external magnetic field,¹²⁷ the possible alignment and the nature of the resulting morphology in the CF-based systems has not been well characterized.^{180, 183} Clearly, this indicates that alignment of CNTs in an epoxy matrix is intimately dependent on the chemical make-up of the polymer, i.e. the type of core polymer component and, very importantly, the type of cross linking molecules.

6.4.4 Effect on Raman Scattering

The orientation-dependent Raman spectra of SWCNTs and MWCNTs can be determined with different angles between the polarization of the incidence laser light and the nanotube axis using VV (parallel polarization of the incidence and scattered light) configuration. The Raman scattering pattern of a carbon nanotube is unique to the properties of an individual tube. The differences depend on defects, wall thickness, and the conductivity of the carbon nanotubes.^{130, 198, 233, 234} The scattering pattern also changes as a function of the absence or presence of strain on the carbon nanotube. It would make sense that other factors, such as a magnetic field,²³⁵⁻²³⁷ would affect the Raman scattering pattern.

The orientation-dependent Raman spectra of SWCNT can be determined with different angles between the polarization of the incidence laser light and the nanotube axis using VV (parallel polarization of the incidence and scattered light) configuration. The G band which is found around 1591 cm^{-1} , corresponds to the resonantly excited metallic SWCNTs, and shows a maximum intensity when the polarization of the incident radiation is parallel to the nanotube axis (i.e. $\alpha = 90^\circ$), and is minimal when the

polarization of the incident radiation is perpendicular to the nanotube axis (i.e. $\alpha = 0^\circ$).¹³⁰,
143, 200-202

It is expected that an increase in CNTs will be accompanied by an increase in the intensity of the G band. Moreover, there should also be a shift of the G band to higher frequencies for MWCNTs as compared to their SWCNTs MWCNT counterparts. As stated earlier, the G band of the SWCNTs tend to have a peak around 1591 cm^{-1} and the MWCNTs G band tend to be located around 1600 cm^{-1} .^{130, 198, 233-237}

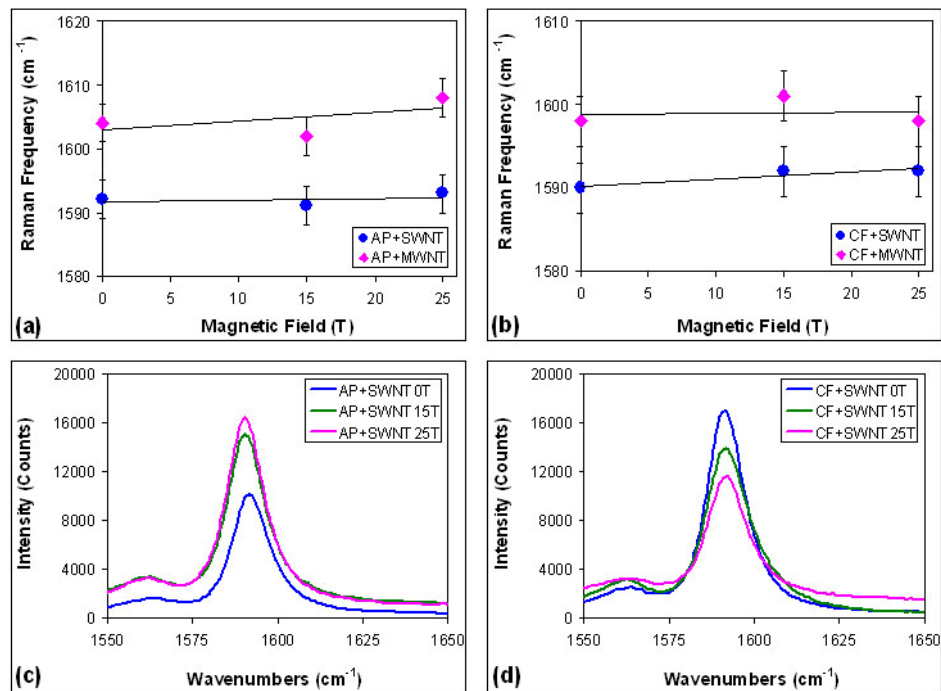


Figure 6.6: The effect of the applied magnetic field on the alignment of the carbon nanotube chains for both types of carbon nanotubes as inferred from the changes of the intensity of their G band in their Raman spectra: (a) AP epoxy reinforced with both single-wall and multi-wall carbon nanotubes; (b) CF epoxy reinforced with both single-wall and multi-wall carbon nanotubes; (c) The Raman spectrum of the AP epoxy matrix reinforced with single-wall carbon nanotubes at different applied magnetic field strengths; (d) The Raman spectrum of the CF epoxy matrix reinforced with single-wall carbon nanotubes at different applied magnetic field strengths.

The data shown in Figure 6.6 (a,b) illustrates the effect of the applied magnetic field on the G band intensity and frequency. It appears that the G band is not only affected by the magnetic field, but by the polymer used as the epoxy matrix, as expected based on the results obtained so far. The graphs in Figure 6.6 (a,b) show that the trend in the change in the frequency of the G band is similar for all the epoxy systems that we have tested in this work, irrespective of the type of carbon nanotubes embedded in them. The G band peak for the AP-based systems shifts from 1604 cm^{-1} for MWCNTs and 1592 cm^{-1} for SWCNTs at 0 T, MWCNTs 1608 cm^{-1} and 1593 cm^{-1} , respectively, at 25 T. The G band for the CF-based systems shifts from 1598 cm^{-1} MWCNTs and 1590 cm^{-1} for SWCNTs at 0 T, to 1598 cm^{-1} and 1592 cm^{-1} , respectively, at 25 T. The shift in the CNTs peak location, while negligible, could be a result of samples having a mixture of both SW/MWCNTs, in addition to inconsistencies within the sample on a microscopic level.

Based on the mechanical properties results, we determined that the AP-based epoxy composite, particularly the one containing SWCNTs, exhibits improved moduli as a function of the applied magnetic field. This effect was attributed to the increased orientation and alignment of the CNTs in the polymer matrix. Conversely, the non-linear response of the storage and loss moduli of the CF-based systems, coupled with the decrease in Young's modulus, point to an effective misalignment of the carbon nanotubes and a complex response in the presence of an external magnetic field. This is further supported by the changes in the intensity of the Raman G band of the CNTs, as shown in Figure 6.6 (c,d). Upon the application of an external magnetic field on the epoxy composites containing SWCNTs, a significant increase in intensity at the characteristic G

band is observed for the AP-based epoxy system (Figure 6.6c), while for the CF-based epoxy system (Figure 6.6d), a small gradual decrease occurs, consistent with the trend observed also with respect to the behavior of its elastic modulus. Additional support for the fact that CNTs in the AP matrix have a higher degree of alignment that in the CF matrix is evident in the TEM images of such systems shown in Figure 6.7 (a,b). The CNTs in the AP system (Figure 6.7a) show alignment in the direction of the applied magnetic field, while the CNTs in the CF system show various regions of local alignment, but not necessarily in the direction of the magnetic field.

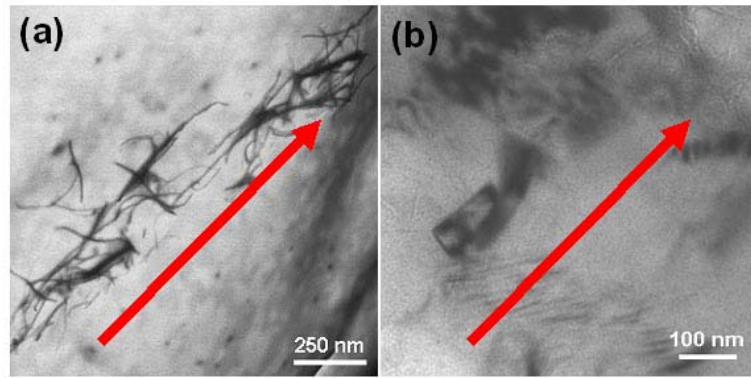


Figure 6.7: TEM images of MWCNTs embedded in epoxy matrices placed under a 17 T magnetic field. (a) AP-based composite, and (b) CF-based composite. (Note that these samples could not be tested for their mechanical properties due to inadequate sample dimensions and hence, it is assumed that these images approximate their respective nanocomposite morphology at 15 T).

6.5 Summary of Mechanical Properties of Magnetic Field Alignment of Carbon

Nanotubes

In this work, we have analyzed the effect of an external magnetic field on carbon nanotube alignment in epoxy-based composites and the implications regarding their mechanical properties. The results comprised in this work, coupled with previous results^{97, 127}, has illustrated that the effect appears to be dependent upon the polymer matrix used

in the composite. The results showed that the carbon nanotubes appear to have an affinity for polymers with amine groups and is not uniform for all epoxy polymers. It was determined that the exposure of the samples to a magnetic field increased the stiffness for the AP system, which we believe is due to increased alignment of the carbon nanotube in the system. The CF epoxy system appeared to have a consistent decrease in properties under the application of a magnetic field, and the original composite at 0 T had better properties than any of the treated ones. The decrease in stiffness upon exposure to a magnetic field in the CF-based system is most likely caused by a decoupled orientation between the polymer chains due to inhibited chain movement caused by the presence of the carbon nanotubes, and formation of a disordered complex microstructure. If compared to the pure epoxy matrices under various magnetic fields, it becomes clear that the incorporation of CNTs has a detrimental effect on the stiffness of composites. As stated earlier, this could be due to the non-conformal alignment of CNTs and polymer chains, which in turn, could be a result of premature network hardening under the magnetic field and the trapping of the CNTs in metastable conformations in the matrix.

CHAPTER 7

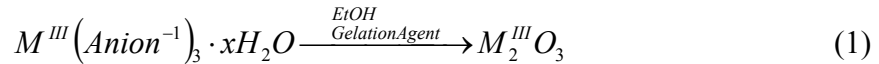
CARBON NANOTUBES DECORATED WITH IRON (III) OXIDE PARTICLES FROM SOL GEL PROCESSING FOR MAGNETIC APPLICATIONS

7.1 Overview

This chapter expands upon the research of Chapter 6. It was found in Chapter 6 that CNTs and self-aligning epoxy couldn't effectively align carbon nanotubes in a magnetic field. In this chapter, the research is focused on adding iron (III) oxide particles to the CNT and epoxy matrix to assist in alignment. This chapter discusses the method of sol-gel processing to create iron (III) oxide particles for decoration of carbon nanotubes. Section 7.2 gives a brief introduction and background of previous research in the areas of nanomaterials, functionalization of carbon nanotubes, and functionalized carbon nanotube polymer composites. Section 7.3 details the experimental procedure used to produce nanoparticles for decorating the carbon nanotubes. Section 7.4 describes the results of the different methods for producing nanoparticles. In conclusion, Section 7.5 summarizes the results and determines which system would be idea to use with carbon nanotube composites. Chapter 8 continues the research by utilizing the nanoparticles synthesis method presented in this chapter.

7.2 Introduction

There are currently several different methods for creating iron oxide nanoparticles such as, sol gel processing, synthesis using microemulsions, hydrothermal synthesis, and high temperature reactions in solution.²³⁸⁻²⁴⁶ All the above-mentioned methods, with the exception of the sol-gel synthesis, constitute reliable and controllable methods for the formation of iron oxide nanoparticles, however, they require high temperature, high pressure and/or hazardous environments, which can be difficult and costly to produce in bulk.^{239, 246-248} Conversely, sol-gel synthesis does provide an extremely easy method of creating a large variety of metal oxides from metals salts, at low temperatures and ambient conditions. The reaction proceeds via the following pathway:



The process involves the scavenging of protons from the aqueous coordination sphere of the metal salt (sol formation), followed by condensation and formation of the metal oxide product characterized by a three-dimensional network.^{239, 246} The formation of a metal oxide 3D network may not be conducive to the development of materials where the presence of separated, individual, functionalized nanoparticles is essential, such as in magnetic or medical applications.^{191, 247-250} Hence, the ability to create independent nanosized particles, with tunable size and surface properties, via a method that combines the efficiency and advantages of the sol-gel process, but inhibits the formation of a gel, becomes a very important endeavor.

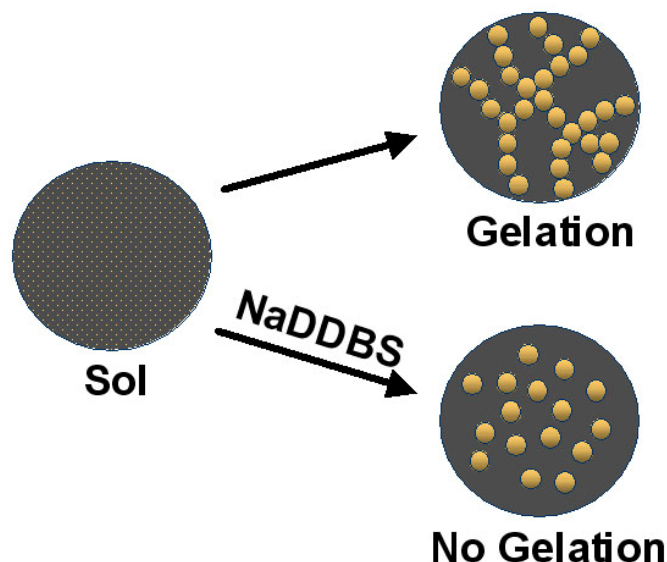


Figure 7.1: Schematic representation of the modified sol-gel process involving the use of a surfactant, NaDDBS. In the absence of NaDDBS, the system undergoes gelation (top process), while in the presence of NaDDBS the system either does not gel or gelation is delayed (bottom process), but the particles formed are of similar size as the primary particles in the systems formed by the regular sol-gel method.

In this research, we have applied a modified sol gel processing method to create iron (III) oxide nanoparticles in a manner that would utilize the advantages of the traditional sol-gel process, but circumvent the pitfalls of network formation. Our strategy was the addition of a common surfactant, sodium dodecyl benzene sulfonate (NaDDBS), to the reaction mixture, at different stages of the reaction, in order to provide an adequate stabilization mechanism for the growing iron oxide nanoparticles, and arrest their growth and the network formation at the optimal step, as shown in the process schematics in Figure 7.1. Probing the effect of the NaDDBS molecules on the iron oxide nanonetwork formation when introduced into the reaction solution at different stages, will provide insight into the nucleation and aggregation of the fundamental particles and will offer opportunity for process optimization without gelation.

7.3 Experimental Procedure

The syntheses were performed in 20 mL glass scintillation vials under ambient conditions. Six separate solutions were made in order to test the effects of the surfactant on the final iron oxide particle size.

For the synthesis with $\text{Fe}(\text{NO}_3)_3 \cdot 9\text{H}_2\text{O}$ (solution 6), 0.65 g $\text{Fe}(\text{NO}_3)_3 \cdot 9\text{H}_2\text{O}$ was added to 3.5 mL of ethanol and stirred until the $\text{Fe}(\text{NO}_3)_3 \cdot 9\text{H}_2\text{O}$ dissolved completely. Then, 1.2 mL of propylene oxide was added as the gelation agent. Solutions 2 and 4 were prepared following the same procedure as that of solution 6, but with the addition of 3.5 mL of 1.2 mM NaDDBS before the addition of propylene oxide. For the synthesis with $\text{FeCl}_3 \cdot 6\text{H}_2\text{O}$, (solution 5), 0.42 g $\text{FeCl}_3 \cdot 6\text{H}_2\text{O}$ was added to 3.5 mL of ethanol and stirred until the $\text{FeCl}_3 \cdot 6\text{H}_2\text{O}$ dissolved completely. Then, 1.2 mL of propylene oxide was added. Solutions 1 and 3 were prepared following the same procedure as that of solution 5, but with the addition of 3.5 mL of 1.2 mM NaDDBS before the addition of propylene oxide. All solutions were then placed in a Fisher Scientific isotherm oven to dry for 72 hours at 100°C. After this time, water was added to solutions 3, 4, 5, and 6, and 1.2 mM NaDDBS was added to solutions 1 and 2, as summarized in Table 7.1.

Table 7.1: Summary of the characteristics of the modified sol-gel process for the various reactions performed in this study. Specific molar quantities for each reactant are described in the Experimental section.

Sample Number	Metal Salt Precursor	Gelation Agent	NaDDBS Addition	Water Addition
1	$\text{FeCl}_3 \cdot 6\text{H}_2\text{O}$	$\text{C}_3\text{H}_6\text{O}$	Before gel process and after drying	None
2	$\text{Fe}(\text{NO}_3)_3 \cdot 9\text{H}_2\text{O}$	$\text{C}_3\text{H}_6\text{O}$	Before gel process and after drying	none
3	$\text{FeCl}_3 \cdot 6\text{H}_2\text{O}$	$\text{C}_3\text{H}_6\text{O}$	Before gel process	After drying
4	$\text{Fe}(\text{NO}_3)_3 \cdot 9\text{H}_2\text{O}$	$\text{C}_3\text{H}_6\text{O}$	Before gel process	After drying
5	$\text{FeCl}_3 \cdot 6\text{H}_2\text{O}$	$\text{C}_3\text{H}_6\text{O}$	None	After drying
6	$\text{Fe}(\text{NO}_3)_3 \cdot 9\text{H}_2\text{O}$	$\text{C}_3\text{H}_6\text{O}$	None	After drying

All the solutions were placed in a sonic dismembrator (Fisher Scientific, 20 kHz) at 35 % amplification for 30 minutes. After sonication, transmission electron microscopy (TEM) samples of both solutions were measured to determine particle size. TEM samples were prepared by placing a droplet of solution onto a TEM grid and allowing it to dry for later analysis. These samples were then analyzed using the Hitachi HF2000, 200 kV transmission electron microscope.

X-ray diffraction (XRD) was performed on the samples in order to determine composition. The samples were prepared and tested in the same manner as previous

research.²⁵¹ The dried samples were then placed on a zero background holder and analyzed using a Philips PW 1800 X-ray diffractometer. Patterns from 20° to 90° were examined with a step size of 0.02° using monochromatic $\text{Cu}_{K\alpha}$ X-rays with a wavelength of 1.54 Å.

7.4. Results and Discussion of Iron (III) Oxide Decorated Carbon Nanotubes

7.4.1. Modified Sol Gel Processing of Iron (III) Oxide Particles

The main outcome of this research was fact that the presence of a typical surfactant, NaDDBS, was able to modify the morphology of iron oxide particles formed by sol gel processing. Propylene oxide was used as a gelation agent because it is known that this compound facilitates the formation of a monolithic wet gel in about just a few minutes.^{252, 253} The addition of water to the reaction solution is known to alter the gel time as a function of the metal salt used as precursor.²⁵³ The two metal salts used in this research, ferric nitrate nonahydrate, $\text{Fe}(\text{NO}_3)_3 \cdot 9\text{H}_2\text{O}$ and ferric chlorate hexahydrate, $\text{FeCl}_3 \cdot 6\text{H}_2\text{O}$, were known to form a gel under these reaction conditions²⁵²⁻²⁵⁴, and since the sol-gel reactions in these systems are well characterized, they represented good starting points for probing the outcome of the modified procedure.

The addition of the NaDDBS increased the gelation time for the $\text{FeCl}_3 \cdot 6\text{H}_2\text{O}$ from 2 minutes to several hours, and prevented $\text{Fe}(\text{NO}_3)_3 \cdot 9\text{H}_2\text{O}$ from forming a gel altogether. The different response of the two systems was not completely unexpected, because it was determined previously by Gash *et al.*²⁵³ that it is possible to form a gel in water with $\text{FeCl}_3 \cdot 6\text{H}_2\text{O}$ but not with $\text{Fe}(\text{NO}_3)_3 \cdot 9\text{H}_2\text{O}$. One reason for this phenomenon, i.e. the delay in the onset of gelation, might be the relative molar quantities of the

components in the reaction medium, i.e. water, propylene oxide and the iron salt precursor. Since the NaDDBS molecules were added before the addition of propylene oxide and in the presence of excess water, they could have, most likely, clustered around the iron (III) centers and formed a loose self-assembled layer around the hydrated iron moiety. This, in turn, could have been capable, in principle, to prevent the approach of the propylene oxide molecules within the coordination sphere of the iron (III) centers, and as a consequence, the formation of a gel, as shown in Figure 7.2.

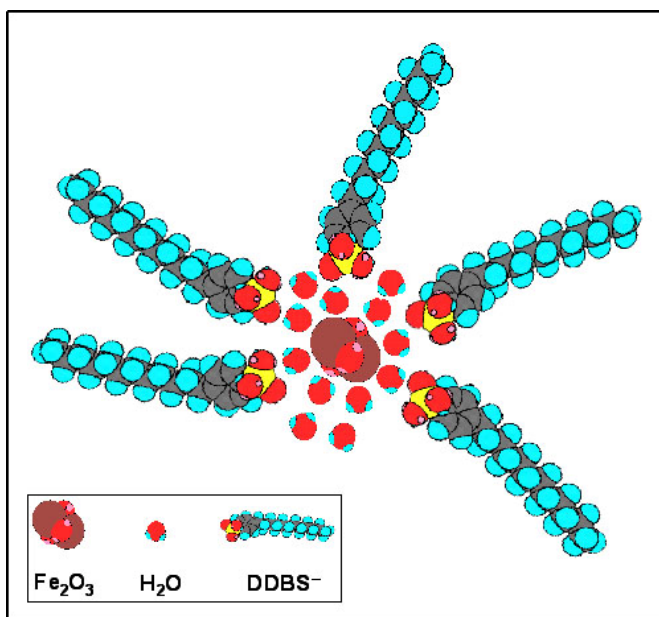
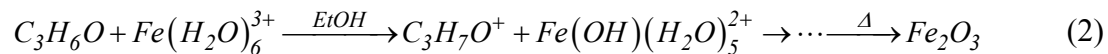


Figure 7.2: Schematic representation of the hydration sphere around the iron (III)/iron oxide centers coupled with the preferred location of the NaDDBS surfactant molecules.

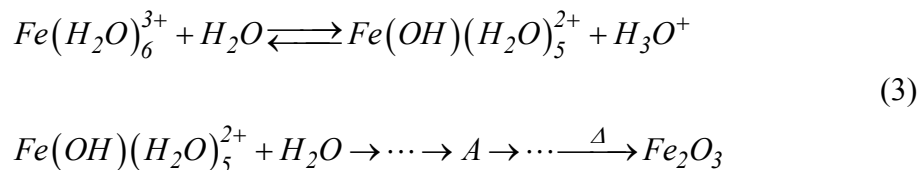
The structure depicted shows the steric and electrostatic barrier that the NaDDBS molecules create around the iron (III) centers, which inhibits the formation of a gel. The 3D schematic was achieved by the use of the commercial software ChemDraw 3D

Solutions that underwent gelation followed the same general procedure of hydrolysis, condensation, and heating. This process allows for the formation of iron (III) oxide particles through a series of reactions, involving an intermediate reaction product

having a metal hydroxide reactive group (*A*). In the presence of polypropylene oxide the reaction is as follows:



In the presence of water the reaction is as follows:



It is expected that the presence of NaDDBS would be essential in the early stages of the process, impeding the reaction with the epoxide and/or hydroxo ligands, thus preventing the gelation process. In the last step of this process, the material is heated to 100°C in order to remove all excess water and promote the formation of the iron (III) oxide.

Table 7.2: Summary of the iron oxide product size and morphology resulting from the modified sol-gel process for the various reactions performed in this study.

Sample Number	Metal Salt Precursor	Gel Formation	Average Particle Size (nm)	Sample Color
1	$\text{FeCl}_3 \cdot 6\text{H}_2\text{O}$	Yes	4.9	Brown
2	$\text{Fe}(\text{NO}_3)_3 \cdot 9\text{H}_2\text{O}$	No	3.2	Light brown
3	$\text{FeCl}_3 \cdot 6\text{H}_2\text{O}$	Yes	84.6	Orange
4	$\text{Fe}(\text{NO}_3)_3 \cdot 9\text{H}_2\text{O}$	No	5.1	Light brown
5	$\text{FeCl}_3 \cdot 6\text{H}_2\text{O}$	Yes	3.6	Brown
6	$\text{Fe}(\text{NO}_3)_3 \cdot 9\text{H}_2\text{O}$	Yes	4.5	Light Brown

The change in particle size and color of the solutions is illustrated in Table 7.2. It appears that the color of the solution is directly related to the size of the particles formed in the corresponding solution, as shown in Figure 7.3. The average particle size was determined by measuring the individual particle sizes using high-resolution TEM images for each sample. The images and corresponding histograms are shown in Figures 7.4 and 7.5. It was difficult to obtain high quality TEM images from the collected samples due to

the low degree of aggregation (i.e. low mass) of the iron oxide particles and the presence of surfactant and epoxide molecules, which tend to cloud the images.



Figure 7.3: Pictures of the six different iron oxide samples obtained via the modified sol-gel process. The characteristics of the specific reactions in each solution are summarized in Table 7.1. Note the bright orange color of sample 3 as compared to the brown color of all other samples.

The addition of NaDDBS prior to gelation to the $\text{FeCl}_3 \cdot 6\text{H}_2\text{O}$ system did not appear to have a large effect on the particle sizes compared to the same system in the absence of NaDDBS. However, upon drying, the system having NaDDBS that was added in the final stages of the synthesis (solution 1) appears to generate significantly smaller particle size than that of the system without NaDDBS added at this stage (solution 3). This leads to the conclusion that the action of the NaDDBS molecules is most notable in the growth stage of particles (gel phase) rather than the nucleation stage (sol phase). This may be due to the fact that the surfactant molecules inhibit the growth of the particle by replacing water molecules in the coordination sphere of the growing oxide particles, thus preventing their aggregation.

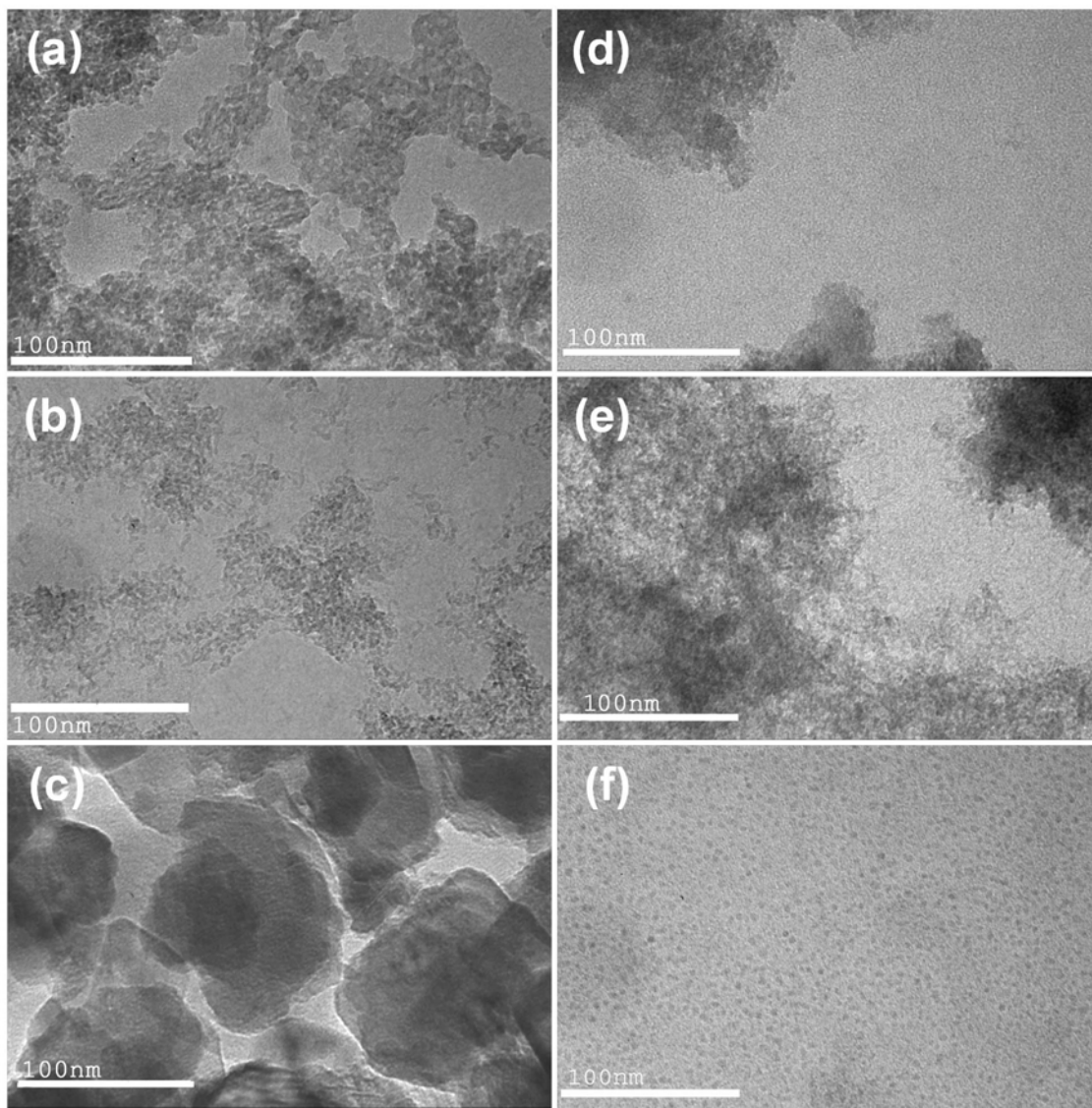


Figure 7.4: High resolution transmission electron microscopy (HRTEM) images of the iron oxide products obtained from the various reactions performed as per the specifications summarized in Table 1: (a) $\text{FeCl}_3 \cdot 6\text{H}_2\text{O}$ precursor with NaDDBS added prior to the gelation process and upon drying (sample 1); (b) $\text{Fe}(\text{NO}_3)_3 \cdot 9\text{H}_2\text{O}$ precursor with NaDDBS added prior to the gelation process and upon drying (sample 2); (c) $\text{FeCl}_3 \cdot 6\text{H}_2\text{O}$ precursor with NaDDBS added prior to the gelation process (sample 3); (d) $\text{Fe}(\text{NO}_3)_3 \cdot 9\text{H}_2\text{O}$ precursor with NaDDBS added prior to the gelation process; (e) $\text{FeCl}_3 \cdot 6\text{H}_2\text{O}$ precursor without NaDDBS (sample 5); (f) $\text{Fe}(\text{NO}_3)_3 \cdot 9\text{H}_2\text{O}$ precursor without NaDDBS (sample 6).

As for the $\text{Fe}(\text{NO}_3)_3 \cdot 9\text{H}_2\text{O}$ systems, the changes in particle size are negligible in most samples, however, the smallest particle sizes were obtained in the solutions

containing NaDDBS. This supports the realization that the addition of NaDDBS to these systems interferes in the growth stage of the iron oxide nanoparticles and not only inhibits the formation of a gel, but also limits the extent of aggregation, thus decreasing the size of the fundamental particles.

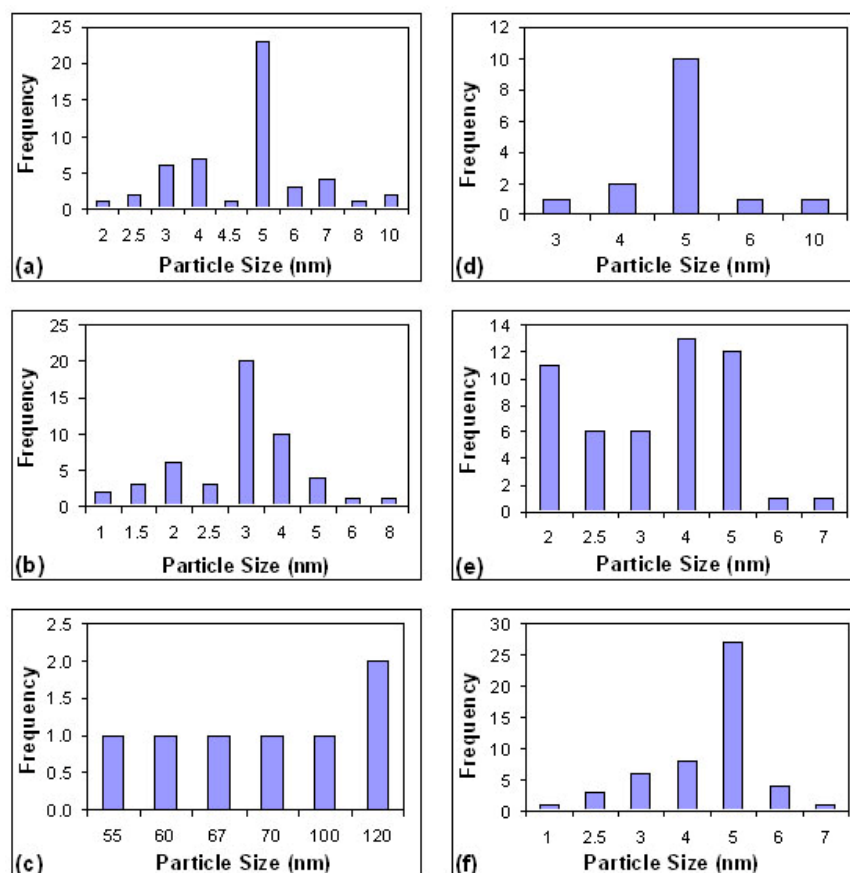


Figure 7.5: Particle size distribution for the iron oxide nanoparticles obtained in the various samples, and based on the HRTEM images shown in Figure 4: (a) FeCl₃·6H₂O precursor with NaDDBS added prior to the gelation process and upon drying (sample 1); (b) Fe(NO₃)₃·9H₂O precursor with NaDDBS added prior to the gelation process and upon drying (sample 2); (c) FeCl₃·6H₂O precursor with NaDDBS added prior to the gelation process (sample 3); (d) Fe(NO₃)₃·9H₂O precursor with NaDDBS added prior to the gelation process; (e) FeCl₃·6H₂O precursor without NaDDBS (sample 5); (f) Fe(NO₃)₃·9H₂O precursor without NaDDBS (sample 6).

The coupling of a high number of coordinated water molecules with the presence of a surfactant, inhibits gel formation on one hand, and stabilizes small nanoparticles on the

other hand. Hence, a distribution of particle sizes in the 3-5 nm range that is characteristic to the primary particles formed by the sol-gel process,^{245, 251, 253} may be achieved also in a system in which surfactants are present and the gelation is inhibited.

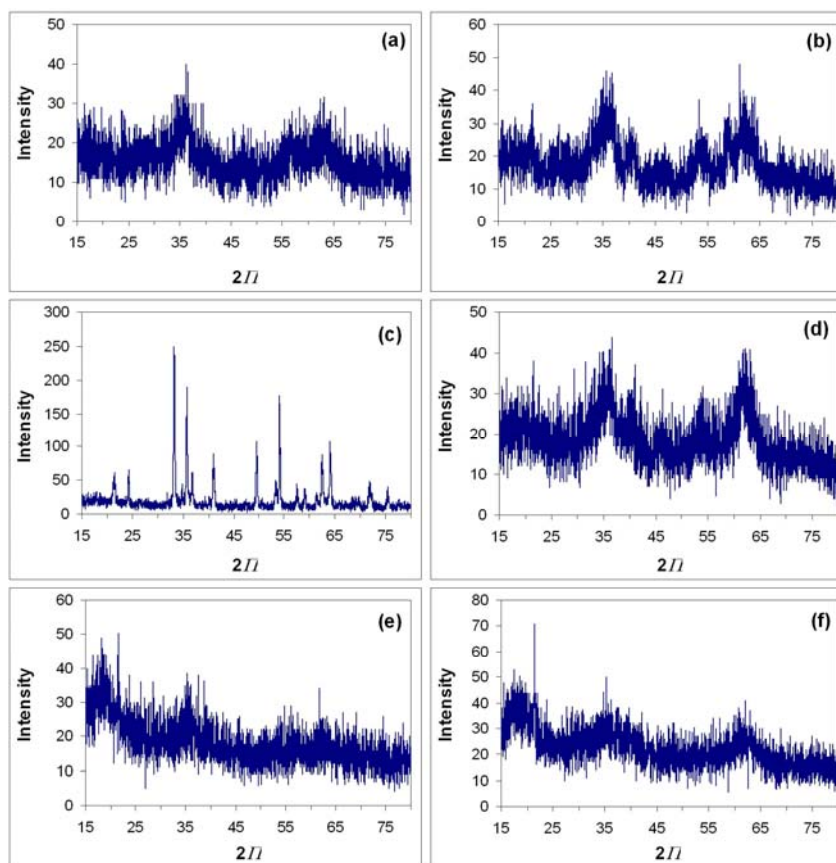


Figure 7.6: Experimental X-ray diffraction patterns for the iron oxide nanoparticles obtained in the various samples summarized in Table 1: (a) $\text{FeCl}_3 \cdot 6\text{H}_2\text{O}$ precursor with NaDDBS added prior to the gelation process and upon drying (sample 1); (b) $\text{Fe}(\text{NO}_3)_3 \cdot 9\text{H}_2\text{O}$ precursor with NaDDBS added prior to the gelation process and upon drying (sample 2); (c) $\text{FeCl}_3 \cdot 6\text{H}_2\text{O}$ precursor with NaDDBS added prior to the gelation process (sample 3); (d) $\text{Fe}(\text{NO}_3)_3 \cdot 9\text{H}_2\text{O}$ precursor with NaDDBS added prior to the gelation process; (e) $\text{FeCl}_3 \cdot 6\text{H}_2\text{O}$ precursor without NaDDBS (sample 5); (f) $\text{Fe}(\text{NO}_3)_3 \cdot 9\text{H}_2\text{O}$ precursor without NaDDBS (sample 6).

X-ray diffractions of the iron oxide nanoparticles are shown in Figure 7.6 for the as-synthesized samples. The diffraction patterns for samples 1, 2, 4, 5 and 6 are largely amorphous in character, having large diffraction peaks resulting from the nanoscale

features of the material. Figure 7.7 illustrates possible alternative phases that may have formed; iron (III) oxide, hydroxide and oxyhydroxide phases: α -Fe₂O₃ (hematite), Fe(OH)₃, α -FeO(OH) (ferrihydrite), γ -Fe₂O₃, γ -FeO(OH); and δ -FeO(OH). Since the samples are largely amorphous, the analysis is mainly qualitative. The broad peaks that can be seen in the diffraction patterns largely overlap with all of the main peaks in most of the spectra shown in Figure 7.7.

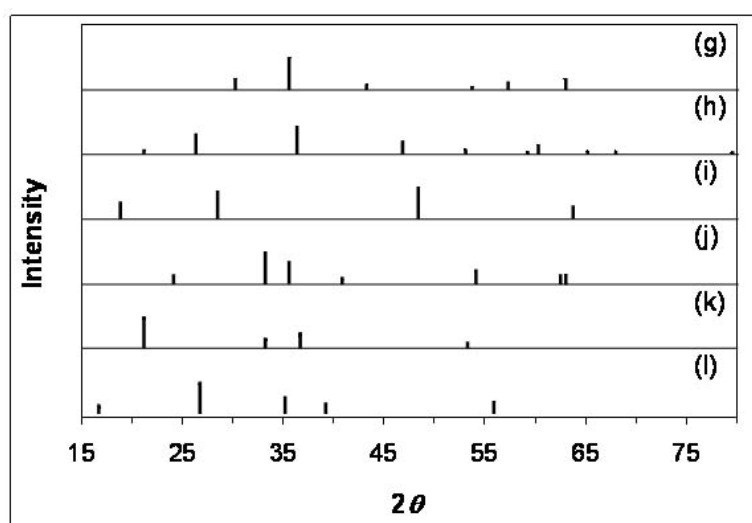


Figure 7.7: Theoretical X-ray diffraction patterns for various iron oxide/oxyhydroxide phases: (a) α -Fe₂O₃ (hematite); (b) Fe(OH)₃; (c) α -FeO(OH) (ferrihydrite); (d) γ -Fe₂O₃; (e) γ -FeO(OH); and (f) δ -FeO(OH).

In samples 5 and 6 it appears that there is an additional peak at low angles, but this could be due to beam noise while the samples were analyzed. In contrast, the XRD analysis of sample 3, shown in Figure 7.6c, exhibited a diffraction pattern that is characteristic of a crystalline material. The crystalline character of this spectrum is commensurate with the average particles size of 80 nm calculated from TEM images. This sample, like the others tested, exhibits peaks that correspond to a variety of iron oxide compounds, as mentioned above. Based on this analysis, we cannot ascertain that the particles formed

consist of Fe_2O_3 exclusively. The XRD data confirms that the particles are mostly nanocrystalline (except sample 3) iron oxide particles, similar to the results obtained from TEM imaging. In related previous studies,²⁵¹ it was determined that the material could be assigned an empirical formula of $\text{Fe}^{(\text{III})}_x\text{O}_y\text{H}_z$, but nevertheless, throughout this paper, it will be referred to as “iron oxide.” This leads to the conclusion that iron oxide particles may be present along with other oxyhydroxide phases.^{249, 250}

7.4.2 Decoration of CNTs with Iron (III) Oxide Nanoparticles

The decoration of carbon nanotubes with iron oxide particles is shown in Figure 7.8 (a-d). Figure 7.8a is at a relatively low magnification, but the CNT-NaDDBS-iron oxide bundles are clearly visible, and exhibit bundle sizes between 15-40 nm. Hence, these are not individually dispersed nanotubes, but the bundle sizes obtained indicate the aggregation of approximately 10-20 CNT/bundle. Figure 7.8b captures one CNT-NaDDBS-iron oxide bundle having varying diameters. At its widest region, the diameter of the decorated CNT is approximately 45 nm, with the fundamental bundle itself representing about half the diameter, or ~20 nm. Figure 7.8c shows a wider frame in order to capture a larger CNT population, but the results are very similar to those in Figure 1a, i.e. the decorated bundle sizes are approximately 10-30 nm, with fundamental CNT bundles being smaller and on the order of 10-20 nm. Figure 7.8d illustrates a high-resolution image of an agglomeration of iron oxide particles with interdispersed, decorated CNT bundles. From Figure 7.8d an approximate particle size of the iron oxide was determined to be 4 nm. Since there is such a large amount of iron oxide particles in the TEM image the CNT bundles can be seen in the areas indicated by arrows. The

bundles indicated are the most prominent bundles but are not the only bundles in this image.

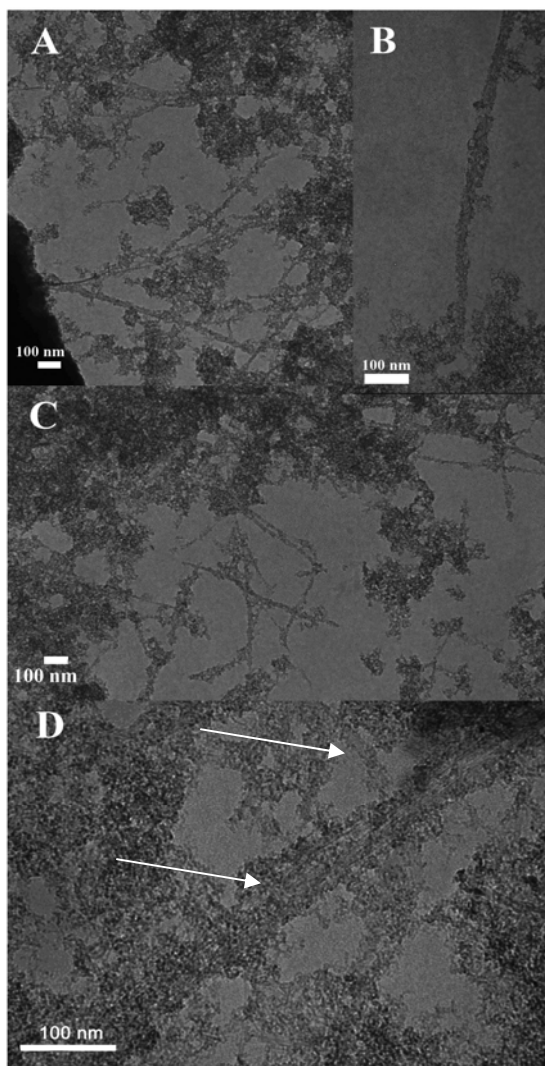


Figure 7.8: Carbon nanotubes decorated with iron oxide particles with various CNT-NaDDBS-Iron oxide bundle sizes (a) 15-40 nm (b) 45 nm (c) 10-20 nm (d) 4 nm iron oxide particles with ~45 nm bundle sizes

The TEM images shown in Figure 7.8 clearly demonstrate the ability to create CNTs decorated with iron oxide nanoparticles.²⁵⁵ This illustrates an easy and economical method for creating CNT-NaDDBS-iron oxide bundles for magnetic applications.²⁵⁵

7.5 Summary of Decorating Carbon Nanotubes with Iron (III) Oxide Nanoparticles

In this work we have shown that the addition of an anionic surfactant to the iron oxide sol-gel processing method decreased the surface energy of the fundamental iron oxide particles and allowed the creation of stable nanosized iron oxide particles without the formation of a 3D network (gel). The primary particle sizes in both systems, $\text{Fe}(\text{NO}_3)_3 \cdot 9\text{H}_2\text{O}$ and $\text{FeCl}_3 \cdot 6\text{H}_2\text{O}$, have nanoscale dimensions in the gel phase regardless of the presence of NaDDBS. The addition of NaDDBS to the $\text{FeCl}_3 \cdot 6\text{H}_2\text{O}$ system in the nucleation stage, i.e. prior to gelation, delayed the gelation process and allowed extensive aggregation to occur. The addition of NaDDBS to the $\text{FeCl}_3 \cdot 6\text{H}_2\text{O}$ system both prior and during gelation, delayed the onset of gelation and resulted in small particles. Similarly, the addition of NaDDBS to the $\text{Fe}(\text{NO}_3)_3 \cdot 9\text{H}_2\text{O}$ system prevented the formation of a gel to occur, but still lead to the formation of nanosize particles in the same size range of the primary particles obtained upon gel formation.

Despite the fact that a mixture of iron oxide compounds is formed by this modified sol-gel method, it still provides an easy and economical synthesis process for the formation of nanoscale iron (III) oxide particles upon the addition of NaDDBS as a surfactant.

The addition of the iron oxide particles from the $\text{Fe}(\text{NO}_3)_3 \cdot 9\text{H}_2\text{O}$ system (solution 2) was demonstrated to result in the decoration of the carbon nanotubes for magnetic applications.

CHAPTER 8

MAGNETIC ALIGNMENT OF IRON (III) OXIDE DECORATED CARBON NANOTUBE POLYMER COMPOSITES

8.1 Overview

In this chapter, a magnetic field was used to align carbon nanotubes in an epoxy and the properties of the resulting composites were explored. Section 8.2 gives a brief introduction and background of previous research done on magnetic field effects on polymers and polymer carbon nanotube composites. Section 8.3 details the experimental procedure used to align the carbon nanotubes. Section 8.4 describes the results of the composites that were placed in a magnetic field. In conclusion, Section 8.5 summarizes the alignment results of the two systems. The next chapters will outline the overall conclusions and recommendations from the research presented.

8.2 Introduction

In this work we have developed a new way of magnetically aligning the carbon nanotubes to allow complete alignment of the composite sample as the sample was being processed, thus avoiding the pitfalls of the other methods. Since carbon nanotubes are not magnetic, they do not align on their own in a magnetic field without the cooperative influence of other aligning fibrous networks (such as a polymer matrix),^{134, 136} or without tethering to them a magnetic material.¹³⁴ Thus, the focus of this work is to tether iron

oxide nanoparticles to the carbon nanotubes in order to induce their alignment while embedded in a polymer matrix.

8.3 Experimental Procedure

The composites were made with Araldite GY 6008, a clear liquid resin with a viscosity of 6,500-10,500 cps at room temperature. According to the manufacturer's specification (Huntsman Advanced Materials Americas Inc.), the resin is a Bisphenol A Diglycidyl ether. The hardener used was ANCAMINE AEP curing agent (Air products), and is an aminoethyl piperazine, 1-(2-, (AEP), a colorless liquid.

For the synthesis of the a single iron oxide nanoparticle batch, 0.65 g $\text{Fe}(\text{NO}_3)_3 \cdot 9\text{H}_2\text{O}$ was added to 3.5 mL of ethanol and 3.5 mL of 1.2 mM NaDDBS, and stirred until the $\text{Fe}(\text{NO}_3)_3 \cdot 9\text{H}_2\text{O}$ dissolved completely. Then, 1.2 mL of propylene oxide was added as the gelation agent. The characterization of the iron oxide nanoparticles formed by this method is shown in Figure 8.1 (a-c).²⁵⁵ Electron micrographs of the NaDDBS-stabilized iron oxide nanoparticles show uniform particle morphology (Figure 8.1a) and narrow particle size distribution (Figure 8.1b). The chemical structure of the particles is obtained by XRD, which identifies the presence of $\gamma\text{-Fe}_2\text{O}_3$ (Figure 8.1c). A detailed account of the procedure to obtain such narrowly-dispersed iron oxide nanoparticles in an aqueous medium has been described elsewhere.²⁵⁵ Two different concentrations of iron oxide nanoparticles were used: a single synthesized batch and a double synthesized batch. The solutions were then placed in a Fisher Scientific Isotemp oven to dry for 72 hours at 100°C. The dried iron oxide batches were then added to the carbon nanotubes. The amount of carbon nanotubes in the suspension was determined based on the final composite weight of 10 g. Solutions were made with 0, 0.5, or 1.0 wt.% carbon

nanotubes. The carbon nanotubes were then dispersed in the same procedure as described previously¹⁹⁸ in the presence of the iron oxide powder. This also leads to the dispersion and stabilization of the iron oxide particles. This solution was then added to the resin, and the excess water was evaporated off. The hardener was added to the resin/CNT/iron oxide mixture, and the mixture was poured into Teflon molds and placed in a magnetic field. The samples were heated to 100°C for several hours and allowed to harden in the 0.0 (no magnetic field), 0.4, and 0.8 Tesla magnetic fields. The composition of the various samples is summarized in Table 1.

Table 8.1: Summary of the sample parameters, such as carbon nanotube content, iron oxide batches, and magnetic field applied.

Sample number	CNT (wt %)	Fe₂O₃ batches	Magnetic field (Tesla)
1 (Epoxy only)	0.0	0	0
2	0.5	1x	0
3	1.0	1x	0
4	0.0	0	0.4
5	0.5	1x	0.4
6	0.5	2x	0.4
7	0.5	2x	0.4
8	1.0	1x	0.4
9	1.0	2x	0.4
10	1.0	2x	0.4
11	0.0	0	0.8
12	0.5	1x	0.8
13	0.5	2x	0.8
14	1.0	1x	0.8
15	1.0	2x	0.8
16	1.0	2x	0.8
17 (Epoxy & NaDDBS)	0.0	0	0

The samples were tested using a MTS Insight 2 the samples were tested in compression using the 643 compression platens to determine the effects of the magnetic field. The samples were tested at 25 °C and 100 °C to obtain information below and above the glass transition temperature. The sample geometry (4 mm squares) used was

not an ideal geometry¹⁴⁹ but was made to ensure consistent data for testing in both aligned and unaligned directions. The data collected was then analyzed and graphed to determine the elastic modulus, yield point and other trends within the data

Raman spectroscopy was used in order to determine the presence and extent of the alignment of the carbon nanotubes in the epoxy matrix as a result of the application of the magnetic field. The samples were tested on a Holo Probe VPT system, with integrated fiber coupled with a Raman system (Kaiser Optical Systems, Inc.), using a 731 nm incident laser radiation and VV (parallel/parallel) configuration.³⁴⁻³⁷ To ensure that the data was accurate, the samples were tested on a flat surface, and the testing site for each angle remained the same. The samples were oriented in the sample compartment so that the highest band intensity will occur at 90°. Subsequently, the samples were tested at various polarization angles ranging from 0° to 90° in order to determine the development of CNT orientation after being subjected to a magnetic field.

The samples were tested in a TA Instruments Q100 differential scanning calorimeter to determine the glass transition temperature of the samples. The samples were tested from 0°C to 200 °C, and a TA universal analysis program was used to calculate the glass transition temperatures.

8.4. Results and Discussion of Iron (III) Oxide Decorated Aligned Carbon

Nanotubes Alignment

The first step was to demonstrate the decoration of the carbon nanotubes by iron (III) oxide particles. This was proven in Chapter 7. The second step was to compare the results of the various measurements of these samples as a function of the strength of the

applied magnetic field, the carbon nanotube content, and iron oxide content and evaluate the effect of these variables on the mechanical properties of the resulting polymer composites.

8.4.1. Effect on Glass Transition Temperature

The initial goal of using a magnetic field on carbon nanotube composites was to promote the directional alignment of the carbon nanotubes, which would improve the mechanical properties of the composite. The effects on the glass transition temperature should be relatively simple to predict since they are well documented.³⁸⁻⁴² It is expected that increasing the extent of alignment and orientation of the carbon nanotubes and epoxy matrix chains¹²⁷ will result in an increase in the glass transition temperature of the composite.^{23,38-42} Table 8.2 summarizes the T_g values for the various samples tested.

Table 8.2: Summary of the measured and determined sample properties, such as glass transition temperature, carbon nanotube content, iron oxide batches, applied magnetic field, and Raman analysis.

Sample number	T_g (°C)	CNT (wt%)	Fe₂O₃ batches	Magnetic field (Tesla)	Raman analysis
1	54.9	0.0	0	0	
2	41.6	0.5	1x	0	
3	45.5	1.0	1x	0	
4	68.7	0.0	0	0.4	
5	86.0	0.5	1x	0.4	Alignment
6	60.8	0.5	2x	0.4	
7	50.7	0.5	2x	0.4	
8	46.2	1.0	1x	0.4	Alignment
9	75.1	1.0	2x	0.4	
10	50.6	1.0	2x	0.4	
11	103.4	0.0	0	0.8	
12	49.8	0.5	1x	0.8	Alignment
13	58.9	0.5	2x	0.8	
14	45.9	1.0	1x	0.8	
15	55.3	1.0	2x	0.8	
16	87.9	1.0	2x	0.8	Alignment
17	44.6	0.0	0	0	

The glass transition temperature of the epoxy increases with increasing magnetic field and implies that there is some molecular orientation/alignment occurring in the epoxy. However, there is a decrease in glass transition temperature with the addition of the surfactant, NaDDBS, which could be expected, since NaDDBS is a low molecular weight material that could act as a plasticizer. The general glass transition temperature of the epoxy increases with the addition of the CNT-NaDDBS-iron oxide particles. In

some cases there is a significant increase of the glass transition temperature that appears to be correlated with the alignment of the carbon nanotubes and epoxy. The overall effect on the glass transition temperature is not completely understood at this point because of the inconsistencies within the samples. Since in this study there were many variables to contend with, a definitive determination of an overall behavioral trend of the T_g was not possible, especially given that the degree of alignment varied greatly from sample to sample. Nevertheless, in the samples in which the CNT were indeed aligned, the general trend showed that an increase in the extent of alignment caused an increase in T_g , as expected. Further confirmation of the degree of CNT alignment in the various samples was achieved by Raman spectroscopy, which is discussed in Section 8.4.4.

8.4.2 Compression Testing

The compression data that illustrates the effect of a magnetic field on the epoxy matrix alone can be seen in Figure 8.1. The corresponding results for the epoxy matrix after the addition of Fe_2O_3 -decorated, NaDDBS-dispersed carbon nanotubes at 0.5 wt% and 1.0 wt% can be seen in Figure 8.2 (a,b). Figure 8.3 (a-c) illustrates the changes in the stress-strain behavior of the composites as a function of the applied magnetic field of 0.4 and 0.8 Tesla, respectively.

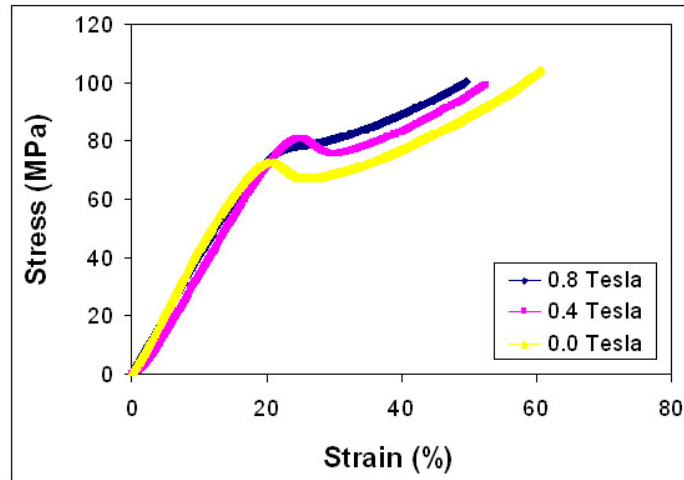


Figure 8.1: Experimental stress versus strain data from compression testing of the epoxy only at various magnetic fields. This illustrates the increase in yield point with increasing magnetic field.

The data presented in Figures 8.1-8.4 illustrate the mechanical response of the composites in the direction of a magnetic field at room temperature. Figure 8.1 shows that there is only a slight effect on the stress-strain data of the epoxy in the presence of a magnetic field. The linear portion of the graph (i.e. the elastic response of the matrix) remains relatively the same, but there is a change in the yield point. The yield point is very pronounced in the epoxy that was not placed under a magnetic field, but with increasing magnetic field becomes less pronounced. This indicates a toughening process, most likely due to chain alignment in the direction of the magnetic field, as previously reported.¹³⁴

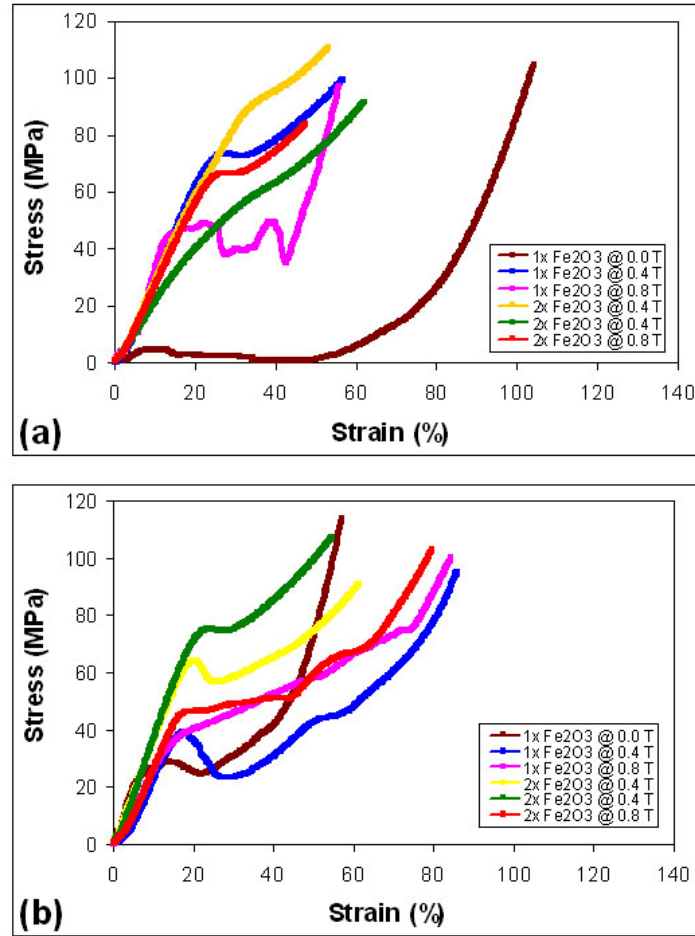


Figure 8.2: Experimental stress versus strain data from the compression testing of the composite samples. This illustrates the effect of magnetic field on (a) ½ wt% CNT (b) 1wt% CNT samples with various iron oxide particle concentrations. This illustrates the profound increase in plasticity that occurs with the addition of Fe₂O₃ and 0.5 wt% CNT at 0.0 Tesla, which disappears with increased magnetic fields and Fe₂O₃ content.

Figure 8.2a illustrates that the 0.5 wt% CNT-filled epoxy in the absence of a magnetic field is very flexible and undergoes extensive deformation at low stresses, but as the magnetic field increases there is an increase in strength and in yield point. This behavior is also seen in Figure 8.2b, which illustrates 1 wt% CNT-filled epoxy. Figure 8.2b illustrates a significant increase in the material stiffness with increase in magnetic field, coupled with a reduction in yielding, especially for single batch Fe₂O₃-decorated

CNT filled epoxy, suggesting a repression of the yielding mechanism due to chain alignment and reinforcement. It appears that there is a very pronounced yield point when the ratio of CNT to Fe_2O_3 is 1:1, but when this ratio is different, the yielding mechanism is repressed and hence, the yield point becomes less dominant.

Therefore, the yield point behavior depicted in Figure 8.3 (a-c) is consistently different, especially for the samples with a ratio of CNT to Fe_2O_3 that varies from 1:1, than that observed for the epoxy matrix alone and shown in Figure 8.1. This could mean that in the epoxy itself, the magnetic field induces a molecular reorientation or possibly alignment of the epoxy chains, thus causing a less pronounced yield point.^{97, 127, 206-209} In Figure 8.3a, there is evidence of a profound increase in plasticity that occurs with the addition of Fe_2O_3 and 0.5 wt% CNT at 0.0 Tesla. However, this effect disappears with increased magnetic fields and Fe_2O_3 content. Therefore, an increase in elastic modulus was observed in both the 0.5 and 1 wt% CNT at 0.4 (Figure 8.3b) and 0.8 Tesla (Figure 8.3c), most notably in the systems in which a double batch of iron oxide nanoparticles was used. It was also determined that neither 0.4 nor 0.8 Tesla exhibited a significant increase in strength, because the data produced inconsistent results. The overall composites properties were similar at the different concentrations and magnetic field strengths. Therefore, continuing this research with higher magnetic field strengths and sample preparation modifications to prevent inconsistencies might provide an optimal magnetic field needed to increase the modulus of the samples.

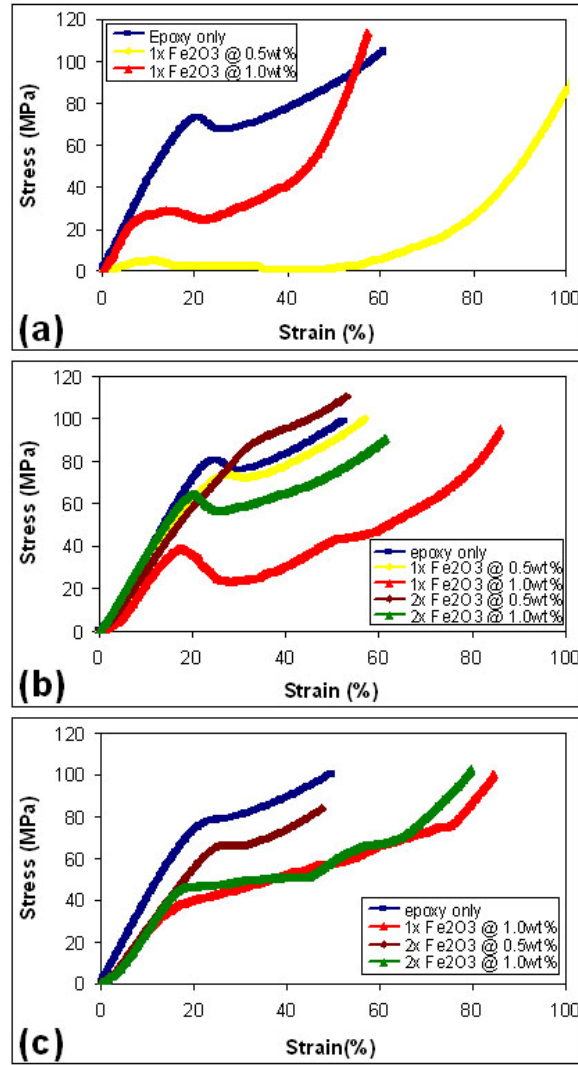


Figure 8.3: Experimental stress versus strain data from the compression testing of the composite samples. This illustrates the effect of the magnetic field on various concentrations of carbon nanotubes and iron oxide (a) 0 Tesla (b) 0.4 Tesla (c) 0.8 Tesla.

8.4.3 Effect on Young's Modulus

Table 8.3 illustrates the changes in the elastic moduli of the samples when the temperature was changed from room temperature (25 °C) to 100 °C, both for the direction parallel to that of the assumed CNT alignment (samples labeled with a) and for the direction perpendicular to the CNT direction of alignment (samples labeled with b). This

data can be understood only after taking into account the data shown in Figure 8.4 (a,b). Figure 8.4a illustrates that the increase in temperature has a pronounced effect on the properties of the epoxy in the presence of the magnetic field. In the absence of a magnetic field (at 0.0 Tesla) the elastic modulus above the glass transition temperature decreased as expected. At 0.4 Tesla, the elastic modulus does not change above the glass transition temperature due, most likely, to some degree of polymer chain alignment (also supported by the decrease in the extent of yield shown in Figure 8.1). Finally, at 0.8 Tesla, the epoxy exhibits a large increase in modulus above the glass transition temperature, which indicates that the magnetic field could in fact have the effect of aligning the polymer chains. However, it is not completely understood why there is no increase in the elastic modulus of the samples at room temperature when increasing the applied magnetic field from 0.4 to 0.8 Tesla. This could be interpreted to indicate that there is a minimum magnetic field strength required to induce alignment in the polymer chains.

Table 8.3 Summary of the compression test values for samples in alignment direction (#a) and perpendicular to alignment direction (#b) coupled with the Raman analysis.

Sample (#)	25 C Modulus (MPa)	100 C Modulus (MPa)	Raman Analysis
1a	282.7023726	65.27734811	
1b	49.07225673	99.30448667	
2a	0.087574013	91.14939407	
2b	0.448477451	150.4140271	
3a	194.2791742	40.65850245	
3b	42.33835011	66.14525771	
4a	95.11843105	87.22255282	
4b	52.93338373	81.40314942	
5a	12.31162143	62.66630675	alignment
5b	53.16157033	89.18974323	
6a	79.37667126	41.49192703	
6b	62.21599516	54.9913466	
7a	112.498603	5.797232046	
7b	54.20730997	3.165230748	
8a	103.2323482	77.18409137	alignment
8b	27.72319287	57.28173332	
9a	159.9277631	88.5311064	
9b	66.93790985	78.64735599	
10a	165.324802	35.8014695	
10b	92.01365099	6.795496643	
11a	319.2223583	80.78290993	
11b	65.35913553	65.55625587	
12a	181.4614326	105.4189657	alignment
12b	73.47282092	106.1621946	
13a	99.11760944	105.8697404	
13b	33.11983093	76.03132087	
14a	106.6323854	11.09853009	
14b	95.70656884	110.4437686	
15a	75.58125095	80.07094744	alignment
15b	27.19962447	110.9428681	
16a	96.36448735	83.92015326	
16b	51.34607265	86.62458064	

The analysis of the compression data at two temperatures (above and below the glass transition temperature of the epoxy matrix) was not straightforward and yielded results that were inconsistent with expected behavior. Figure 8.4b illustrates more clearly the difficulty in sample analysis, due to the inconsistent change in the elastic modulus. Some samples exhibit a drastic change in modulus from 25 °C to 100°C, while others show little to no change. From the data, it can be concluded that in samples having 0.5 wt% CNT and a double batch of iron oxide nanoparticles, the optimum alignment and enhancement of properties occurs with an applied magnetic field of 0.4 Tesla.

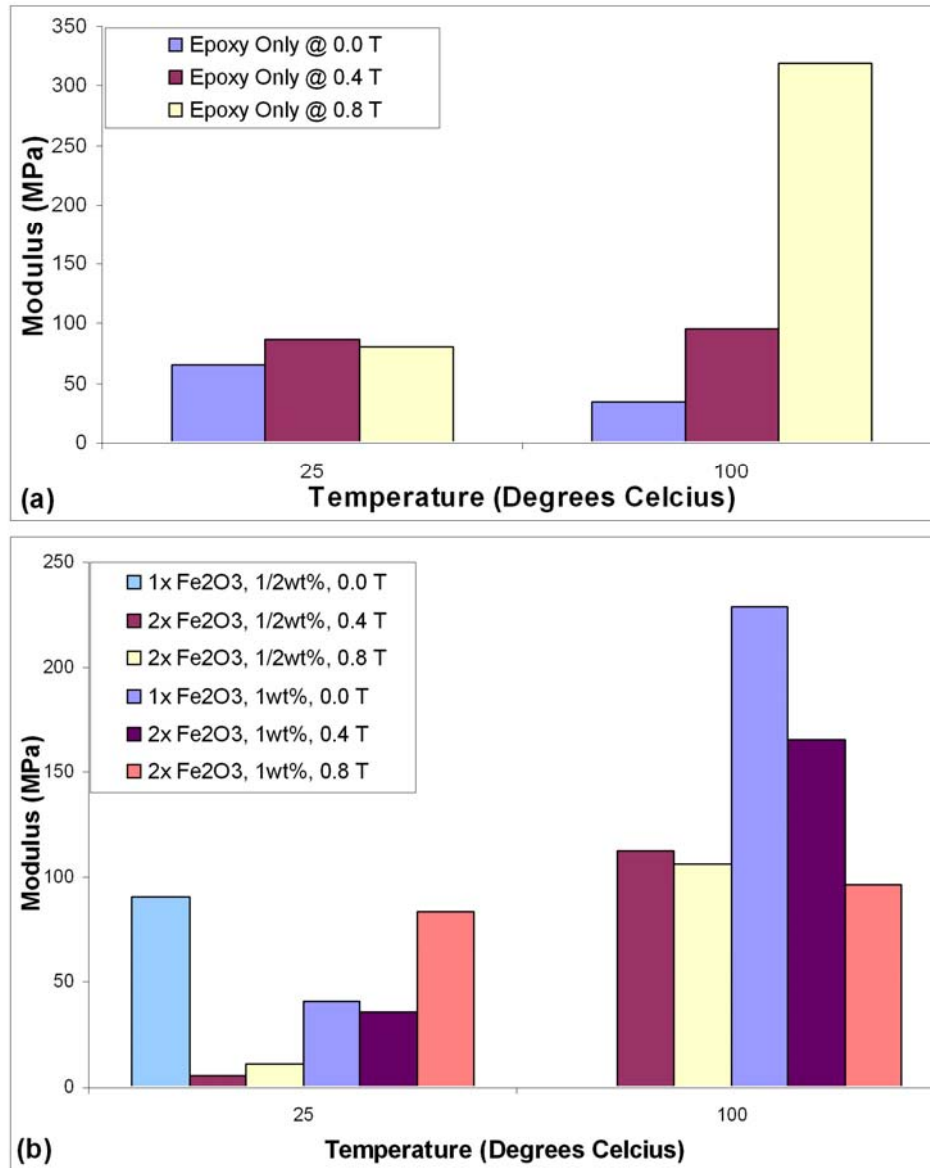


Figure 8.4: Experimental stress versus strain data from the compression testing of the composites samples. This illustrates the change in elastic modulus of the composite samples from room temperature (25°C) to above the glass transition temperature (100 °C) for (a) the epoxy only data and (b) the composite data sets at various carbon nanotube and iron oxide content. The data concludes that the epoxy only has a optimum magnetic field at 0.8 Tesla, conversely at 0.5wt% CNTs and a double batch of iron oxide there is an optimum magnetic field of 0.4 Tesla.

However, samples having 1 wt% CNT in the absence of an applied magnetic field exhibit the highest increase in elastic modulus with temperature, which subsequently decreases

with the application of a magnetic field and addition of iron oxide particles. Hence, the difficulty in the interpretation of the data is three-fold: (a) The epoxy itself had inconsistent data at 25 °C; (b) The possibility that certain concentration ratios of CNT and iron oxide inhibit alignment; (c) Samples without an applied magnetic field yielded increased moduli, presumably due to easier sample preparation. Therefore, alignment could not be inferred from compression data alone, but required additional independent evidence, and hence, had to be coupled with Raman spectroscopy.

8.4.4 Effect on Raman Scattering

The orientation-dependent Raman spectra of SWNT can be determined with different angles between the polarization of the incident laser light and the nanotube axis using VV (parallel polarization of the incidence and scattered light) configuration. The Raman scattering pattern of a carbon nanotube is unique to the properties of an individual tube. The differences depend on defects, wall thickness, and the conductivity of the carbon nanotubes. The scattering pattern also changes as a function of the absence or presence of strain on the carbon nanotube. It would make sense that other factors, such as a magnetic field, would affect the Raman scattering pattern.

The typical G band, which is found around 1591 cm^{-1} , corresponds to the resonantly excited metallic SWNT. In the set-up and sample positioning configuration used in this work (see Experimental section), this band shows a maximum intensity when the polarization of the incident radiation is parallel to the nanotube axis (i.e. $\alpha = 90^\circ$), and is minimal when the polarization of the incident radiation is perpendicular to the nanotube axis (i.e. $\alpha = 0^\circ$).^{130, 143, 200-202}

The analysis of the Raman spectra for this particular epoxy system using the G band of the SWNT cannot provide conclusive evidence of their alignment due to the

Raman peaks of the epoxy. The Raman spectra of the aligned epoxy and epoxy only samples are shown in Figure 8.5.

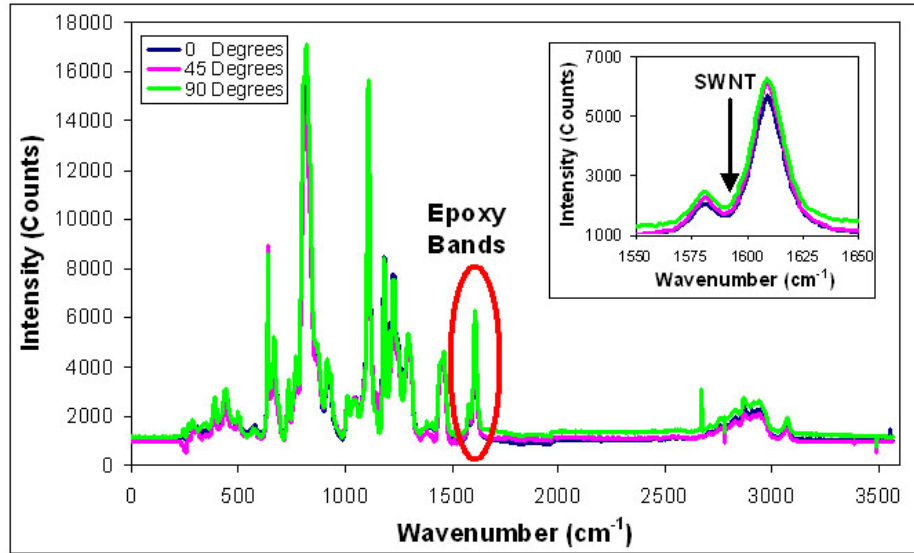


Figure 8.5: Raman spectroscopy data of epoxy only (a) complete spectra (b) CNT/epoxy G peak overlap. Therefore, the typical alignment analysis to determine alignment using the G band Raman peak is inconclusive.

From these spectra it becomes clear that the epoxy itself has a distinct Raman fingerprint, which is characterized by the presence of two peaks (see inset) that surround the 1591 cm^{-1} G band (which allows the determination of the orientation of carbon nanotubes). Therefore, we cannot unequivocally determine that we have orientation in the samples based solely on the G band peak.

It was previously determined by Frogley *et al.*,¹²⁹ that the G band peak is not the only peak from which alignment can be determined, but other peaks can be used, such as the D^* band. The D^* band is a second overtone of the D band, and its location is dependent upon the laser excitation energy used and the dispersion relation used between the D and D^* bands. For this system this band appears around $\sim 2600 \text{ cm}^{-1}$.¹²⁹ Therefore, the data from the samples were re-analyzed to determine if this particular peak could be used for the determination of the presence and degree of CNT alignment in the system.

The analysis proved difficult, because even after removing as much of the background and beam noise, this band resides in the wing of a broad, low-intensity band of the epoxy matrix located around 2500 cm^{-1} . However, from the peak at $\sim 2600\text{ cm}^{-1}$, the alignment of only a few of our samples was confirmed, as shown in Figure 8.6 (a,b). Figure 8.6a, shows the increase in the intensity of the D^* band as a function of the increase in the polarization angle from 0° to 90° . The intensity of the angular-dependent changes in this case is not of the same magnitude is found for the G band, but rather is on the order of 200-300 counts. However, the average intensity difference is higher than found in previous work.²⁵⁶ The Raman spectra allow a direct comparison of experimental data with theoretical calculations, as shown in Figure 8.6b. The experimental angular dependencies in our system exhibit a considerable deviation from the selection rules predicted by theoretical studies, where intensities scale with $\cos^4\alpha$.⁵⁵

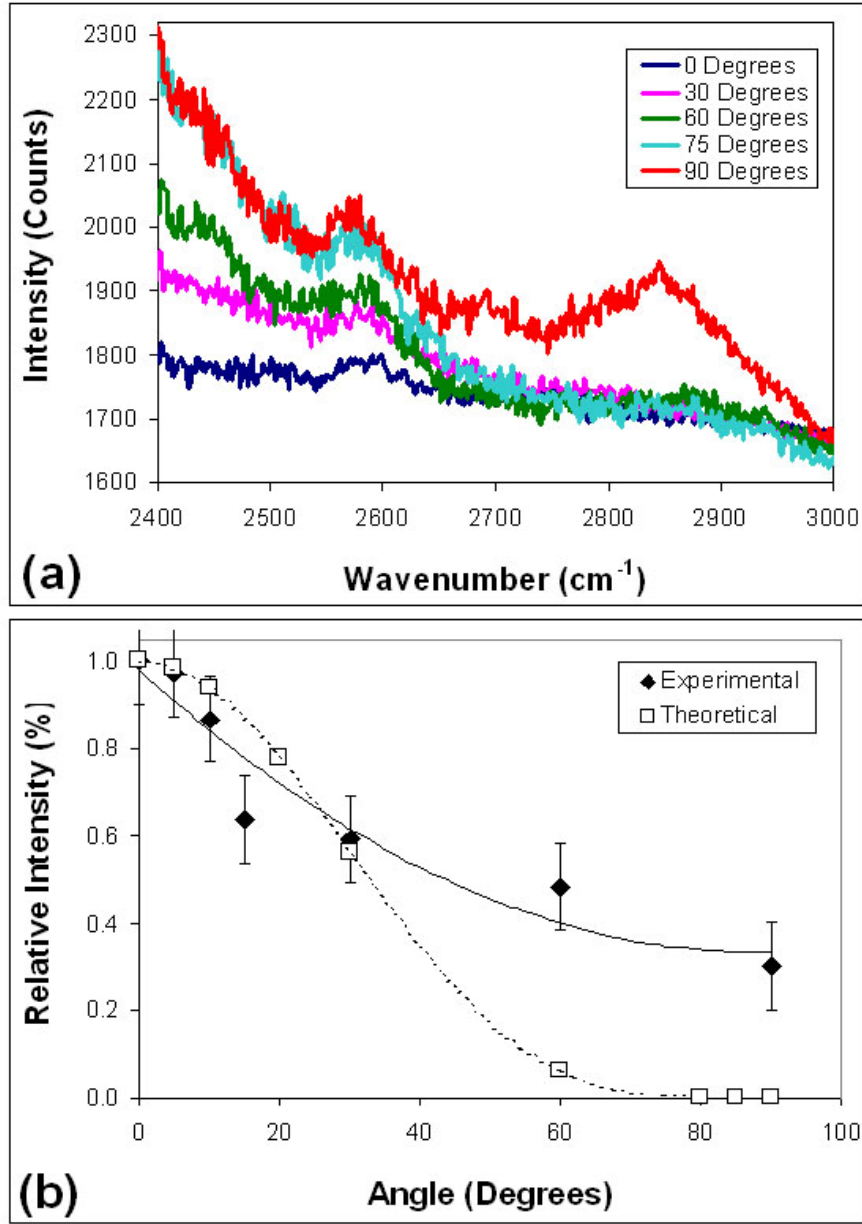


Figure 8.6: Raman spectroscopy data of aligned the CNT samples at 0.8 Tesla using the D band to determine alignment (a) peak over lap with epoxy peak at 2000 cm^{-1} (b) distinct Raman peaks. Although the intensity change is not as dramatic this illustrates that there is alignment in the carbon nanotube composite samples.

These differences may be attributed to depolarization effects generated by the pronounced anisotropic structure of the nanotubes and to electronic resonance effects, probably due in part to the presence of the iron oxide nanoparticles. Therefore, we can

conclude that in this work, we could find evidence of Fe₂O₃-decorated CNT alignment in an epoxy matrix upon application of a magnetic field only in some of the cases that were studied.

8.5 Summary of Decorating Carbon Nanotubes with Iron (III) Oxide Nanoparticles for Magnetic Field Alignment

In this work, we have analyzed the effect of a magnetic field on carbon nanotube alignment in epoxy-based composites. This work has illustrated that the magnetic field had a positive impact on the mechanical properties of the epoxy used. The alignment of carbon nanotubes in these samples was difficult to determine accurately and was not uniform for all samples. The reason for the non-uniformity is believed to be due to the concentration of iron oxide tethered to the surface of the carbon nanotubes, the magnetic field strength, and the variance in viscosity during curing. At 0.4 Tesla a lower concentration of iron oxide was needed to induce alignment, whereas at 0.8 Tesla a higher concentration of iron oxide was needed, results which is counterintuitive.

However, taking into consideration the results of the alignment experiments coupled with the characteristics of the processing methods and the changes of the viscosity in the samples, the reasoning behind the inconsistent results becomes clearer. The viscosity of the epoxy was strongly dependent on temperature, and the ability to quickly place the CNT-iron oxide-epoxy mixture into the mold and in the magnetic field. To evaporated off the excess water, the samples were kept at much higher temperatures than room temperature, resulting in a decrease in the viscosity of the system. If the sample were placed efficiently into the mold and be instantaneously subject to the effect of the magnetic field, alignment would have most likely occurred in all cases. Conversely, if too much time between mixing and processing would have elapsed, alignment would have been inhibited given the increasing viscosity of the resin, which

would have resulted in the decreased mobility of the iron oxide nanoparticles, epoxy matrix and CNT mixture. This work presented here points to the applicability of this in-situ processing method for the creation of a magnetically-induced aligned epoxy composite. However, the processing method needs to be further studied and most likely somewhat modified, in order to create uniformly aligned samples.

CHAPTER 9

CONCLUSIONS

This work has detailed the procedures of dispersion and alignment of carbon nanotube polymer based composites. Dispersion was demonstrated using surfactants and polymers, while two alignment techniques; shear flow and magnetic alignment; were explored. There were many techniques used to characterize the dispersion and alignment of the polymer composites by transmission electron microscopy, dynamic mechanical analysis, compression testing, differential scanning calorimetry, and Raman spectroscopy.

Dispersion of Carbon Nanotubes

The goal of the research was to modify current methods of dispersion carbon nanotubes to incorporate the dispersed carbon nanotubes into a final epoxy matrix. This research leads to the discovery of a complex problem when combining the dispersing agent, carbon nanotubes, and epoxy together. Dispersion of carbon nanotubes is more complex than typical nanomaterials. Even among the different methods of producing carbon nanotubes, nanotubes do not all disperse equally. This promotes difficulties when dispersing carbon nanotubes, because it is necessary to know the method at which they were produced and typical methods of dispersing particles has not been proven effective on carbon nanotubes⁶⁹.

There were three different dispersing agents used in this research, an anionic surfactant (NaDDBS), commercial dispersing agent (Disperbyk 2150), and a Pluronic (F108, PEO-PPO-PEO). The dispersing agents were chosen based on previous research⁴⁻⁶ which detailed their use as dispersing agents for carbon nanotubes. The dispersing agents were used based on the procedure of the previous work.⁴⁻⁶ It was determined that Disperbyk 2150 didn't adequately disperse the carbon nanotubes creating large bundles of dispersed carbon nanotubes and led to phase separation when added into an epoxy matrix. This material might prove more useful if placed with a more adequate one when paired with a miscible epoxy matrix.

The anionic surfactant used, NaDDBS, has been significantly researched and its ability to disperse carbon nanotubes is well documented. However, this surfactant appears to be limited by the concentration of carbon nanotubes used in solution. At high weight fractions NaDDBS can't accommodate all the carbon nanotubes, and leaves larger clusters of nanotubes. NaDDBS doesn't individually disperse carbon nanotubes, but disperse carbon nanotubes in bundles varying from 10-40 nm. This makes NaDDBS a useful dispersing agent for specific applications where it is not required to disperse the carbon nanotubes individually. In conjunction with the epoxy matrix, NaDDBS, had a very small effect on curing time (slight increase in time), and proved to have very consistent DMA results. Since, NaDDBS is a relatively small molecular weight molecule, the interactions between the epoxy and the surfactant remained favorable in the low weight fractions used to disperse carbon nanotubes. The final composite properties are significantly increased over that of the epoxy, and could be tailored to create a composite for a specific application.

The Pluronic used, PEO-PPO-PEO tri-block copolymer, has been previously researched at various PEO and PPO molecular weights⁶⁹. It was determined that at higher PEO molecular weights lead to better dispersed samples. As a dispersant the Pluronic proved itself. The Pluronic appears to be very consistent in being able to well disperse carbon nanotubes. The average bundle size found ranged between 10-20 nm. The problems with the Pluronic occurred with the incorporation into the epoxy matrix. The high molecular weight of the Pluronic leads to a significant increase in curing time, and the final polymer properties. The DMA results for the Pluronic materials were not consistent most likely due to insufficient mixing of the 4 component mixture (CNTs, Pluronic, resin, and hardener).

Even though each composite system had their own problems, the final composites still performed well. The composite strength was increased by several hundred percent. This is very promising, and with additional research the individual composite systems can be created for specific applications with specific strengths.

Alignment of Carbon Nanotubes

This research study was done to expand upon the current research techniques used to align carbon nanotubes in a matrix. In this research, two separate techniques were used to align the carbon nanotubes.

The first method chosen, shear flow, was used because of the simplicity of the system and theory behind how it works. Shear flow works on the premise that the carbon nanotubes will align because of the shear forces that are created during laminar flow. This research determined that purely increasing the rate of shear flow in an

aqueous solution was insufficient to align the carbon nanotubes, but required a high shear rate and viscous polymer solution. In a viscous polymer solution shear flow worked very well. It was determined by TEM that in solution the carbon nanotubes would align under constant shear flow or 100 RPMs.

This research was later expanded upon to attempt to align carbon nanotubes in a polymer matrix. This research utilized only two of the three dispersing agents used in this research, NaDDBS and Pluronic F108. These dispersing agents were chosen based on their ability to disperse the carbon nanotubes with small bundle sizes. The third dispersing agent, Disperbyk 2150, didn't prove to produce small bundle sizes, and was not used.

It was determined that while shear flow techniques were a viable alignment technique for viscous solutions, it was not a viable alignment technique for polymer composites. It is believed that the increased viscosity inhibited the carbon nanotubes from aligning. The final results remain somewhat contradictory, which lead to the conclusion that alignment, occurred in both directions. This conclusion was made, because in the process of hardening the polymer while aligning the carbon nanotubes the laminar flow slowly turned to turbulent flow, thus resulting in parallel regions of aligned carbon nanotubes.

The second method of alignment, alignment in a magnetic field, was chosen because of its novel and potential applications. Magnetic particles were tethered to the carbon nanotubes through the use of an anionic surfactant, NaDDBS. This surfactant had two purposes, to disperse the carbon nanotubes, and to tether the magnetic particles to the carbon nanotubes.

The magnetic particle chosen was iron (III) oxide, because of its magnetic properties, and its affinity to negatively charge ions. The iron (III) oxide creates a dipole of iron cations and oxygen anions. The iron cations will be attracted to the oxygen anions in the surfactant resulting in the iron particles to decorate the outside of the carbon nanotubes.

The iron (III) oxide particles were produced using sol gel processing techniques. It was determined that adding the surfactant, NaDDBS to the sol gel process resulting in a profound effect depending upon the metal salt used. Two metal salts were tested: (a) $\text{Fe}(\text{NO}_3)_3 \cdot 9\text{H}_2\text{O}$ and (b) $\text{FeCl}_3 \cdot 6\text{H}_2\text{O}$. The NaDDBS was added prior to the gelations agent, propylene oxide ($\text{C}_3\text{H}_6\text{O}$), and after the material was dried. The $\text{FeCl}_3 \cdot 6\text{H}_2\text{O}$ system still formed a gel, but the gel time was lengthened significantly (minutes to hours). It was found that the $\text{Fe}(\text{NO}_3)_3 \cdot 9\text{H}_2\text{O}$ system did not form a gel in the presence of the NaDDBS. This effect on the gelation was due to the precedence of the surfactant in an aqueous solution resulting in a clustering of molecules around the metal cation creating a barrier to gelation. The addition of the dispersing agent to the dried iron oxide material in addition to carbon nanotubes provided an easy method for tethering the iron oxide particles to the carbon nanotubes.

This mixture was then able to be used to create CNT-iron oxide-epoxy composites. The CNT-iron oxide mixture was added to the epoxy and allowed to harden in the presence of a magnetic field at 0, 0.4, and 0.8 Tesla. Two different concentrations of iron oxide were used a single synthesized batch and a double synthesized batch. The concentrations of carbon nanotubes used was 0, 1/2, and 1 weight percent. It was determined that although alignment occurred in some of the samples, the reason for

alignment can't be determined. Alignment and the absence of alignment occurred at 0.4 and 0.8 Tesla at both concentrations of iron oxide. The final samples prove to have inconsistent results, and without modifications it can't be considered a viable alignment technique.

Overall Composite Analysis

This work was able to create disperse carbon nanotube composites that have superior mechanical properties over the original matrix material. The composite materials with the NaDDBS dispersing agent yielded an 1100% increase in modulus, and the Pluronic dispersing agent yielded an 1100% increase in modulus. The alignment of carbon nanotubes in composite was not fully attained. The results are promising in the fact with modified procedures and techniques alignment of the carbon nanotubes could be obtained.

CHAPTER 10

RECOMMENDATIONS

This research project was successful in creating dispersed and aligned carbon nanotube composites. DMA, compression testing, XRD, Raman spectroscopy, and Transmission electron microscope were instrumental in determining the dispersing, alignment, and mechanical properties of these composite materials. Utilizing other techniques to analyze the properties such as, cryo-TEM or cryo-SEM might prove helpful in analyzing the carbon nanotube composite structure more closely.

One research experiment that would prove to be very useful is to determining the effect of the dispersing agent on the matrix material. This would require using several different dispersing agent and matrix materials to determine the effect on the composite properties. The systems would need to be picked based on there ability to create a composite without inhibiting the dispersing of the carbon nanotubes or causing phase separation. By testing analyzing the composite structure using microscopy methods and mechanical testing it can determine the effectiveness of the dispersing in the matrix and the utilization of the carbon nanotube properties. Likewise, determining an epoxy that can effectively disperse the carbon nanotubes without the need of dispersing agents would be very useful.

The techniques used in this research need to be modified to produce more promising and consistent results. The method of aligning carbon nanotubes via shear

flow can be modified by using different shear rates to help determine the effect on shear rates on highly viscous matrix materials. By using several different matrix materials that having varying viscosities it can be determine what viscosity is needed to create an aligned matrix without inducing turbulent flow causing misalignment. Modifying this method using these two parameters could lead to finding an ideal matrix material and shear rate that would allow for uniform alignment.

The results for the samples made in a magnetic field are inconsistent. By limiting the causes of inconsistencies it might be understood why alignment occurred in some samples. By modifying the method by repeating tests, higher magnetic fields, and different matrix materials could provide insight to what caused the alignment in the samples to occur.

Finally, determining what might be the best sample geometry to get ideal mechanical characterization, which will confirm the alignment of the samples. The current study used sample geometries that were not ideal, because of testing limitations. Thus, by determining ideal samples geometry that coincides with testing strengths would produce more precise results.

APPENDIX A

TWO-POINT PROBABILITY FUNCTION ANALYSIS FOR ANISOTROPIC CARBON NANOTUBE COMPOSITES

Abstract

This work uses the empirical equations of the two-point probability functions for a carbon nanotube (CNT) polymer based composite to investigate the ability of these equations to adequately portray the composite structure. From the analysis of the varying volume fractions (1%-30% CNTs) it was determined that very low volume fractions cannot be adequately portrayed. The images analyzed must contain high concentrations of CNTs and might be unrealistic concentrations and microstructures for composites. The low concentration microstructure was inadequately portrayed due to the uniqueness of the structure and the inability to adequately capture the CNTs through statistical analysis.

Introduction

Composite research has been around for years; today fillers are used to manipulate a material's properties¹²³. Carbon and glass fibers are the most widely used fillers to create conductive polymers¹²³. Since the discovery of single-walled carbon nanotubes and their exceptional mechanical properties, the idea of using them as reinforcing fibers in

composite materials has been a driving force for composite testing^{2, 3, 257, 258}. The Young's modulus of any material is related to the cohesion of the atoms and molecules that make up the solid⁵¹. However, early nanotube reinforced polymer composites have actually failed to utilize the full mechanical potential of carbon nanotubes^{1, 42}. The reason for the failed samples is due to the microstructures that are created. The CNTs orient themselves in very random directions and are not adequately dispersed to induce good cohesion between the matrix and the filler. This resulted in problems when producing SWNT composites, with ease and the ability to adeptly use them to create composite materials. There are several different methods available to align carbon nanotubes, including slicing⁹³, chemical vapor deposition⁹¹, melt processing¹⁸⁸, mechanical stretching⁹⁹, electrophoresis¹⁸⁹, application of magnetic fields,^{97, 127, 190} and electrospinning¹⁹⁴⁻¹⁹⁶. A problem with most alignment processes arises when combining the carbon nanotubes with the polymer matrix to form the composite materials.

In creating carbon nanotube composites there are many key factors in creating a new composite; structure, properties, performance, and processing.²⁵⁹ Most research uses the guess and test method of creating a new microstructure, but what if the type of microstructure needed could be created to get the desired properties? The ability to predict the macroscopic properties of a bulk material by analyzing a representative microstructure of the bulk sample has been gaining interest in materials research recently.²⁶⁰⁻²⁶² Two- point statistical analysis has been and can be used to predict mechanical properties.²⁶¹ Two-point statistical analysis allows the user to incorporate morphology, particle distribution, and the properties of the individual phases and components to determine the overall properties of the microstructure.²⁶¹

There are several factors that affect the material properties, volume fraction, surface area interfaces, orientation, sizes, shapes, spatial distribution, and many others. The ability to take all the properties into account would require an n-point correlation function, but the ability to use a more simplified equation would allow for more efficient use of the correlation functions.

Statistical Modeling of Carbon Nanotube Properties

Statistical modeling of materials is not a new concept and has been around for decades²⁶¹. In more recent years the focus has changed from crystalline materials to being able to predict the properties of nanomaterials, particularly carbon nanotube composites^{261, 263, 264}. However, this field proves to be a very challenging one due to the large number of unknown factors and assumption about the interphase region between the carbon nanotubes and the matrix^{261, 263, 264}. In this section, the background of n-point statistics will be addressed and how it relates to composite materials.

Table A.1: Nomenclature for distribution functions

Nomenclature	
A	degree of anistropy
α_{ij}	function of volume fraction
β_{ij}	function of volume fraction
c_{ij}	empirical constants
$I(x)$	function that indicates if it lands in phase i or in phase j
N	total number of points
N_i	totally number of points in phase I
n_{ij}	empirical constants
P_{ij}	probability of vector r starting in phase I and ending in phase j
P_{ij}^o	$P_{ij}(r=r_{ij}^o)$
$r, r $	magnitude of vector r
r_j	vector, where the beginning is some pre-determined origin and the end is point r_i
r^o	characteristic length scale
S_n^i	n point probability function that is made up of the indicator function for every point
v_i	volume fraction of phase I

N- Point Distribution Functions

These probability functions use mathematical models to determine the probability of n points of x landing in phase i . For a given point there is an indicator function $I^{(i)}(x)$, where the indicator function is either 1, it lands in phase i , or 0 it doesn't land in phase i . In this case phase i can be any type of phase, solid, fluid, or void. The n point probability function can then be illustrated by the averages of the indicator functions for each point x .

$$S_n^{(i)}(x_1, x_2, \dots, x_n) \equiv \langle I^{(i)}(x_1) I^{(i)}(x_2) \dots I^{(i)}(x_n) \rangle$$

$$I^{(1)}(x) + I^{(2)}(x) = 1 \quad \text{(Eqn A.1)}$$

$$P\{I^{(1)}(x) = 1\} \quad P\{I^{(1)}(x) = 0\} = 1 - P\{I^{(1)}(x) = 1\}$$

Where S_n only depends on the relative positions of x , and the first term S_1 is a constant volume fraction, ϕ_i .

The n-point probability functions originated from determining the effective transport properties of random media by Brown.^{259, 265} These statistical functions have been found to be able to model several important macroscopic properties: effective conductivity, dielectric constant, magnetic permeability, elastic modulus, and fluid permeability.²⁵⁹

One -Point Distribution Functions

N - point distribution functions are used to determine the macroscopic properties of microstructures; an example microstructure is illustrated in Figure A.1.

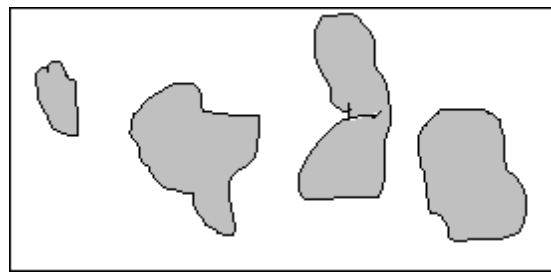


Figure A.1: *General 2 Phase Composite Microstructure*

The data acquired by an n - distribution function starts with throwing a random number of points in a microstructure. Essentially all n-point distribution functions originate from one-point distribution functions, which consist of throwing random points across a microstructure to collect information about the microstructure from this initial set of points.

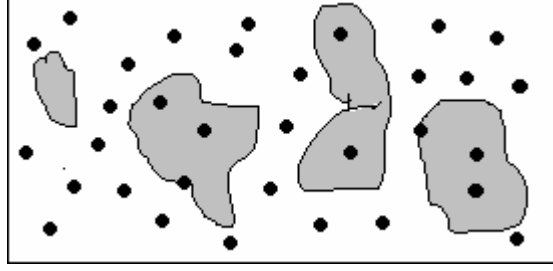


Figure A.2 *Determining the Volume fraction*

From this set of points the volume fraction can be determined, where the number of points in one phase compared to the total number of points gives the volume fraction. For the two-phase composite case, i and j , which corresponds to phase 1 and 2 the following relations can be determined.

$$\frac{V_i}{V_{total}} = v_i, i = 1, 2 \quad v_1 = P(\varphi_1), \quad v_2 = P(\varphi_2) \quad P(\varphi_1) + P(\varphi_2) = 1.0 \quad (\text{Eqn A.2})$$

Two Point Distribution Functions

Two-point distribution functions start out using one-point distribution functions, and build upon them. Thus, by taking the points that were initially used to determine the volume fraction and connect a vector, where the vector will vary by length and orientation (0-90°). From this set of vectors, the data can be analyzed to determine the probabilities of the vectors to be in to begin or end in the different phases (in this case phase 1 and phase 2).

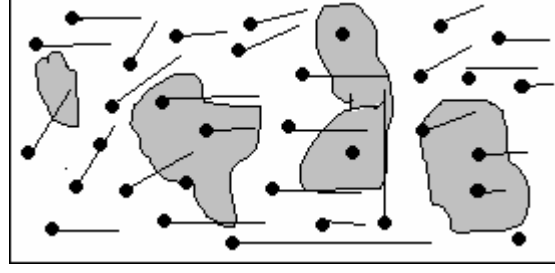


Figure A.3: *Determining end point of the Vectors, r*

This results in a number of random vectors within the microstructure, where each vector has a head and a tail, that has a probability of hitting phase 1 and phase 2.²⁶⁶ Two point correlations are defined as the average probability that both the end points of a randomly located and oriented straight line of length r are contained in particles (phase 1).²⁶⁷ However, both the head and the tail do not have to land in the same phase. By determining the probabilities of the head and tails of the vectors landing in a particular phase can be used to determine four different probabilities (P_{11} , P_{12} , P_{21} , P_{22}). The four probabilities represent the average probabilities of the possible results of where the head and tail vectors land²⁶⁷. For example, P_{11} is the probability that both the head vector and tail vector are in phase 1, and P_{12} is the probability that the head lands in phase one and the tail lands in phase 2, where P_{21} is the average probability of the head landing in phase 2 and the tail in phase 1, and P_{22} is the average probability of both head and tail landing in phase 2²⁶⁷. The four different probabilities can be determined by the number fractions.

$$P_{ij} = \frac{N_{ij}}{N} \bigg|_{N \rightarrow \infty} \left\{ \vec{r} = \vec{r}_j - \vec{r}_i, (\vec{r}_i \in \phi_i) \cap (\vec{r}_j \in \phi_j) \right\} \quad (\text{Eqn A.3})$$

Where N_{ij} is the number of vectors that begin in phase i (ϕ_i) and end in phase j (ϕ_j). The correlation functions are not all independent variables but follow a simple relationship shown in equations 4-6²⁶⁷.

$$\langle P_{11}(r) \rangle + \langle P_{12}(r) \rangle + \langle P_{21}(r) \rangle + \langle P_{22}(r) \rangle = 1 \quad (\text{Eqn A.4})$$

$$\langle P_{12}(r) \rangle = \langle P_{21}(r) \rangle \quad (\text{Eqn A.5})$$

$$\langle P_{11}(r) \rangle + \langle P_{12}(r) \rangle = \phi_1 \quad (\text{Eqn A.6})$$

$$\langle P_{21}(r) \rangle + \langle P_{22}(r) \rangle = \phi_2$$

These equations above illustrate that the sum of all the probabilities must equal one. The volume fraction can then be determined by the summing the probabilities with the same initial point. If a vector lands in phase 1 and then in either phase 1 or 2, it is exactly equal to the volume fraction of the initial point.²⁶⁷

The two point function then can be defined by probabilities and as the vector, r goes to zero the functions reduce to one-point functions.²⁶⁶

$$P_{ij}(\vec{r}) = P\{\vec{r}_i \in \phi_i \mid \vec{r}_j \in \phi_j\} P(\vec{r}_j \in \phi_j) \quad (\text{eqn A.7})$$

$$P_{12}(0) = P_{21}(0) = 0, P_{11}(0) = v_1, P_{22}(0) = v_2$$

The values of P_{ij} then reduce and can be easily determined and said to be the boundary conditions of the two-point probability function. The values are shown in Table 2.4.

Table A.2 *Limiting conditions for the two-point probability function*¹⁸⁵

P_{ij}	Boundary conditions		Result coefficients	
	$r = 0$	$r \rightarrow \infty$	$\alpha_{ij} =$	$\beta_{ij} =$
P_{11}	V_1	V_1^2	V_1^2	$V_1 V_2$
P_{12}	0	$V_1 V_2$	$V_1 V_2$	$-V_1 V_2$
P_{21}	0	$V_1 V_2$	$V_1 V_2$	$-V_1 V_2$
P_{22}	V_2	V_2^2	V_2^2	$V_1 V_2$

Corson's Equation

There are several different mathematical forms of the two-point probability function, but the one that will be used here is the modified Corson's equation.^{185, 261, 268,}

269

$$P_{ij} = \alpha_{ij} + \beta_{ij} e^{-c_{ij} r^{n_{ij}}} \quad (\text{Eqn A.8})$$

In this equation for the anisotropic case, r is a vector, but for an isotropic case the probability doesn't depend on the direction and r is assumed to be a scalar. Alpha and beta are determined by the boundary conditions and the empirical coefficients c_{ij} and n_{ij} are microstructure parameters. This equation can be re-written to determine n_{ij} and c_{ij} from experimental data through mathematical manipulation, as seen in equation 12.

$$\ln \left(\ln \left(\frac{P_{ij} - v_{ij}^2}{v_{ij} * v_{ij}} \right) \right) = y = n_{ij} \ln r + \ln c_{ij} \quad (\text{Eqn A.9})$$

This equation allows for the determination of n_{ij} and c_{ij} for each individual probability, P_{ij} . Where n_{ij} is very close to 1 for anisotropic media, as proven by Gokhale, *et al.*, and c_{ij} is a scaling parameter represented by the correlation distance.²⁷⁰

The coefficients can be altered for anisotropic media in the following equations

$$n_{ij}(\theta, \alpha) = n_{ij}^0 (1 - (1 - A) \sin \theta) \quad (\text{Eqn A.10})$$

$$c_{ij}(\theta, \alpha) = c_{ij}^0 (1 + (1 - A) \sin \theta) \quad (\text{Eqn A.11})$$

Where A is a material parameter, the degree of anisotropy, and in isotropic microstructures $A=1$.²⁶¹ From the information gathered by these equations, leads to the possibility of characterizing the composites properties, and applying that knowledge gained to creating better composites.

Simulation and Results

The samples analyzed in this section are TEM images of single-walled carbon nanotubes (SWNTs) dispersed in anionic surfactant. The solutions have varying SWNT concentrations, and the TEM images represent high CNT and low CNT concentrations within the individual samples. The CNTs do not uniformly adhere to the grids allowing for varying concentrations to be analyzed.

The concentrations of the TEM images are determined by one-point statistical analysis. Other methods of determining CNT concentrations were employed, such as from the solution concentration and image analysis techniques, but were found to estimate much higher concentrations than the statistical data. The reason for this is believed to be the unique microstructure created by dispersed CNTs, and remnant catalyst particles found in the solution.

The micrographs of a high concentration and low concentration sample are shown in Figure A.1 (a,b).

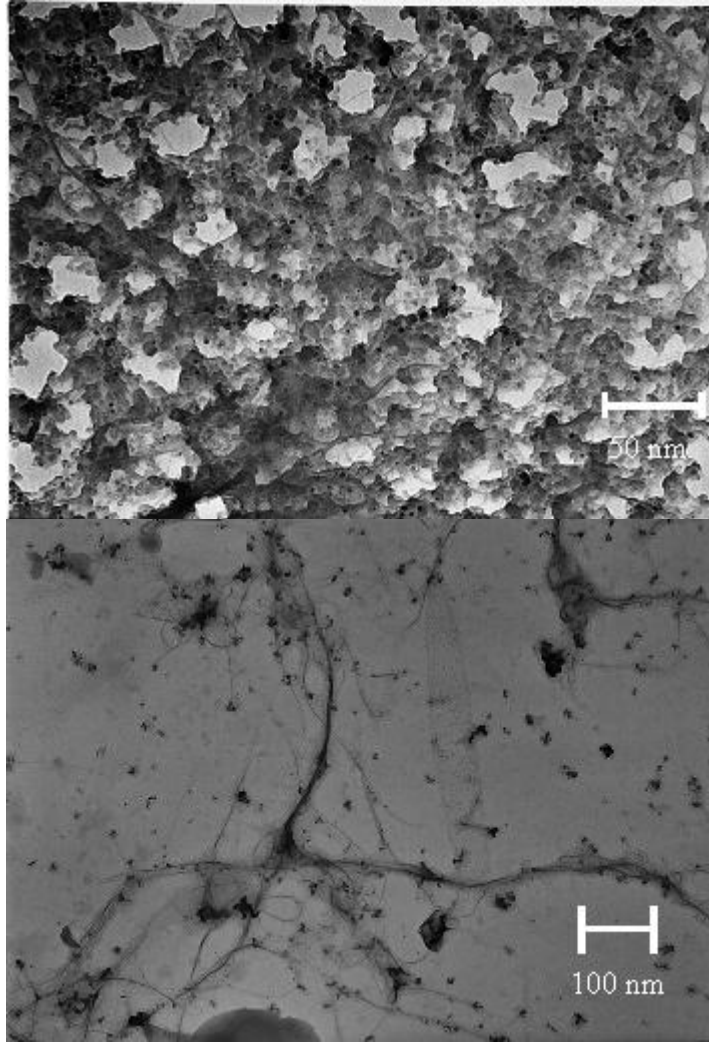


Figure A.3: (a) High concentration (b) Low concentration of CNT and Surfactant

Figure A.1b resulted in a microstructure of too low concentration to accurately use the modified Corson equation, because the concentration from the data was approximately 98% matrix and 2% filler. The data resulted in an almost linear data set (data varied from .80-.88), and doesn't fit the exponential equation by the modified Corson equation, as seen in Figure A.2.

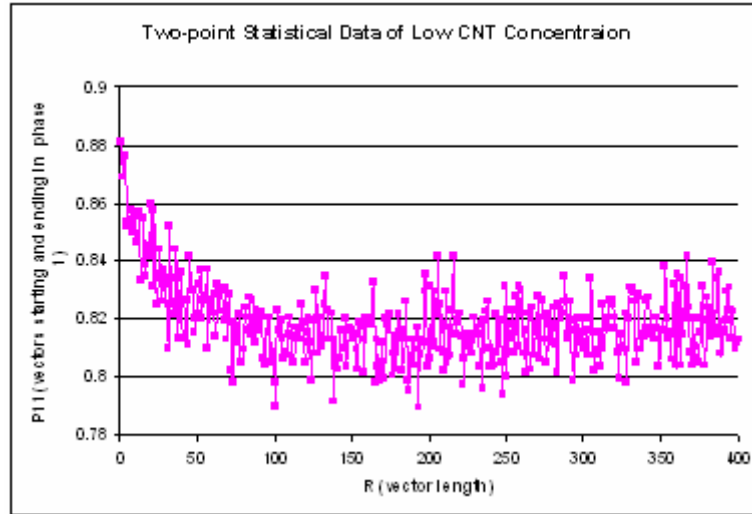


Figure A.4: Two-Point Statistical Data of Low CNT Concentration

This proves to be problematic, because carbon nanotube composites are inherently low weight fraction composites. The appeal of using carbon nanotubes over carbon fibers or other commonly used fillers is the ability to decrease the amount of filler used and at the same time increase the stiffness of the material. Higher concentration CNT composite samples are not impossible to create, but generally are more difficult to keep dispersed. The addition of large amounts of CNTs should require large amounts of surfactant to be used, however, with increasing amounts of surfactant there isn't increased dispersion. In some cases the addition of increased surfactant yields aggregation.⁵ Thus making analyzing CNT composites via two-point statistical functions challenging.

However, analysis of the high concentration CNT solution, which was found in a different portion of the TEM grid, proved to actually follow the modified Corson's equation. The data is shown in Figure A.3.

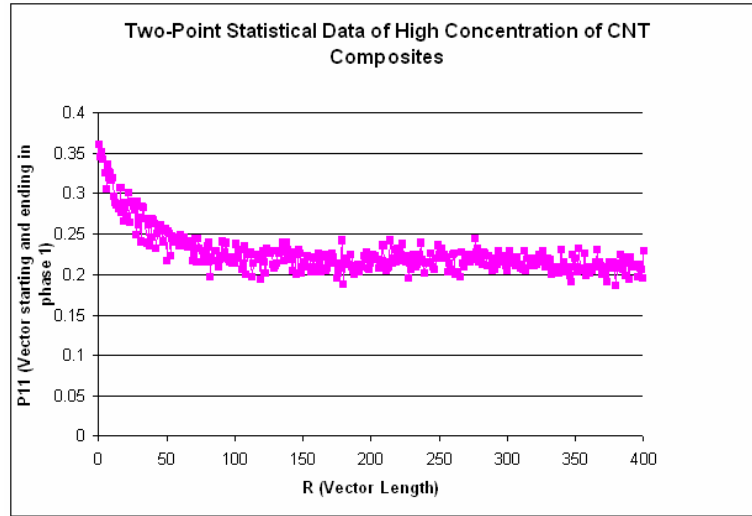


Figure A.5: Two-Point Statistical Data of High CNT Concentration

The data illustrates an exponential function with a large degree of variation (.36-.19), which fits the modified Corson's equation. This data set can be analyzed using equation 2.13 and 2.14, to determine c_{ij} and n_{ij} for this angle and probability. For each angle (0-90°) and each probability (P_{11} , P_{12} , P_{21} , P_{22}), there will be a separate c_{ij} and n_{ij} . The data set for a high concentration of CNTs at zero and ninety degrees are shown in Figure 7.

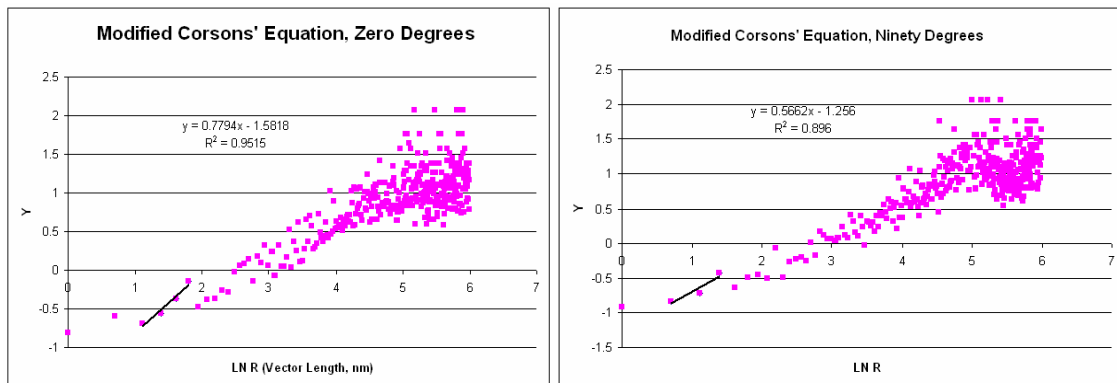


Figure A.6: Modified Corson's Equation applied to Two-point Statistical Data

The data isn't ideal and appears to only fit the modified Corson's equation at the very first vectors. It was found that only certain angles had n_{ij} that were near 1. The results lead to the conclusion that the microstructures analyzed are not completely anisotropic as previously believed. Also, it was determined that the program used to determine the data needed modifications. Varying the angles from 0-90°, while in theory is a good idea, however, doesn't translate perfectly into pixels. For an individual pixel the only angles that will hit an actual pixel are 0°, 45°, and 90°. As the vector length increase the amount of pixels increase, and therefore long-range data would be still useful. However, the amount of scattering seen in the data illustrates that there isn't a good pixel representation for the long-range data. Therefore, the program needed to be modified using a overlapping or tiling type method to increase the amount of pixel data represented.

CONCLUSION

The main problems with analyzing carbon nanotube composites deals with the size of the CNTs, because they are so small the volume fraction that is added to the composite is very small. This happens to be a reason why CNTs are used for fillers, because small amounts create a composite with better properties than current composites. The two-point analysis of CNT composites then proves to be very challenging. The TEM images analyzed were unable to adequately portray the microstructure, because there was a lack of long-range data. By altering the program, the two-point analysis may prove to be a very helpful tool in adequately analyzing the CNT composite microstructure and modeling an ideal microstructure of structural use.

REFERENCES

1. Andrews, R., D. Jacques, M. Minot, and T. Rantell, Fabrication of Carbon Multiwalled Nanotube/Polymer Composites by Shear Mixing. *Macromolecules Materials*, **2002**. 287:395.
2. Treacy, M. M. J., Ebbesen, T. W., Gibson, J. M., Exceptionally high Young's Modulus observed for individual carbon nanotubes. *Nature*, **1996**. 381:6584.
3. Yu, M. F., Lourie, O., Dyer, M. J., Noloni, K., Kelly, T.F., Ruoff, R. S., Strength and breaking mechanism of multiwalled carbon nanotubes under tensile load. *Science*, **2000**. 287:637.
4. Li, Q., Zaiser, M., Koutsos, K., Carbon nanotube/epoxy resin composites using a block copolymer dispersing agent. *Physica Status Solidi*, **2004**. 201(13):R89.
5. Matarredonna, O., Rhoads, H., Li, Z., Harwell, J.H., Balzano, L., Resasco, E., , Dispersions of Single-Walled Carbon Nanotubes in Aqueous Solutions of the Anionic Surfactant NaDDBS. *Journal of Physical Chemistry B*, **2003**. 107:13357.
6. O'Connell, M. J., et. al., Band Gap Fluorescence from Individual Single-Walled Carbon Nanotubes. *Science*, **2002**. 297:593.
7. Schaffer, J. P., A. Saxena, S. D. Antolovich, J. Thomas H. Sanders, and S. B. Warner, *The science and design of engineering materials*. 2nd ed. 1999: McGraw-Hill. 826.
8. Callister, W. D., *Material Science and Engineering: An Introduction*. Vol. 6. 2000, New York: John Wiley and Sons, Inc.
9. Shaffer, J. B., A. Saxena, S. D. Antolovich, T. H. S. Jr., and S. B. Warner, *The Science and Design of Engineering Materials*. second ed. 1999: McGraw Hill. 826.
10. Astrom, T. B., *Manufacturing of Polymer Composites*. 1997: CRC Press. 469.
11. Kushwaha, S. S. S. and J. Mishra, Preparation and characterization of magnesium ion conducting glass-polymer composites films. *Current Science*, **2005**. 88(7):1159.
12. Baucom, J. N. and M. A. Zikry, Low-velocity impact damage progression in woven E-glass composite systems. *Composites, Part A: Applied Science and Manufacturing*, **2005**. 36A(5):658.
13. Burkle, R., S. Deutschbein, R. Mauch, K.-h. Sossenheimer, and A. Weber, *Polymer-coated composite smooth optical films for display devices for electronic components*. 2000, (Schott Glas, Germany). Germany. p. 39

14. Imashita, K. and S. Yokokura, *Water-resistant glass-organic polymer composites and their manufacture*. 1994: Japan. p. 6
15. Osawa, T. and K. Yoshino, *Electrically conductive glass-polymer composites*. 1989: Japan. p. 4
16. Ende, D. A., P. Almeida, and S. Zwaag, Piezoelectric and mechanical properties of novel composites of PZT and a liquid crystalline thermosetting resin. *Journal of Materials Science*, **2007**. 42(15):6417.
17. Xu, L., W. Chen, J. Zhou, and J. Li, Preparation and properties of fine scale 1-3 piezoelectric ceramic/polymer composites. *Wuhan Ligong Daxue Xuebao*, **2006**. 28(6):1.
18. Khan, Y. M., E. K. Cushnie, J. K. Kelleher, and C. T. Laurencin, In situ synthesized ceramic-polymer composites for bone tissue engineering: bioactivity and degradation studies. *Journal of Materials Science*, **2007**. 42(12):4183.
19. Arbatti, M., X. Shan, and Z. Cheng, Ceramic-polymer composites with high dielectric constant. *Advanced Materials (Weinheim, Germany)*, **2007**. 19(10):1369.
20. Szafran, M., G. Rokicki, E. Bobryk, and B. Szczesna, Effect of ceramic-powder surface modification on properties of ceramic-polymer composites used in dentistry. *Kompozyty*, **2006**. 6(3):78.
21. Ren, Y., K. Yang, J. Huang, B. Zhang, and Z. Yao, *Application of degradation-controllable polymer/metal composite material in medicinal implant*. 2007, (Institute of Metal Research, Chinese Academy of Sciences, Peop. Rep. China). p. 7
22. Lim, E.-S., J.-C. Lee, J.-J. Kim, E.-T. Park, Y.-K. Chung, and H.-Y. Lee, Dielectric characteristics of polymer-ceramic-metal composites for the application of embedded passive devices. *Integrated Ferroelectrics*, **2005**. 74:53.
23. Lavu, B. C., M. P. Schoen, and A. Mahajan, Adaptive intelligent control of ionic polymer-metal composites. *Smart Materials and Structures*, **2005**. 14(4):466.
24. Shahinpoor, M. and K. J. Kim, Ionic polymer-metal composites: IV. Industrial and medical applications. *Smart Materials and Structures*, **2005**. 14(1):197.
25. Chung, D. D. L., *Carbon Fiber Composites*. 1994, Boston: Carbon Fiber Composites. 211.
26. Edison, T. A., *Incandescing Electric Lamp*. 1889, (Edison Electric Light Company, USA). US.

27. Edison, T. A., *Incandescent-Lamp Filament*. 1889, (USA): US.
28. Colbert, D. T., Smalley, R. E., Past, Present, and Future of Fullerene Nanotubes: Buckytubes. *Perspectives on Fullerene Nanotechnology*, **2002**:3.
29. Bacon, R., Growth, Structure, and Properties of Graphite Whiskers. *Journal of Applied Physics*, **1960**. 31:283.
30. Oberlin, A., M. Endo, and T. Koyama, Filamentous growth of carbon through benzene decomposition. *Journal of Crystal Growth*, **1976**. 32(3):335.
31. Kroto, H. W., J. R. Heath, S. C. O'Brien, R. F. Curl, and R. E. Smalley, C60: buckminsterfullerene. *Nature (London, United Kingdom)*, **1985**. 318(6042):162.
32. Tennent, H. G., *Carbon fibrils, method for producing same and compositions containing same*, U. States, Editor. May 5 1987.
33. Tomanek, D., *The Nanotube Website*. 2004.
34. Bernhold, J., et. al., Theory of growth and mechanical properties of nanotubes. *Applied Physics A: Materials Science & Processing*, **1996**. 67:39.
35. de Heer, W. A., Bacsá, W.S., Chatelain, A., Gerfin, T., Humphrey-Baker, R., Forro, L., Ugarte, D. , Aligned Carbon Nanotube films: Production and Optical and Electronic Properties. *Science*, **1995**. 268(5212):845.
36. Dresselhaus, M. S., G. Dresselhaus, and P. C. Eklund, *Science of Fullerenes and Carbon Nanotubes*. 1996, Academic Press: San Diego, CA. p. 965.
37. Huczko, A., Synthesis of aligned carbon nanotubes *Applied Physics A: Materials Science & Processing*, **2002**. 74:617.
38. Chang, R., *Chemistry*. 5 ed. 1994, Highstown: McGraw-Hill, Inc. 994.
39. Barone, P., H. G. Chae, C. Chan, S. B. Chikkannanavar, C. P. Collier, S. K. Dooron, C. A. Dyke, M. Freitag, R. J. Grow, D. Heller, F. Hennrich, J. Kono, S. Kumar, J. Liu, D. E. Luzzi, D. Mann, V. Moore, M. O'Connell, S. Roche, M. Rolandi, B. W. Smith, M. S. Strano, J. M. Tour, and M. Usrey, *Carbon Nanotubes: Properties and Applications*, ed. M.J. O'Connell. 2006, Boca Raton, FL: Taylor & Francis.
40. Dresselhaus, M. S., G. Dresselhaus, and R. Saito, Physics of Carbon Nanotubes. *Carbon*, **1995**. 33:883.

41. Fink, J. H. and P. Lambin, Carbon Nanotubes. *Topics Applied Physics*, **2001**. 80:247.
42. Bernholc, J., M. B. Nardelli, V. Meunier, and C. Roland, Mechanical and Electrical Properties of Nanotubes. *Annual Review Material Research*, **2002**. 32:347.
43. Barber, A. H., S. R. Cohen, and H. D. Wagner, Measurement of carbon nanotube-polymer interfacial strength. *Applied Physics Letters*, **2003**. 82(23):4140.
44. Thostensona, E. T., Renb, Z., Choua, T. W., *Composites Science and Technology*, **2001**. 61
45. Yuan, S.-J., Y. Kong, and F.-S. Li, Mechanical properties of single-walled (5,5) carbon nanotubes with vacancy defects. *Chinese Physics Letters*, **2007**. 24(7):2036.
46. Wang, C. and C. Y. Wang, Geometry and electronic properties of single vacancies in achiral carbon nanotubes. *European Physical Journal B: Condensed Matter and Complex Systems*, **2006**. 54(2):243.
47. Saether, E., Transverse mechanical properties of carbon nanotube crystals. Part II: sensitivity to lattice distortions. *Composites Science and Technology*, **2003**. 63(11):1551.
48. Goze, C., L. Vaccarini, L. Henrard, P. Bernier, E. Hernandez, and A. Rubio, Elastic and mechanical properties of carbon nanotubes. *Synthetic Metals*, **1999**. 103(1-3):2500.
49. Krishnan, A., E. Dujardin, T. W. Ebbesen, P. N. Yanilos, M. M. J. Treacy, and Young's Modulus of Single Walled Nanotubes. *Phys Rev B*, **1998**. 58:14013.
50. Lu, J. P., Elastic Properties of Single and Multilayered Nanotubes. *Physical Chemistry: Solids*, **1997**. 58:1649.
51. Salvétat, J. P., Bonard, J.M., Thomson, N.H., Kulik, A.J., Forro, L., Benoit, W., Zuppiroli, L. , Mechanical properties of carbon nanotubes. *Applied Physics A: Materials Science & Processing*, **1999**. 69:255.
52. Lu, Y., Liaw, P.K. , The Mechanical Properteis of Nanostructured Materials. *Journal of Materials*, **2001**:31.
53. Kelly, B. T., editor, *Physics of Graphite*. 1981, Englewood, N.J.: London: Applied Science. 477.
54. Lau, K. T., Hui, D., The revolutionary creation of new advanced materials-carbon nanotube composites. *Composites Part B: engineering*, **2002**. 33:263.

55. Ruoff, R. S., Lorents, D.C. , Mechanical and Thermal Properteis of Carbon Nanotubes. *Carbon*, **1995**. 3(7):925.
56. Wong, E. W., Sheehan, P.E. , Nanobeam Mechanics: Elasticity, Strength, and Toughness of Nanorods and Nanotubes. *Science*, **1997**. 277(5334):1391.
57. Breuer, O. and U. Sundararaj, Big returns from small fibers: A review of polymer/carbon nanotube composites. *Polymer Composites*, **2004**. 25(6):630.
58. Xie, X.-L., Y.-W. Mai, and X.-P. Zhou, Dispersion and alignment of carbon nanotubes in polymer matrix: A review. *Materials Science & Engineering, R: Reports*, **2005**. R49(4):89.
59. Niyogi, S., M. A. Hamon, H. Hu, B. Zhao, P. Bhowmik, R. Sen, M. E. Itkis, and R. C. Haddon, Chemistry of Single-Walled Carbon Nanotubes. *Accounts of Chemical Research*, **2002**. 35(12):1105.
60. Chae, H. G. and S. Kumar, Polymer/carbon nanotube composites - an overview. *Indian Journal of Fibre & Textile Research*, **2006**. 31(1):29.
61. Girifalco, L. A., Miroslov, H., Lee, R.S., Carbon nanotubes, buckyballs, ropes, and a universal graphitic potential. *Physical Review B*, **2000**. 62(19):13104.
62. Hilding, J., E. A. Grulke, Z. G. Zhang, and F. Lockwood, Dispersion of Carbon Nanotubes in Liquids. *Journal of Dispersion Science and Technology*, **2003**. 24(1):1.
63. Niyogi, S., M. A. Hamon, D. E. Perea, C. B. Kang, B. Zhao, S. K. Pal, A. E. Wyant, M. E. Itkis, and R. C. Haddon, Ultrasonic Dispersions of Single-Walled Carbon Nanotubes. *Journal of Physical Chemistry B*, **2003**. 107(34):8799.
64. Bandyopadhyaya, R., E. E. Nativ-Roth, O. Regev, and R. Yerushalmi-Rozen, Stabilization of Individual Carbon Nanotubes in Aqueous Solutions. *Nano Letters*, **2002**. 2(1):25.
65. Bonard, J. M., Stora, T., Salvétat, J.P, Maier, F., Stockli, T., Duschi, C., Forro, L., deHeer, W.A., Chatelain, A., Purification and size-selection of carbon nanotubes. *Advanced Materials*, **1997**. 9(10):827.
66. Chen, J., H. Liu, W. A. Weimer, M. D. Halls, D. H. Waldek, and G. C. Walker, Noncovalent Engineering of Carbon Nanotube Surfaces by Rigid Functional Conjugated Polymers. *Journal of American Chemical Society*, **2002**. 124(31):9034.

67. Duro, R., C. Souto, J. L. Gomez-Amoza, R. Martinez-Pacheco, and A. Concheiro, Interfacial adsorption of polymers and surfactants: implications for the properties of disperse systems of pharmaceutical interest. *Drug Development and Industrial Pharmacy*, **1999**. 25(7):817.
68. Lu, K. L., et. al, Mechanical Damage of Carbon Nanotubes by Ultrasound. *Carbon*, **1996**. 34:814.
69. Moore, V. C., Strano, M.S., Haroz, E.H., Hauge R.H., Smalley, R.E., Individually Suspended Single-Walled Carbon Nanotubes in Various Surfactants. *Nano Letters*, **2003**. 3(10)
70. O'Connell, M. J., et. al., Reversible water-solubilization of single-walled carbon nanotubes by polymer wrapping. *Chemical Physics Letters*, **2001**. 342:265.
71. Shvartzman-Choen, R., Levi-Kalishman, Y., Nativ-Roth, E., Yerushalmi-Rozen, R., Generic Approach for Dispersing Single-Walled Carbon Nanotubes: The Strength of a Weak Interaction. *Langmuir*, **2004**. 20(15):6085.
72. Shvartzman-Cohen, R., E. Nativ-Roth, E. Baskaran, Y. Levi-Kalishman, I. Szleifer, and R. Yerushalmi-Rozen, Selective Dispersion of Single-Walled Carbon Nanotubes in the Presence of Polymers: the Role of Molecular and Colloidal Length Scales. *Journal of American Chemical Society*, **2004**. 126(45):14850.
73. Strano, M. S., V. C. Moore, M. K. Miller, M. J. Allen, E. H. Haroz, C. Kittrel, R. H. Huage, and R. E. Smalley, The Role of Surfactant Adsorption During Ultrasonication in the Dispersion of Single-Walled Carbon Nanotubes. *Journal of Nanoscience and Nanotechnology*, **2003**. 3(1/2):81.
74. Vigolo, B., A. Penicaud, C. Coulon, R. Sauder, C. Pailler, P. Journet, P. Bernier, and P. Pulin, Macroscopic Fibers and Ribbons of Oriented Carbon Nanotubes. *Science*, **2000**. 290(5495):1331.
75. Zheng, M., A. Jagota, M. S. Strano, A. P. Santos, P. Barone, S. G. Chou, B. A. Diner, M. S. Dresselhaus, R. S. McLean, G. B. Onoa, G. G. Samsonidze, E. D. Semke, M. Usrey, and D. J. Walls, Structure-Based Carbon Nanotube Sorting by Sequence-Dependent DNA Assembly. *Science*, **2003**. 302(5650):1545.
76. Dalton, A. B., Collins, S., Razal, J., Munoz, E., Ebron, V. H., Kim, B. G., Coleman, J. N., Ferraris, J. P., and Baughman, R. H., Continuous carbon nanotube composite fibers: properties, potential applications, and problems. *Journal of Material Chemistry*, **2004**. 14:1.

77. Ding, W., A. Eitan, F. T. Fisher, X. Chen, D. A. Dikin, R. Andrews, L. C. Brinson, L. S. Schadler, and R. S. Ruoff, Direct Observation of Polymer Sheathing in Carbon Nanotube-Polycarbonate Composites. *Nano Letters*, **2003**. 3(11)
78. Fisher, F. T., R. D. Bradshaw, and L. C. Brinson, Fiber waviness in nanotube-reinforced polymer composites-I: Modulus predictions using effective nanotube properties. *Composites Science and Technology*, **2003**. 63(11):1689.
79. Wagner, H. D., Nanotube-polymer adhesion: a mechanics approach. *Chemical Physics Letters*, **2002**. 361
80. Du, J. H., J. Bai, and H. M. Cheng, The present status and key problems of carbon nanotube based polymer composites. *eXPRESS Polymer Letters*, **2007**. 1(5):253.
81. Andrews, R., D. Jacques, A. M. Rao, T. Rantell, and F. Derbyshire, Nanotube Composite Carbon Fibers. *Applied Physics Letters*, **1999**. 75(9):1329.
82. Andrews, R. and M. C. Weisenberger, Carbon nanotube polymer composites. *Current Opinion in Solid State & Materials Science*, **2004**. 8(1):31.
83. Xia, H. and M. Song, Preparation and Characterization of Polyurethane-Carbon Nanotube Composites. *Soft Materials*, **2005**. 1:386.
84. Yerushalmi-Rozen, R. and I. Szleifer, Utilizing polymers for shaping the interfacial behavior of carbon nanotubes. *Soft Matter*, **2006**. 2(1):24.
85. Bao, Q. and C. Pan, Electric field induced growth of well aligned carbon nanotubes from ethanol flames. *Nanotechnology*, **2006**. 17(4):1016.
86. Turano, S. P. and J. Ready, Chemical vapor deposition synthesis of self-aligned carbon nanotube arrays. *Journal of Electronic Materials*, **2006**. 35(2):192.
87. Liu, H., G. Cheng, R. Zheng, Y. Zhao, and C. Liang, Layered growth of aligned carbon nanotubes arrays on silicon wafers. *Journal of Molecular Catalysis A: Chemical*, **2006**. 247(1-2):52.
88. Chen, L. H., J. F. AuBuchon, I. C. Chen, C. Daraio, X. R. Ye, A. Gapin, S. Jin, and C. M. Wang, Growth of aligned carbon nanotubes on carbon microfibers by dc plasma-enhanced chemical vapor deposition. *Applied Physics Letters*, **2006**. 88(3):033103/1.
89. Liu, J., X. Li, A. Schrand, T. Ohashi, and L. Dai, Controlled Syntheses of Aligned Multi-Walled Carbon Nanotubes: Catalyst Particle Size and Density Control via Layer-by-Layer Assembling. *Chemistry of Materials*, **2005**. 17(26):6599.

90. Chen, X. Q., Saito, T., Yamada, H., Matsushige, K. , Aligning single-walled carbon nanotubes with an alternating-current electric field. *Applied Physics Letters*, **2001**. 78(23)
91. Chen, Y., L. Guo, S. Patel, and D. T. Shaw, Aligned Conical Carbon Nanotubes. *Journal of Materials Science*, **2000**. 35(21):5517.
92. Gong, Q.-m., Z. Li, D. Li, X.-d. Bai, and J. Liang, Fabrication and structure: a study of aligned carbon nanotube/carbon nanocomposites. *Solid State Communications*, **2004**. 131(6):399.
93. Ajayan, P. M., O. Stephan, C. Colliex, and D. Trauth, Aligned Carbon Nanotube Arrays Formed by Cutting a Polymer Resin-Nanotube Composite. *Science*, **1994**. 265:1212.
94. Badaire, S., V. Pichot, C. Zakri, P. Poulin, P. Launois, J. Vavro, C. Guthy, M. Chen, and J. E. Fischer, Correlation of properties with preferred orientation in coagulated and stretch-aligned single-wall carbon nanotubes. *Journal of Applied Physics*, **2004**. 96(12):7509.
95. Chen, W. and X. Tao, Self-organizing alignment of carbon nanotubes in thermoplastic polyurethane. *Macromolecular Rapid Communications*, **2005**. 26(22):1763.
96. Gao, J., A. Yu, M. E. Itkis, E. Bekyarova, B. Zhao, S. Niyogi, and R. C. Haddon, Large-Scale Fabrication of Aligned Single-Walled Carbon Nanotube Array and Hierarchical Single-Walled Carbon Nanotube Assembly. *Journal of the American Chemical Society*, **2004**. 126(51):16698.
97. Garmestani, H., Al-Haik, M.S.; Dahmen, K., Tannenbaum, R., Li, D.S., Sablin, S.S., Hussaini, M. Y., Polymer-Mediated Alignment of Carbon Nanotubes under High Magnetic Fields. *Advanced Materials*, **2003**. 15(22)
98. Hagenmueller, R., Gommans, H.H., Rinzler, A.G., Fischer, J.E., Winey, K.I., Aligned Single-walled carbon nanotubes in composites by melt processing methods. *Chemical Physics Letters*, **2000**. 330:219.
99. Jin, L., C. Bower, and O. Zhou, Alignment of Carbon Nanotubes in a Polymer Matrix by Mechanical Stretching. *Applied Physics Letters*, **1998**. 73(9):1197.
100. Kim, Y. A., T. Hayashi, M. Endo, Y. Gotoh, N. Wada, and J. Seiyama, Fabrication of aligned carbon nanotube-filled rubber composite. *Scripta Materialia*, **2005**. 54(1):31.

101. Poetschke, P., H. Bruenig, A. Janke, D. Fischer, and D. Jehnichen, Orientation of multiwalled carbon nanotubes in composites with polycarbonate by melt spinning. *Polymer*, **2005**. 46(23):10355.
102. Rarvikar, N. R., Schadler, L. S., Vijaaraghavan, A., Zhao, Y., Wei, B., Ajayan, P. M., Synthesis and characterization of thickness-aligned carbon nanotube-polymer composite films. *Chemical Materials*, **2005**. 17:974.
103. Smith, B. W., Z. Benes, D. E. Luzzi, J. E. Fischer, D. A. Walters, M. J. Casavant, J. Schmidt, and R. E. Smalley, Structural Anisotropy of Magnetically Aligned Single Walled Carbon Nanotube Films. *Applied Physics Letters*, **2000**. 77(5):663.
104. Spotnitz, M. E., D. Ryan, and H. A. Stone, Dip coating for the alignment of carbon nanotubes on curved surfaces. *Journal of Materials Chemistry*, **2004**. 14(8):1299.
105. Wang, T., M. Wang, X. Hu, X. Qu, F. Zhao, and S. Dong, Parallel Alignment of Carbon Nanotubes Induced with Inorganic Molecules. *Langmuir*, **2005**. 21(26):12068.
106. Xiao, Y., Z. M. Li, X. H. Yan, Y. Zhang, Y. L. Mao, and Y. R. Yang, Curvature effect on the radial breathing modes of single-walled carbon nanotubes. *Physical Review B: Condensed Matter and Materials Physics*, **2005**. 71(23):233405/1.
107. Kumar, M. S., Kim, T.H., Lee, S.H., Song, S.M., Yang, J.W., Nahm, K.S., Suh, E.K. , Influence of electric field type on the assembly of single walled carbon nanotubes. *Chemical Physics Letters*, **2003**. 383:235.
108. Martin, C. A., J. K. W. Sandler, A. H. Windle, M.-K. Schwarz, W. Bauhofer, K. Schulte, and M. S. P. Shaffer, Electric field-induced aligned multi-wall carbon nanotube networks in epoxy composites. *Polymer*, **2005**. 46:877.
109. Thostenson, E. T. and T.-W. Chou, Aligned multi-walled carbon nanotube-reinforced composites: processing and mechanical characterization. *Journal of Applied Physics D: Applied Physics*, **2002**. 35:L77.
110. Valentini, L., I. Armentano, J. M. Kenny, L. Lozzi, and S. Santucci, Pulsed plasma-induced alignment of carbon nanotubes. *Materials Letters*, **2003**. 57:3699.
111. Fry, D., B. Langhorst, H. Kim, E. Grulke, H. Wang, and E. K. Hobbie, Anisotropy of Sheared Carbon-Nanotube Suspensions. *Physical Review Letters*, **2005**. 95(3):038304/1.
112. Fry, D., B. Langhorst, H. Wang, M. L. Becker, B. J. Bauer, E. A. Grulke, and E. K. Hobbie, Rheo-optical studies of carbon nanotube suspensions. *Journal of Chemical Physics*, **2006**. 124(5):054703/1.

113. Wei, C., L. Dai, A. Roy, and T. B. Tolle, Multifunctional chemical vapor sensors of aligned carbon nanotube and polymer composites. *Journal of the American Chemical Society*, **2006**. 128(5):1412.
114. Ajayan, P. M., Schadler, L. S., Giannaris, C., Rubio, A., Single-Walled Carbon Nanotube-Polymer Composites: Strength and Weakness. *Advanced Materials*, **2000**. 12(10):750.
115. Chen, J., R. Ramasubramaniam, C. Xue, and H. Liu, A versatile, molecular engineering approach to simultaneously enhanced, multifunctional carbon nanotube-polymer composites. *Advanced Functional Materials*, **2006**. 16(1):114.
116. Curran, S., A. P. Davey, J. Coleman, A. Dalton, B. McCarthy, S. Maier, A. Drury, D. Gray, M. Brennan, K. Ryder, M. L. de La Chapelle, C. Journet, P. Bernier, H. J. Byrne, D. Carroll, P. M. Ajayan, S. Lefrant, and W. Blau, Evolution and evaluation of the polymer/nanotube composite. *Synthetic Metals*, **1999**. 103(1-3):2559.
117. Li, F., Cheng, H. M., Bai, S., Su, G., Tensile Strength of Single-Walled Carbon Nanotubes directly measured from their macroscopic ropes. *Applied Physics Letters*, **2000**. 77(20):3161.
118. Baughman, R. H., A. A. Zakhidov, and W. A. de Heer, Carbon nanotubes-the route toward applications. *Science (Washington, DC, United States)*, **2002**. 297(5582):787.
119. Kumar, S., T. D. Dang, F. E. Arnold, A. R. Bhattacharyya, B. G. Min, X. Zhang, R. A. Vaia, C. Park, W. W. Adams, R. H. Hauge, R. E. Smalley, S. Ramesh, and P. A. Willis, Synthesis, Structure, and Properties of PBO/SWNT Composites. *Macromolecules*, **2002**. 35(24):9039.
120. Chae, H. G., M. L. Minus, and S. Kumar, Oriented and exfoliated single wall carbon nanotubes in polyacrylonitrile. *Polymer*, **2006**. 47(10):3494.
121. Kim, G. M., G. H. Michler, and P. Poetschke, Deformation processes of ultrahigh porous multiwalled carbon nanotubes/polycarbonate composite fibers prepared by electrospinning. *Polymer*, **2005**. 46(18):7346.
122. Rodriguez, F., C. Choen, C. K. Ober, and L. A. Archer, *Principles of Polymer Systems*. 5th ed. 2003, New York, NY: Taylor & Francis Books, Inc. 760.
123. Rosen, S. L., *Fundamental Principles of Polymeric Materials*. 2 ed. 1993, New York: Wiley-Interscience 420.

124. Advani, S. G. and Z. Fan, Effect of dispersion state on the rheology of Multi-walled Carbon nanotube suspensions in shear flow. *AIP Conference Proceedings*, **2004**. 712(Pt. 2, Materials Processing and Design):1619.
125. Lin-Gibson, S., G. Schmidt, H. Kim, C. C. Han, and E. K. Hobbie, Shear-induced meso structure in nano platelet-polymer networks. *Journal of Chemical Physics*, **2003**. 119(15):8080.
126. Wang, H., G. T. Christopherson, Z. Y. Xu, L. Porcar, D. L. Ho, D. Fry, and E. K. Hobbie, Shear-SANS study of single-walled carbon nanotube suspensions. *Chemical Physics Letters*, **2005**. 416(1-3):182.
127. Al-Haik, M. S., H. Garmestani, D. S. Li, M. Y. Hussaini, S. S. Sablin, R. Tannenbaum, and K. Dahmen, Mechanical Properties of Magnetically Oriented Epoxy. *Journal of Polymer Science: Part B*, **2004**. 42:1586.
128. Clayton, L. M., T. G. Gerasimov, M. Cinke, M. Meyyappan, and J. P. Harmon, Dispersion of single-walled carbon nanotubes in a non-polar polymer, poly(4-methyl-1-pentene). *Journal of Nanoscience and Nanotechnology*, **2006**. 6(8):2520.
129. Frogley, M. D., D. Ravich, and H. D. Wagner, Mechanical properties of carbon nanoparticle-reinforced elastomers. *Composites Science and Technology*, **2003**. 63:1647.
130. Frogley, M. D., Q. Zhao, and H. D. Wagner, Polarized resonance Raman spectroscopy of single-wall carbon nanotubes within a polymer under strain. *Physics Review B*, **2002**. 65(11):113413.
131. Cantournet, S., M. C. Boyce, and A. H. Tsou, Micromechanics and macromechanics of carbon nanotube-enhanced elastomers. *Journal of the Mechanics and Physics of Solids*, **2007**. 55(6):1321.
132. Coleman, J. N., M. Cadek, K. P. Ryan, A. Fonseca, J. B. Nagy, W. J. Blau, and M. S. Ferreira, Reinforcement of polymers with carbon nanotubes. The role of an ordered polymer interfacial region. Experiment and modeling. *Polymer*, **2006**. 47(26):8556.
133. Ha, Y.-H., Y. Kwon, T. Breiner, E. P. Chan, T. Tzianetopoulou, R. E. Cohen, M. C. Boyce, and E. L. Thomas, An Orientationally Ordered Hierarchical Exfoliated Clay-Block Copolymer Nanocomposite. *Macromolecules*, **2005**. 38(12):5170.
134. Camponeschi, E., R. Vance, M. Al-Haik, H. Garmestani, and R. Tannenbaum, Properties of epoxy-based composites reinforced with carbon nanotubes aligned in a magnetic field. *Carbon*, **2007**. 45(10):2037.

135. Kimura, T., H. Ago, M. Tobita, S. Ohshima, M. Kyotani, and M. Yumura, Polymer composites of Carbon Nanotubes Aligned by a Magnetic Field. *Advanced Materials*, **2002**. 14(19):1380.
136. Camponeschi, E., M. Minus, H. Garmestani, and R. Tannenbaum, Effects of the Different Dispersing Agents on the Polymer-Carbon Nanotubes Composite Properties. *Acta Materialia*, **2007**. submitted
137. Campbell, D., Pethrick, R.A.; White, J.R., *Polymer characterization: physical techniques*. 2000 Cheltenham, U.K: Stanley Thornes.
138. White, J. R., D. Campbell, and R. A. Pethrick, *Polymer Characterization: Physical Techniques*. 2000: Stanley Thornes Ltd. 481.
139. Williams, D. B. and C. B. Carter, *Transmission Electron Microscopy: A Textbook for Materials Science*. 1996, New York: Plenum Press. 729.
140. Loader, J., *Basic Laser Raman Spectroscopy*. 1970, [Philadelphia] Heyden Sadtler Research Laboratories 105.
141. Zhao, Q. and H. D. Wagner, Raman spectroscopy of carbon-nanotube-based composites. *Philosophical Transactions of the Royal Society of London*, **2004**. 362(1824):2407.
142. Cooper, C. A., R. J. Young, and M. Halsall, Investigation into the deformation of carbon nanotubes and their composites through the use of Raman spectroscopy. *Composites: Part A*, **2001**. 32:401.
143. Wood, J. R., Zhao, Q., Wagner, H. D., Orientation of carbon nanotubes in polymers and its detection by Raman Spectroscopy. *Composites: Part A*, **2001**. 32:391.
144. Dresselhaus, M. S., G. Dresselhaus, A. Jorio, A. G. Souza Filho, and R. Saito, Raman spectroscopy on isolated single wall carbon nanotubes. *Carbon*, **2002**. 40(12):2043.
145. Sauvajol, J. L., E. Anglaret, S. Rols, and L. Alvarez, Phonons in single wall carbon nanotube bundles. *Carbon*, **2002**. 40(10):1697.
146. Simon, G. P. and Editor, *Polymer Characterization Techniques and Their Application to Blends*. 2003. 516 pp.
147. Brown, G. G., *DMA 2980 Technical Reference User's Manual*. 2002, TA Instruments, Inc.
148. Schmitz, J. V., *Testing of Polymers*. Vol. 1. 1965, New York: Interscience. 479.

149. Schmitz, J. V., *Testing of Polymers*. Vol. 3. 1965, New York: Interscience. 379.
150. Cullity, B. D. and S. R. Stock, *Elements of X-ray Diffraction*. 2001, New Jersey: Prentice Hall. 555.
151. Ewald, P. P., ed. *Fifty Years of Electron Diffraction*. 1962, Springer. 733.
152. Snyder, R. L., J. Fiala, and H. J. Bunge, *Defect and Microstructure Analysis by Diffraction*. 1999: Oxford University Press. 767.
153. Brumberger, H., ed. *Modern Aspects of Small-Angle Scattering*. 1995, Kluwer: Boston.
154. Feigin, L. A. and D. I. Syergun, *Structure Analysis by Small-Angle X-ray and Neutron Scattering*. 1987, New York: Plenum Press.
155. Debeye, P., H. R. Anderson, and H. Brumberger, Scattering by an Inhomogeneous Solid II: the Correlation Function and It's Application. *Journal of Applied Physics*, **1957**. 28:679.
156. Frische, H. L. and F. H. Stiltlinger, Contribution to the Statistical Geometric Basis of Radiation Scattering. *Journal of Chemical Physics*, **1963**. 28:2200.
157. Glatter, O. and O. Kratky, *Small Angle X-ray Scattering*. 1982, New York: Academic Press. 594.
158. Gunier, A. and G. Gournet, *Small Angle Scattering of X-Rays*. 1955, New York: John Wiley.
159. Beaucage, G., Approximations leading to a unified exponential/power-law approach to small-angle scattering. *Journal of Applied Crystallography*, **1995**. 28(6):717.
160. Beaucage, G., Small-angle scattering from polymeric mass fractals of arbitrary mass-fractal dimension. *Journal of Applied Crystallography*, **1996**. 29(2):134.
161. Beaucage, G., H. K. Kammler, and S. E. Pratsinis, Particle size distributions from small-angle scattering using global scattering functions. *Journal of Applied Crystallography*, **2004**. 37(4):523.
162. Tannenbaum, R., M. Zubris, K. David, D. Ciprari, K. Jacob, I. Jasiuk, and N. Dan, FTIR Characterization of the Reactive Interface of Cobalt Oxide Nanoparticles Embedded in Polymeric Matrices. *Journal of Physical Chemistry B*, **2006**. 110(5):2227.

163. Pham, J. Q., C. A. Mitchell, J. L. Bahr, J. M. Tour, R. Krishnamoorti, and P. F. Green, Glass Transition of Polymer/SWNT Films. *Journal of Polymer Science: Part B*, **2003**. 41
164. Kovacs, J. Z., B. S. Velagala, K. Schulte, and W. Bauhofer, Two precolation thresholds in carbon nanotube epoxy composites. *Composites Science and Technology*, **2007**. 67(5):922.
165. Shenogina, N., S. Shenogin, L. Xue, and P. Keblinski, On the lack of thermal percolation in carbon nanotube composites. *Applied Physics Letters*, **2005**. 87(13)
166. Ha, M. L. P., B. P. Grady, G. Lolli, D. E. Resasco, and W. T. Ford, Composites of single-walled carbon nanotubes and styrene-isoprene copolymer latices. *Macromolecular Chemistry and Physics*, **2007**. 208(5):446.
167. Gong, X., J. Liu, S. Baskaran, R. D. Voise, and J. S. Young, Surfactant-Assisted Processing of Carbon Nanotube/Polymer Composites. *Chemistry of Materials*, **2000**. 12(4):4.
168. Wei, C., D. Srivastava, and K. Cho, Thermal expansion and diffusion coefficients of carbon nanotube-polymer composites. *Nano Letters*, **2002**. 2(6)
169. Wood, J. R., M. D. Frogley, E. R. Meurs, A. D. Prins, T. Peijs, D. J. Dunstan, and H. D. Wagner, Mechanical Response of Carbon Nanotubes under Molecular and Macroscopic Pressures. *Journal of Physical Chemistry B*, **1999**. 103(47):10388.
170. Zhao, Q., J. R. Wood, and H. D. Wagner, Using carbon nanotubes to detect polymer transitions. *Journal of Polymer Science, Part B: Polymer Physics*, **2001**. 39(13):1492.
171. Barrau, S., P. Demont, C. Maraval, A. Bernes, and C. Lacabanne, Glass transition temperature depression at the percolation threshold in carbon nanotube-epoxy resin and polypyrrole-epoxy resin composites. *Macromolecular Rapid Communications*, **2005**. 26(5):390.
172. Chen, H., O. Jacobs, W. Wu, G. Ruediger, and B. Schaedel, Effect of dispersion method on tribological properties of carbon nanotube reinforced epoxy resin composites. *Polymer Testing*, **2007**. 26(3):351.
173. Gojny, F. H. and K. Schulte, Functionalization effect on the thermo-mechanical behavior of multi-wall carbon nanotube/epoxy-composites. *Composites Science and Technology*, **2004**. 64(15):2303.

174. McLean, S. C., H. Lioe, L. Meagher, V. S. J. Craig, and M. L. Gee, Atomic Force Microscopy Study of the Interaction between Adsorbed Poly(ethylene oxide) Layers: Effects of Surface Modification and Approach Velocity. *Langmuir*, **2005**. 21(6):2199.
175. Riccardi, C. C., J. Borrajo, L. Meynie, F. Fenouillot, and J.-P. Pascault, Thermodynamic analysis of the phase separation during the polymerization of a thermoset system into a thermoplastic matrix. Part II. Prediction of the phase composition and the volume fraction of the dispersed phase. *Journal of Polymer Science, Part B: Polymer Physics*, **2004**. 42(8):1361.
176. Riccardi, C. C., J. Borrajo, L. Meynie, F. Fenouillot, and J.-P. Pascault, Thermodynamic analysis of the phase separation during the polymerization of a thermoset system into a thermoplastic matrix. Part I. Effect of the composition on the cloud-point curves. *Journal of Polymer Science, Part B: Polymer Physics*, **2004**. 42(8):1351.
177. Zucchi, I. A., M. J. Galante, J. Borrajo, and R. J. J. Williams, A model system for the thermodynamic analysis of reaction-induced phase separation: solutions of polystyrene in bifunctional epoxy/amine monomers. *Macromolecular Chemistry and Physics*, **2004**. 205(5):676.
178. Bund, A., H. Chmiel, and G. Schwitzgebel, Determination of the complex shear modulus of polymer solutions with piezoelectric resonators. . *Physical Chemistry Chemical Physics*, **1999**. 1(17):3933.
179. Coleman, J. N., M. Cadek, K. P. Ryan, A. Fonseca, J. B. Nagy, W. J. Blau, and F. M. S, Reinforcement of polymers with carbon nanotubes. The role of an ordered polymer interfacial region. Experiment and modeling. *Polymer*, **2006**. 47(26):8556.
180. Coleman, J. N., U. Khan, W. J. Blau, and Y. K. Gun'ko, Small but strong: A review of the mechanical properties of carbon nanotube-polymer composites. *Carbon*, **2006**. 44(9):1624.
181. Fidelus, J. D., E. Wiesel, F. H. Gojny, K. Schulte, and H. D. Wagner, Thermo-mechanical properties of randomly oriented carbon/epoxy nanocomposites. *Composites Part A: Applied Science and Manufacturing*, **2005**. 36(11):1555.
182. Gall, K., M. L. Dunn, Y. Liu, G. Stefanic, and D. Balzar, Internal stress storage in shape memory polymer nanocomposites. *Applied Physics Letters*, **2004**. 85(2):290.
183. Xiao, J. R. and J. W. Gillespie, Nanomechanics of single-walled carbon nanotubes as composite reinforcement. *Polymer Engineer and Science*, **2006**. 46(8):1051.

184. Jefferson, G., H. Garmestani, R. Tannenbaum, A. Gokhale, and E. Tadd, Two-point probability distribution function analysis of Co-polymer nano-composites. *International Journal of Plasticity*, **2004**. 21(1):185.
185. Lin, S., Garmestani, H., Statistical continuum mechanics analysis of an elastic two-isotropic-phase composite material. *Composites Part B: engineering*, **2000**. 31:39.
186. Hernandez, J. J., M. C. Garcia-Gutierrez, A. Nogales, D. R. Rueda, A. Sanz, I. Sics, B. S. Hsiao, Z. Roslaniec, G. Broza, and T. A. Ezquerro, Deformation behaviour during cold drawing of nanocomposites based on single wall carbon nanotubes and poly(ether ester) copolymers. *Polymer*, **2007**. 48(11):3286.
187. Wang, B. N., R. D. Bennett, E. Verploegen, A. J. Hart, and R. E. Cohen, Quantitative Characterization of the Morphology of Multiwall Carbon Nanotube Films by Small-Angle X-ray Scattering. *Journal of Physical Chemistry C*, **2007**. 111(16):5859.
188. Mitchel, C. A., Bahr, J.L., Arepalli, S., Tour, J.M., Krishnamoorti, R. , Dispersion of Functionalized Carbon Nanotubes in Polystyrene. *Macromolecules*, **2002**. 35:8825.
189. Yamamoto, K., S. Akita, and Y. Nakayama, Orientation of Carbon Nanotubes Using Electrophoresis. *Journal of Applied Physics (Jpn)*, **1996**. 35(7B):L917.
190. Kimra, T., Hiroki, A., Tobitqa, M., Ohshima, S., Kyotani, M., Yumura, M., Polymer composites of Carbon Nanotubes Aligned by a Magnetic Field. *Advanced Materials*, **2002**. 14(19)
191. Correa-Duarte, M. A., M. Grzelczak, V. Salgueirino-Maceira, M. Giersig, L. M. Liz-Marzan, M. Farle, K. Sieradzki, and R. Diaz, Alignment of Carbon Nanotubes under Low Magnetic Fields through Attachment of Magnetic Nanoparticles. *Journal of Physical Chemistry B*, **2005**. 109(41):19060.
192. Shan, Y. and L. Gao, Fe₃O₄-modified carbon nanotubes: a facile and efficient method to orientate alignment in magnetic field. *Chemistry Letters*, **2006**. 35(10):1092.
193. Shi, D., P. He, J. Lian, X. Chaud, S. L. Bud'ko, E. Beaunon, L. M. Wang, R. C. Ewing, and R. Tournier, Magnetic alignment of carbon nanofibers in polymer composites and anisotropy of mechanical properties. *Journal of Applied Physics*, **2005**. 97(6):064312/1.
194. Dror, Y., Salalha, W., Khalfin, R. L., Choen, Y., Yarin, A. L., Zussman, E. , Carbon Nanotube Embedded in Oriented Polymer Nanofibers by Electrospinning. *Langmuir*, **2003**. 19:7012.

195. Ko, F. e. A., Electrospinning of Continuous Carbon Nanotube-Filled Nanofiber Yarns. *Advanced Materials*, **2003**. 15(14):1161.
196. Salalha, W., Dror, Y., Khalfin, R. L., Choen, Y., Yarin, A. L., Zussman, E. , Single-Walled Carbon Nanotubes Embedded in Oriented Polymeric Nanotubers by Electrospinning. *Langmuir*, **2004**. 20:9852.
197. Croce, V., T. Cosgrove, C. A. Dreiss, S. king, G. Maitland, and T. Hughes, Giant Micellar Worms under Shear: A Rheological Study Using SANS. *Langmuir*, **2005**. 21(15):6762.
198. Camponeschi, E., B. Florkowski, R. Vance, G. Garrett, H. Garmestani, and R. Tannenbaum, Uniform Directional Alignment of Single-Walled Carbon Nanotubes in Viscous Polymer Flow. *Langmuir*, **2006**. 22(4):1858.
199. Shvartzman-Choen, R., Nativ-Roth, E.,Baskaran, E., Levi-Kalishman, Y., Szleifer, I., Yerushalmi-Rozen, R., *Journal of American Chemical Society*, **2004**. 126(45)
200. Bhattacharyya, A., R., T. V. Sreekumar, T. Liu, S. Kumar, L. M. Ericson, R. H. Hauge, and R. E. Smalley, Crystallization and Orientation Studies in Polypropylene/Single Walled Carbon Nanotube Composites. *Polymer*, **2003**. 44(8):2373.
201. Duesberg, G. S., I. Loa, M. Burghard, S. K., and S. Roth, Polarized Raman Spectroscopy on Isolated Single-Walled Carbon Nanotubes. *Physics Review Letters*, **2000**. 85(25):5436.
202. Liu, T., Kumar, S., Quantitative characterization of SWNT orientation by polarized Raman spectroscopy. *Chemical Physics Letters*, **2003**. 378:257.
203. Cooper, C. A., D. Ravich, D. Lips, J. Mayer, and H. D. Wagner, Distribution and alignment of carbon nanotubes and nanofibrils in a polymer matrix. *Composites Science and Technology*, **2002**. 62(7-8):1105.
204. Chen, W. and X. Tao, Production and characterization of polymer nanocomposite with aligned single wall carbon nanotubes. *Applied Surface Science*, **2006**. 252(10):3547.
205. Donnet, J. B., Bansal, R. C., Wang, M. J., *Carbon Black: Science and Technology*. 1993, New York: Marcel Dekker. 449.
206. Ebert, F. and T. Thurn-Albrecht, Controlling the orientation of semicrystalline polymers by crystallization in magnetic fields. *Macromolecules*, **2003**. 36(23):8685.

207. Kawai, T. and T. Kimura, Magnetic orientation of isotactic polypropylene. *Polymer*, **1999**. 41(1):155.
208. Kimura, T., T. Kawai, and Y. Sakamoto, Magnetic orientation of poly(ethylene terephthalate). *Polymer*, **1999**. 41(2):809.
209. Sata, H., T. Kimura, S. Ogawa, M. Yamato, and E. Ito, Magnetic orientation of poly(ethylene-2,6-naphthalate). *Polymer*, **1996**. 37(10):1879.
210. Brummer, R., F. Hetzel, and C. Harder, Correlation of polymer properties with dynamic mechanical measurements. *Applied Rheology*, **1997**. 7(4):173.
211. Lapique, F., P. Meakin, J. Feder, and T. Jossang, Relationships between microstructure, fracture-surface morphology, and mechanical properties in ethylene and propylene polymers and copolymers. *Journal of Applied Polymer Science*, **2000**. 77(11):2370.
212. Watanabe, H. and T. Inoue, Conformational dynamics of rouse chains during creep/recovery processes: a review. *Journal of Physics: Condensed Matter*, **2005**. 17(19):R607.
213. Melick, H. v., A. v. Dijken, J. D. Toonder, L. Govaert, and H. Meijer, Near-surface mechanical properties of amorphous polymers. *Philosophical Magazine A: Physics of Condensed Matter: Structure, Defects and Mechanical Properties*, **2002**. 82(10):2093.
214. Pu, Y., h. White, M. H. Rafailovich, J. Sokolov, S. A. Schwarz, A. Dhinojwala, D. Agra, and S. Kumar, Chain orientation and its effect on mobility at a rubbed surface. *Macromolecules*, **2001**. 34(14):4972.
215. Beranger, S., M. H. Fortier, D. Baril, and M. B. Armand, Inducing order in polymer *Solid State Ionics*, **2002**. 148(3-4):437.'
216. Ji, Y., B. Q. Li, S. R. Ge, J. C. Sokolov, and M. H. Rafailovich, Structure and nanomechanical characterization of electrospun PS/clay nanocomposite fibers. *Langmuir*, **2006**. 22(3):1321.
217. Leolukman, M. and S. H. Kim, Effect of rubbing-induced polymer chain alignment on adhesion and friction of glassy polystyrene surfaces. *Langmuir*, **2005**. 21(2)
218. Brekner, M. J., H. A. Schneider, and H. J. Cantow, Approach to the composition dependence of the glass transition temperature of compatible polymer blends. 2. The effect of local chain orientation. *Makromolekulare Chemie*, **1988**. 189(9)

219. Christianen, P., I. O. Shklyarevskiy, M. I. Boamfa, and J. C. Maan, Alignment of molecular materials in high magnetic fields. *Physica B: Condensed Matter*, **2004**. 346-347
220. Eberle, R., S. H. Anders, K. Weishaupt, and M. Pietralla, Anisotropic effects of the glass transition in oriented polyethylene. *Europhysics Letters*, **1999**. 43(2):201.
221. Ekanayake, P., H. Menge, and H. Schneider, Chain orientation and dynamics of filled and unfilled poly(butadiene) networks studied by applying nuclear spin correlation of residual quadrupolar interaction. *Polymer Bulletin*, **2001**. 47(3-4):383.
222. Feldstein, M. M. and D. F. Bairamov, Effects of chains orientation, free volume and interaction on glass transition in poly(N-vinyl pyrrolidone) - poly(ethylene glycol) blends involving a stoichiometric hydrogen-bonded network complex. *Polymer Material Science and Engineer*, **2000**. 82:365.
223. Grigorova, T., S. Pispas, N. Hadjichristidis, and T. Thurn-Albrecht, Magnetic field induced orientation in diblock copolymers with one crystallizable block. *Macromolecules*, **2005**. 38(17):7430.
224. Lincoln, D. M. and E. P. Douglas, Control of orientation in liquid crystalline epoxies via magnetic field processing. *Polymer Engineering and Science*, **1999**. 39(10):1903.
225. Sekkat, Z., A. Knoesen, V. Y. Lee, and R. D. Miller, Influence of the polymer structure on the achievement of polar orientation in high glass transition temperature nonlinear optical polyimides by photo-assisted poling. *Journal of Polymer Science, Part B: Polymer Physics*, **1998**. 36(10):1669.
226. Sprunt, S., G. Nounesis, J. Naciri, B. R. Ratna, and R. Shashidhar, Stability of magnetic field-induced dipolar order in a ferroelectric side-chain liquid crystal polymer. *Applied Physics Letters*, **1994**. 65(21):2681.
227. Stepanov, A. L., S. N. Abdullin, V. Y. Petukhov, Y. N. Osin, R. I. Khaibullin, and B. Khaibullin, Formation of metal-polymer composites by ion implantation. *Philosophical Magazine A: Physics of Condensed Matter: Structure, Defects and Mechanical Properties*, **2000**. 80(1):23.
228. Takeno, H., M. Kobayashi, and T. Aikawa, Localized Cooperative Molecular Motion in Miscible Polymer Mixtures with Large Difference in Glass-Transition Temperatures. *Macromolecules*, **2006**. 39(6):2183.

229. Volegyoa, I. A., Y. K. Godovsky, and M. Soliman, Glass transition of undrawn and drawn copolyetherester thermoplastic elastomers. *International Journal of Polymer Materials*, **2003**. 52(6)
230. Longieras, N., M. Sebban, P. Palmas, A. Rivaton, and J. L. Gardette, Multiscale approach to investigate the radiochemical degradation of epoxy resins under high-energy electron-beam irradiation. *ournal of Polymer Science, Part A: Polymer Chemistry*, **2005**. 44(2):865.
231. Choi, E. S., et. al., Enhancement of thermal and electrical properties of carbon nanotube polymer composites by magnetic field proecssing. *Journal of Applied Physics*, **2003**. 94(9)
232. Sircar, A. K., M. L. Galaska, S. Rodrigues, and R. P. Chartoff, Glass transition of elastomers using thermal analysis techniques. *Rubber Chemistry and Technology*, **1999**. 72(3):513.
233. Cronin, S. B., A. K. Swan, M. S. unlu, B. B. Goldberg, M. S. Dresselhaus, and M. Tinkham, Measuring the uniaxial strain of individual single-wall carbon nanotubes: Resonance Raman spectra of atomic-force-microscope modified single-wall nanotubes. *Physical Review Letters*, **2004**. 93(16):167401.
234. Souza, A. G., N. Kobayashi, J. Jiang, A. Gruneis, R. Saito, S. B. Cronin, J. Mendes, G. G. Samsonidze, G. G. Dresselhaus, and M. S. Dresselhaus, Strain-induced interference effects on the resonance Raman cross section of carbon nanotubes. *Physical Review Letters*, **2005**. 95(21):217403.
235. Islam, M. F., D. E. Milkie, C. L. Kane, A. G. Yodh, and H. M. Kikkawa, Direct measurement of the polarized optical absorption cross section of single-wall carbon nanotubes. *Physical Review Letters*, **2004**. 93(3):037404.
236. Pal, A. K., R. K. Roy, S. K. Mandel, S. Gupta, and B. Deb, Electrodeposited carbon nanotube thin films. *Thin Solid Films*, **2005**. 476(2):288.
237. Zhao, Q. and H. D. Wagner, Two-dimensional strain mapping in model fiber-polymer composites using nanotube Raman sensing. *Composites Part A: Applied Science and Manufacturing* **2003**. 34(11):1219.
238. Gash, A. E., J. H. J. Satcher, and R. L. Simpson, Strong Akaganeite Aerogel Monoliths Using Epoxides: Synthesis and Characterization. . *Chemistry of Materials s*, **2003**. 15(17):3268.

239. Khomutov, G. B., V. V. Kislov, S. P. Gainutdinov, A. Y. Gubin, S. A. Obydenov, A. N. Pavlov, E. S. Sergeez-Cherenkov, A. L. Soldatov, A. S. Tolstikhina, and A. S. Trifonov, The design, fabrication and characterization of controlled-morphology nanomaterials and functional planar molecular nanocluster-based nanostructures. . *Surface Science*, **2003**. 532-535:287.
240. Koutzarova, T., S. Kolev, C. Ghelev, D. Paneva, and I. Nedkov, Microstructural study and size control of iron oxide nanoparticles produced by microemulsion technique. *Physica Status Solidi C: Current Topics in Solid State Physics*, **2006**. 3(5):1302.
241. Kuykendall, T., P. J. Pauzauskie, Y. Zhang, J. Goldberger, D. Sirbully, J. Denlinger, and P. Yang, Crystallographic alignment of high-density gallium nitride nanowire arrays. *Nature of Materials*, **2004**. 3(8):524.
242. Liu, S., X. Wei, M. Chu, J. Peng, and Y. Xu, Synthesis and characterization of iron oxide/polymer composite nanoparticles with pendent functional groups. *Colloids and Surfaces, B: Biointerfaces*, **2006**. 51(2):101.
243. Lovely, G. R., A. P. Brown, R. Brydson, A. I. Kirkland, R. R. Meyer, L. Y. Chang, D. A. Jefferson, M. Falke, and A. Bleloch, HREM of the {111} surfaces of iron oxide nanoparticles. *Micron*, **2006**. 37(5):389.
244. Nassar, N. and M. Husein, Preparation of iron oxide nanoparticles from FeCl₃ solid powder using microemulsions. *Physica Status Solidi A: Applications and Materials Science*, **2006**. 203(6):1324.
245. Park, Y. K., E. H. Tadd, M. Zubris, and R. Tannenbaum, Size-controlled synthesis of alumina nanoparticles from aluminum alkoxides. *Materials Research Bulletin*, **2005**. 40(9):1506.
246. Walker, J. D. and R. Tannenbaum, Characterization of the Sol-Gel Formation of Iron(III) Oxide/Hydroxide Nanonetworks from Weak Base Molecules. *Chemistry of Materials*, **2006**. 18:4801.
247. Can, M. M., S. Ozcan, and T. Firat, Magnetic behaviour of iron nanoparticles passivated by oxidation. *Physica Status Solidi C: Current Topics in Solid State Physics*, **2006**. 3(5):1271.
248. Du, G., Z. Liu, X. Xia, L. Jia, Q. Chu, and S. Zhang, Functionalization of Fe₃O₄ magnetic nanoparticles. *Nanoscience*, **2006**. 11(1):49.
249. Park, C.-D., D. Magana, and A. E. Stiegman, High-Quality Fe and g-Fe₂O₃ Magnetic Thin Films from an Epoxide-Catalyzed Sol-Gel Process. . *Chemistry of Materials*, **2007**. 19:677

250. Tartaj, P., M. P. Morales, S.-V. Verdaguer, T.-G. Carreno, and C. J. Serna, The preparation of magnetic nanoparticles for applications in biomedicine. . *Journal of Physics D: Applied Physics*, **2003**. 36:R182.
251. Walker, J. D. and R. Tannenbaum, Characterization of the Sol-Gel Formation of Iron(III) Oxide/Hydroxide Nanonetworks from Weak Base Molecules. *Chemistry of Materials*, **2006**. 18(20):4793.
252. Walker, J. D. and R. Tannenbaum, Characterization of the Sol-Gel Formation of Iron(III) Oxide/Hydroxide Nanonetworks from Weak Base Molecules. *Chem. Mater.*, **2006**
253. Gash, A. E., T. M. Tillotson, J. H. Satcher, Jr., J. F. Poco, L. W. Hrubesh, and R. L. Simpson, Use of Epoxides in the Sol-Gel Synthesis of Porous Iron(III) Oxide Monoliths from Fe(III) Salts. *Chemistry of Materials*, **2001**. 13(3)
254. Battisha, I. K., H. H. Afify, and I. M. Hamada, Structural and magnetic susceptibility studies of SiO₂:Fe₂O₃ nanocomposites prepared by sol-gel technique. *Journal of Magnetism and Magnetic Materials*, **2005**. 292:440.
255. Camponeschi, E., J. Walker, H. Garmestani, and R. Tannenbaum, Surfactant Effects on the Particle Size of Iron (III) Oxides Formed by Sol-Gel Synthesis. *Journal of Non-Crystalline Solids*, **2007**
256. Camponeschi, E., B. Florkowski, R. Vance, G. Garrett, H. Garmestani, and R. Tannenbaum, Uniform Directional Alignment of Single-Walled Carbon Nanotubes in Viscous Polymer Flow: Part 2. *Langmuir*, **2007**. in progress
257. Lourie, O., Cox, D. M., Wagner, H. D., Buckling and collapse of embedded carbon nanotubes. *Physics Review Letters*, **1998**. 81(8):1638.
258. Zhao, Q., Frogley, M. D., Wanger, H.D., Using carbon nanotubes to sense matrix stresses around a single glass fiber. *Compsities Science and TEchnology*, **2001**. 61:2139.
259. Torquato, S., Statistical Description of Microstructures. *Annual Reviews Materials Research*, **2002**. 32:77.
260. Adams, B. L., P. R. Morris, T. T. Wang, K. S. Willden, and S. I. Wright, Description of Orientation Coherence in Polycrystalline Materials. *Acta Metallurgica*, **1987**. 35(12):2935.
261. Saheli, G., Garmestani, H., Gohkale, A. *Effective elastic properties of an Al-SiC composite using two-point statistical mechanics approach*. . in *AIP Conference Proceedings*. 2004.

262. Torquato, S. and G. J. Stell, Microstructure of Two-Phase Random Media. I. The N-Point Probability Functions. *Journal of Chemical Physics*, **1982**. 77(4):2071.
263. Odegard, G. M., Pipes, R.B., Hubert, P., Comparison of two models of SWCN polymer composites. *composites: Science and Technology*, **2003**. 64:1011.
264. Odegard, G. M., T. S. Gates, K. E. Wise, C. Park, and E. J. Siochi, Constitutive modeling of nanotube-reinforced polymer composites. *Composites Science and Technology*, **2003**. 63(11):1671.
265. Brown, W. F., Jr., Solid-Mixture Permittivities. *Journal of Chemical Physics*, **1955**. 23:1514.
266. Jefferson, G., Garmestani, H., Tannenbaum, R., Gokhale, A., Tadd, E., Two-point probability distribution function analysis of Co-polymer nano-composites. *International Journal of Plasticity* **2005**. 21:185.
267. Tewari, A., Gokhale, A. M., Spowart, J. E., Miracle, D. B., Qantitative characterization of spatial clustering in three-dimensional microstructures usign two-point correlation funtions. *Acta Materialia*, **2004**. 52:307.
268. Corson, P. B., *Journal of Applied Physics*, **1976**. 45
269. Corson, P. B., *Journal of Applied Physics*, **1976**. 45
270. Gokhale, A. M., A. Tewari, and H. Garmestani, Constraints on microstructural two-point correlation functions. *Scripta Materialia*, **2005**. 53:989.

VITA

ERIN LYNN CAMPONESCHI

ERIN LYNN CAMPONESCHI was born in Skokie, Illinois. She attended Batavia High School and graduated with her diploma in 1999. She received a B.S. in Materials Engineering from Iowa State University, Ames, Iowa in 2003. She then went on to Georgia Institute of Technology to receive her PhD in Materials Science and Engineering in 2007.